

UNIVERSIDAD COMPLUTENSE DE MADRID
FACULTAD DE CIENCIAS FÍSICAS



TESIS DOCTORAL

**Crecimiento y caracterización de óxidos funcionales de alta
calidad (Ni-Co-Fe) sobre Ru(0001)**

**Growth and characterization of high quality functional (Ni-
Co-Fe) oxides on Ru(0001)**

MEMORIA PARA OPTAR AL GRADO DE DOCTOR

PRESENTADA POR

Anna Malgorzata Mandziak

Directores

Juan de la Figuera Bayón
Lucía Aballe Aramburu

Madrid

UNIVERSIDAD COMPLUTENSE DE MADRID



FACULTAD DE CIENCIAS FÍSICAS
Departamento de Física de Materiales

Crecimiento y caracterización de óxidos funcionales de alta
calidad (Ni-Co-Fe) sobre Ru(0001)

Growth and characterization of high quality functional
(Ni-Co-Fe) oxides on Ru(0001)

Memoria presentada por
Anna Malgorzata Mandziak
para obtener el título de Doctor en Física

Directores:

Dr. Juan de la Figuera Bayón
Dr. Lucía Aballe Aramburu

Madrid, 2020



CSIC



Acknowledgements

In the first place, I would like to express my most sincere appreciation to my supervisors, Lucia Aballe and Juan de la Figuera, who have the substance of a genius: they convincingly guided and encouraged me to be professional and to do the right thing even when the road got tough. Without their persistent help, the goal of this project would not have been accomplished. I would also like to acknowledge the support and the valuable tips of Michael Foerster, who was always available for me during my stay at Alba synchrotron. I would like to say thank you to Lucas Perez, who helped me a lot with all the bureaucracy issues.

I am grateful to many people from Alba synchrotron, whose assistance was a milestone in the completion of this project. First, I would like to thank Jordi Prat for his countless help with all the technical problems I have encountered. I would also like to thank all the people from CIRCE beamline, especially Carlos, Virginia and Ignacio. On the other hand, I want to thank Stefano for his help in multiplet calculations, Antonello for his technical support, and Wojtek and Nitya for the time we joined together. I strongly appreciate the invaluable assistance that you all provided me during my stay there.

At this point, I would like to express my deepest gratitude to Dani, the person who was always with me, helping and supporting me every single day. Dani, your presence at Alba was really important for me and this kind of friendship will last forever. I would like to acknowledge the rest of my fantastic friends, with whom I was sharing my free time in Barcelona: Nerea, Albert, Isidro and Jan.

I wish to express my most sincere appreciation to the SURFMOSS group from Instituto de Química Física "Rocasolano" in Madrid. First, I would like to thank Guiomar for the amazing time we spent together, for the support during many beamtimes and for everything. With you the office work has never been boring. Next, I want to thank Miguel for such a great 6 months in Madrid. Thanks to you and Guiomar I really felt like at home. I am indebted also to all my workmates: Maria, Jose Emilio, Pepe, Eva, Guillermo, Victor and Alejandro.

I would like to say a special thank you to all the collaborators, without whom I would not had been able to obtain such a nice results: Adrian and Cecilia from Instituto de Cerámica y Vidrio, Pilar from Universitat Autònoma de Madrid, Sandra from Universidad Complutense de Madrid and many others who were always around.

I would like to express my most special gratitude to my family, especially my parents, who are always supporting me at each stage of my life, my brothers for whom I am always a little sister, and my aunt Agnieszka for her permanent support. I want to thank also Paweł, who helped and supported me in the most difficult part of my thesis.

Resumen

En óxidos complejos, la competencia entre los grados de libertad de carga, spin y orbital da lugar a fenómenos físicos de interés, tales como el ferromagnetismo, la ferroelectricidad o la multiferroelectricidad. En este campo, los avances conseguidos en su crecimiento permiten sintetizar de forma controlada heteroestructuras de alta calidad de los mismos, a veces controlando las dimensiones hasta al nivel de capas atómicas individuales. Por último, la obtención de propiedades electrónicas concretas en películas ultrafinas de óxidos abre la puerta a nuevas rutas para explorar funcionalidades nanoelectrónicas para diferentes aplicaciones.

En particular, los óxidos de metales de transición (TMO) constituyen un grupo de materiales de profundo interés que presentan una amplia variedad de estructuras, en parte como consecuencia de su capacidad de formar diferentes fases con proporciones de metal/oxígeno variables. Este tipo de materiales puede presentar cationes metálicos en múltiples estados de oxidación, afectando a sus propiedades químicas, ópticas, eléctricas y magnéticas. Buena parte de las propiedades de dichos óxidos proviene del carácter singular de los electrones “d” más externos de sus cationes. Sin embargo, para su aplicación en dispositivos, normalmente se requieren únicamente capas de unos pocos nanómetros. En este caso, los efectos de intercaras y de superficies, así como la presencia de defectos estructurales, desempeñan un papel crucial. De hecho, las películas ultrafinas de óxidos con estructura tipo espinela normalmente exhiben propiedades decepcionantes en comparación con sus análogos en estado volumen. Comprender de forma detallada sus propiedades magnéticas y de transporte en la escala nanométrica es fundamental para desarrollar y fabricar películas ultrafinas con las propiedades deseadas.

En esta tesis se emplea un método para la preparación de películas ultrafinas que permite obtener óxidos ternarios de metales de transición de muy alta calidad sobre sustratos metálicos. Los óxidos ternarios compuestos por níquel, hierro y cobalto objeto de estudio han sido crecidos sobre Ru(0001) por crecimiento epitaxial de haces moleculares a alta temperatura asistido por oxígeno molecular. Los procesos de nucleación y crecimiento llevados a cabo han sido observados en tiempo real mediante microscopía de electrones de baja energía (LEEM), lo cual permite optimizar los parámetros de crecimiento de forma ágil. La posterior caracterización de las muestras se realiza combinando varias técnicas. Para la caracterización estructural se emplea la combinación de LEEM y difracción de electrones de baja energía (LEED). Para el análisis químico se usa la microscopía de fotoemisión de electrones (PEEM) combinada con absorción de rayos-x (XAS), mediante el uso

de radiación sincrotrón. Y para la caracterización magnética se emplea el dicroísmo magnético circular y lineal de rayos X (XMCD-PEEM, XMLD-PEEM). Se ha descubierto que, dependiendo de las condiciones de crecimiento seleccionadas, se pueden obtener tanto ferritas con estructura tipo espínela como monóxidos divalentes con la estructura de la sal común.

La primera parte de esta tesis se centra en la preparación de películas finas de ferrita de níquel, que es ferrimagnética (NiFe_2O_4). Hemos observado que su crecimiento mediante la epitaxia de haces moleculares produce ferrita de níquel rica en hierro (i.e. no estequiométrica). Se han obtenido mapas de la imanación vectorial de la superficie combinando imágenes de dicroísmo circular de rayos-x adquiridas con diferentes ángulos azimutales. Se ha detectado que la imanación tiene componente fuera del plano de la película. También se determinaron los momentos magnéticos orbitales y de spin de cada catión.

A continuación, nos dedicamos al estudio de películas de óxido mixto níquel-cobalto (NCO). Para ello, diferentes películas de NCOs con espesores de hasta decenas de nanómetros han sido sintetizadas, observando como dicho crecimiento se produce de manera tridimensional, con nucleación de islas, las cuales presentan antiferromagnetismo a temperatura ambiente. La alta cristalinidad y morfología bien definida que presentan dan lugar a propiedades mejoradas respecto a películas crecidas empleando otros métodos. Se han observado dominios antiferromagnéticos de tamaño lateral que exceden en órdenes de magnitud a otros trabajos. También se ha mostrado como ajustar su temperatura de Néel variando la proporción relativa de níquel y cobalto.

La tercera parte de esta tesis se ha dedicado al estudio de las propiedades estructurales y magnéticas de películas de óxido de níquel. En este caso, el crecimiento se produce en forma de islas pequeñas de un ancho de unos pocos nanómetros. También se ha observado como la presencia de pequeñas cantidades de hierro modifica drásticamente el modo de crecimiento, conduciendo a la formación de islas de mayor tamaño. Estas presentan orden antiferromagnético a temperatura ambiente. Su dirección de spin ha sido determinada mediante magnetometría vectorial utilizando dicroísmo lineal de rayos-x y desarrollando el protocolo de análisis para sistemas monocristalinos con simetría cúbica.

Finalmente, hemos estudiado el cambio observado en las características de dominios ferrimagnéticos individuales en películas de magnetita bajo la aplicación de un campo magnético externo. Para ello, primero fue necesario diseñar un nuevo sistema de portamuestras, consistente en dos cuerpos portamuestras: uno empleado para calentamiento por bombardeo electrónico y otro para la aplicación in-situ de un pequeño campo magnético externo. Se ha observado como islas micrométricas de mayor espesor presentan la llamada configuración de dominios de Landau. Hemos estudiado la modificación de los dominios de Landau aplicando un campo magnético externo. Estos resultados experimentales han sido comparados con simulaciones micromagnéticas.

Abstract

The competition of charge, spin and orbital degrees of freedom in complex oxides leads to intriguing physical phenomena, including ferromagnetism, ferroelectricity or multiferroelectricity. The advances in the growth of oxides gives rise to the controlled synthesis of high-quality oxide heterostructures with monolayer-precision. Designing electronic properties in ultrathin oxide films and interfaces opens up routes to explore novel nanoelectronic functionalities for applications.

Particularly, transition metal oxides (TMO) are an interesting group of materials presenting a broad structural variety due to their ability to form phases of varying metal to oxygen ratios reflecting multiple stable oxidation states of the metal ions what influence their chemical, optical, electrical and magnetic properties. A broad range of different properties of these oxides are due to the unique nature of outermost d - electrons. However for the use in devices, often layers only few nm thick are required, in which interface and surface effects as well as defects, can play important roles. In fact, ultrathin spinel oxide films often exhibit disappointing properties compared to their bulk counterparts. Thus, optimized fabrication methods for ultrathin films and a detailed understanding of their magnetic and transport properties at such scale are needed.

In this thesis we demonstrate a route for preparing high quality ultrathin ternary transition metal oxide films on a metallic substrate. Mixed nickel, iron and cobalt oxides have been grown on Ru(0001) by high temperature oxygen-assisted molecular beam epitaxy. The nucleation and growth process are observed in real time by means of Low-Energy Electron Microscopy (LEEM), which enables to optimize the growth parameters. A comprehensive characterization is performed combining LEEM and LEED for structural characterization and PEEM (PhotoEmission Electron Microscopy) with synchrotron radiation for chemical and magnetic analysis via X-ray Absorption Spectroscopy, X-ray Magnetic Circular Dichroism and X-ray Magnetic Linear Dichroism (XAS-PEEM, XMCD-PEEM and XMLD-PEEM, respectively). We have found that depending on the chosen conditions, either spinel ferrites or divalent monoxides with rocksalt structure can be prepared.

The first part of this thesis is focused on the preparation of thin films of ferrimagnetic nickel ferrite (NiFe_2O_4). We have found that the growth by high-temperature oxygen-assisted MBE leads to formation of non-stoichiometric nickel ferrite (iron-rich). Surface magnetization maps have been obtained from XMCD-PEEM images acquired at three different azimuthal angles. An additional out-of-plane component

of the magnetization was detected. In order to complete the magnetic characterization of the sample, the spin and orbital moments have been determined from x-ray absorption spectra.

Next part of this thesis is focused on the study of mixed nickel-cobalt oxide (NCO) films. Mixed NCO films with thickness up to tens of nanometers have been synthesized. The growth proceeds in a three-dimensional way with the nucleation of small islands. The NCO islands present antiferromagnetism at room temperature. Their high crystalline and morphological quality result in optimized properties with respect to films grown by other methods, such as magnetic domains larger by several orders of magnitude. Moreover, we have found that the Néel temperature of our mixed oxides can be adjusted by varying the ratio between nickel and cobalt.

In the third part, the structural and magnetic properties of the nickel oxide films has been investigated. The growth results in a small, grainy islands up to few nm wide. It has been observed that small content of iron changes drastically the growth mode, leading to the formation of large, three-dimensional islands. We have found that the islands present antiferromagnetic ordering at room temperature. The spin direction was determined by vectorial magnetometry exploiting anisotropic XMLD for single crystalline systems of cubic symmetry.

Finally, we reported the switching characteristics of individual magnetic domains of magnetite (Fe_3O_4) films under applied magnetic field. For this purpose a new custom-made exchangeable sample holder system was designed. It is comprised of two sample holder bodies: one for electron bombardment heating and another one for the in-situ application of a small magnetic field. It has been observed that thick Fe_3O_4 micrometric islands present a so-called Landau-closure state. We were following the movement of the center of Landau state (a vortex) under a magnetic applied field were subsequently imaged by means of XMCD-PEEM. The experimental results have been compared with micromagnetic simulations.

Contents

Resumen	iii
Abstract	v
List of Figures	xi
List of Tables	xv
1 Introduction	1
1.1 References	4
I Theoretical and experimental background	7
2 Experimental Details	9
2.1 Molecular beam epitaxy (MBE)	9
2.1.1 Models for epitaxial growth	11
2.2 Characterization Techniques	13
2.2.1 Low Energy Electron Microscope	13
2.2.1.1 Experimental setup	13
2.2.1.2 Image contrast in LEEM	15
2.2.1.3 Working modes	16
2.2.2 Low Energy Electron Diffraction	17
2.2.2.1 Direct and reciprocal lattice	18
2.2.2.2 Notation for surface structures	19
2.2.3 Photoemission Electron Microscope	20
2.2.3.1 Resolution	21
2.2.4 CIRCE-PEEM end station at Alba synchrotron	22
2.3 Sample preparation	24
2.4 References	24
3 Magnetic spectroscopy using x-rays	27
3.1 Interaction of X-rays with Matter	27
3.2 X-ray Absorption Spectroscopy (XAS)	28
3.3 Dichroism	30
3.3.1 X-ray Natural Circular Dichroism	30
3.3.2 X-ray Magnetic Circular Dichroism	31
3.3.3 X-ray Natural Linear Dichroism (XNLD)	35

3.3.4	X-ray Magnetic Linear Dichroism (XMLD)	37
3.3.4.1	Isotropic and anisotropic XMLD	40
3.4	References	44
II	Experimental results	47
4	Nickel ferrite - NiFe₂O₄	49
4.1	Introduction	50
4.1.1	Crystal structure	50
4.1.2	Magnetism properties of nickel ferrite	51
4.2	Growth of nickel ferrite films by high temperature oxygen-assisted MBE	57
4.3	Chemical and magnetic properties	60
4.4	Conclusions	75
4.5	References	76
5	Mixed nickel-cobalt oxide - Ni_xCo_{1-x}O	83
5.1	Introduction	84
5.2	Magnetic structure	84
5.3	Growth mode and particle shape	89
5.4	Chemical and magnetic properties	92
5.5	Néel temperature dependence on composition	97
5.6	Conclusions	102
5.7	References	102
6	Fe-doped nickel oxide Fe-NiO	107
6.1	Introduction	107
6.2	Growth of nickel oxide thin films	109
6.2.1	Growth at different substrate temperature	109
6.2.2	Effect of Fe doping on the growth of NiO films on Ru(0001)	111
6.3	Chemical and magnetic properties	114
6.4	Magnetism in Fe-doped nickel oxide films	117
6.4.1	Ruling out the crystal field dichroism	117
6.4.2	Determination of the spin direction	118
6.5	Conclusions	126
6.6	References	126
7	Magnetite - Fe₃O₄ Manipulation of magnetic domains in thin magnetite films	131
7.1	Introduction	131
7.2	Growth and crystal structure	133
7.3	Evolution of magnetic domains in magnetite microstructures	134
7.4	Landau state of a thick magnetite microstructures	137
7.5	Vortex displacement in in-plane magnetic field	139
7.6	Conclusions	145
7.7	References	145

8	Conclusions	149
A	Appendix A	153
A.1	A custom-made sample holder for high temperature in-situ growth and magnetic field	153
B	List of acronyms and abbreviations	155
C		157

List of Figures

1.1	Transition metal oxides	2
2.1	Molecular Beam Epitaxy (MBE)	10
2.2	Models for epitaxial growth	11
2.3	Simple model of tension on the substrate	12
2.4	SPELEEM	13
2.5	Image contrast in LEEM	15
2.6	LEEM working modes	16
2.7	Universal curve	18
2.8	Real and reciprocal space	18
2.9	The resolution limit	21
2.10	SPELEEM at Alba synchrotron	23
3.1	Interactions of X-rays with matter	27
3.2	Schematic energy diagram of an atom	28
3.3	Examples of XAS spectra	29
3.4	Types of dichroism	30
3.5	Schematic diagram of XMCD	32
3.6	XMCD sum rules	34
3.7	Crystal field splitting	36
3.8	XNLD in strained NiO films	37
3.9	Illustration of XMLD process	38
3.10	Calculated XMLD spectra	40
4.1	Nickel ferrite crystal structure	51
4.2	Exchange interaction	52
4.3	Superexchange interaction	53
4.4	Double exchange interaction	53
4.5	Anisotropy constant in nickel ferrite	55
4.6	Magnetostriction in nickel ferrite	56
4.7	Oxygen evolution	57
4.8	Sequence of LEEM images during NFO growth	58
4.9	LEED patterns of nickel ferrite	59
4.10	Phase diagram	60
4.11	XAS and XMCD images of NFO islands	61
4.12	XAS and XMCD spectra at Fe-edge - wetting layer	62
4.13	XAS and XMCD spectra at Ni-edge - wetting layer	62
4.14	XAS and XMCD spectra at Fe-edge - island	63

4.15	XAS and XMCD spectra at Ni-edge - island	64
4.16	Computed XMCD spectra for Fe	65
4.17	Computed XMCD spectra for Ni	66
4.18	XMCD PEEM images at different azimuthal angles	67
4.19	Vector magnetization maps of a nickel-iron spinel island - Fe	68
4.20	Vector magnetization maps of a nickel-iron spinel island - Ni	68
4.21	Sum rules at the Fe $L_{2,3}$ absorption edge	71
4.22	Sum rules at the Ni $L_{2,3}$ absorption edge	72
4.23	X-ray absorption spectroscopy at O K-edge	73
4.24	XMCD images at Fe, Ni and O	74
4.25	Magnetic moment induced in oxygen	75
5.1	Cobalt oxide crystal structure	85
5.2	NiO-CoO phase diagram	86
5.3	Magnetic anisotropy energy	88
5.4	Selected frames from NCO growth in LEEM	89
5.5	LEEM IV curves	90
5.6	LEEM and LEED of NCO islands	91
5.7	Thickness estimation of NCO islands	91
5.8	XAS and XMCD images of NCO island	92
5.9	XAS and XMLD spectra at Co edge	93
5.10	XAS and XMLD spectra at Ni edge	93
5.11	XAS and XLD spectra at O edge	94
5.12	Polarization dependent XAS Co and Ni L_3 edge spectra	95
5.13	XMLD PEEM images for NCO/Ru(0001)	97
5.14	Temperature dependence of the asymmetry	98
5.15	Schematic representation of the magnetic interactions	98
5.16	Néel temperature of $Ni_{0.33}Co_{0.67}O$ islands with different thickness	99
5.17	Néel temperature of $Ni_{0.0.14}Co_{0.86}O$ islands with different thickness	100
5.18	Néel temperature of CoO islands with different thickness	100
5.19	Ising model	101
6.1	Nickel oxide crystal structure	108
6.2	Growth of NiO at different substrate temperature	110
6.3	AFM images of NiO	111
6.4	Growth of Fe-doped NiO	112
6.5	LEEM and LEED images of Fe-doped NiO	113
6.6	XAS and XLD images	114
6.7	XAS and XLD at O edge	115
6.8	XAS and XMLD at Ni edge	116
6.9	XAS and XMLD at Ni edge	116
6.10	Polarization dependent XAS Ni L_3 edge spectra	118
6.11	Experimental geometry	119
6.12	Fundamental spectra	120
6.13	Anisotropic XMLD in Fe-doped NiO - align islands	122
6.14	Anisotropic XMLD in Fe-doped NiO - rotated islands LH	124
6.15	Anisotropic XMLD in Fe-doped NiO - rotated islands LH	125

7.1	Magnetite crystal structure	132
7.2	Growth of magnetite	133
7.3	LEED pattern of Fe_3O_4 crystal	134
7.4	XAS and XMCD from Fe_3O_4 island	135
7.5	Evolution of magnetic domains in magnetite	136
7.6	Processes involved in magnetization reversal	136
7.7	Landau state in magnetite islands	137
7.8	The four basic vortex structures	138
7.9	Micromagnetic simulations	139
7.10	Magnetization precession in external magnetic field	140
7.11	The evolution of magnetic contrast under applied $H+$ field	141
7.12	The evolution of magnetic contrast under applied $H-$ field	142
7.13	In-plane magnetic field excitation of a magnetic vortex	142
7.14	Vortex displacement under in-plane applied magnetic field $H+$	144
7.15	Vortex displacement under in-plane applied magnetic field $H-$	144
A.1	Sample holder design	153
A.2	Magnetic field produced by the in-plane sample holder	154

List of Tables

4.1	Linear absorption coefficient	64
4.2	Spin and orbital magnetic moment of NFO	70
5.1	Transition metal monoxides	85
5.2	The Ni/Co flux ratio	94
6.1	Antiferromagnetic domains of NiO	108

1 Introduction

Oxides are a class of materials extensively used in areas as diverse as ceramics, catalysis or magnetic devices. Many oxides are proposed for the next generation of microelectronic devices, in the current search for multifunctional materials to beat the limitations of Moore's law[1–5]. We can distinguish several structural families of oxides, among which spinels have attracted much attention recently, due to the wide range of properties they can exhibit. The structure of spinel oxides consists of a face centred-cubic (fcc) lattice of 32 oxygen anions, where the cations occupy 1/4 of octahedral and and 1/8 tetrahedral sites. Their formula is XY_2O_4 , where X and Y are divalent and trivalent cations, respectively. In the so-called direct spinel structure, cations in tetrahedral site are divalent while cations in octahedral site are trivalent. Inverse spinels also exist with trivalent cations in tetrahedral sites and equally distributed divalent and trivalent cations in the octahedral sites. The structure is capable of incorporating various cations. The X and Y cations can even correspond to the same element with multiple oxidation state as for example Fe^{2+} and Fe^{3+} in magnetite[6].

The chemical flexibility of this oxide structure gives rise to a full range of different properties. Spinel can be half-metallic, insulators, transparent conductors ($NiCo_2O_4$ [7]), superconductors ($LiTi_2O_4$ [8]) or heavy-fermion compounds (LiV_2O_4 [9]). Additionally they exhibit a wide range of magnetic properties as ferri- (Fe_3O_4 , $NiFe_2O_4$ [10]) or antiferromagnetism (Co_3O_4 [11]), often with a high ordering temperature. Thus, the control over cations and their distribution allows to manipulate the physical properties of binary and ternary oxides of the $3d$ magnetic transition metals (Fe, Co and Ni). This is really important if the structures have reduced dimensionality, where often their bulk properties are disappointing.

This dissertation focus on the growth and characterization of different ternary transition metal oxide films on Ru(0001) with special emphasis on their magnetic properties. It is already known that often the properties of materials in thin film form are dominated by their defects. Thus to grow them in a defect-free form could open new avenues for basic and applied research. For this purpose we have been growing mixed iron, cobalt and nickel oxides on ruthenium by high temperature oxygen-assisted molecular beam epitaxy (HOMBE), leading to extremely high structural quality, reflected in their magnetic properties. Furthermore, by the possibility to adjust the ratio between the different cations we are able to tune their chemical and physical properties.

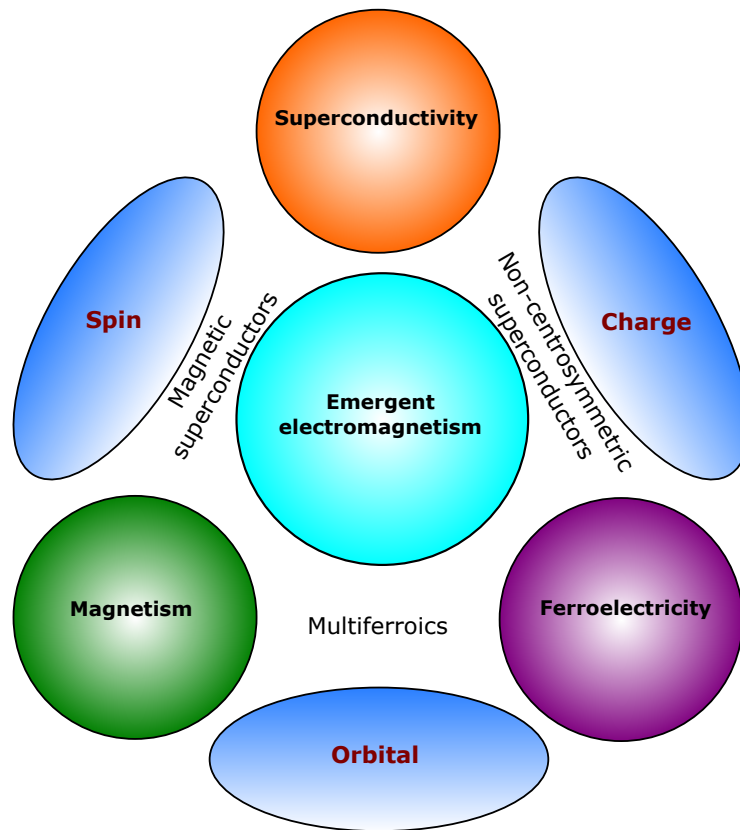


Figure 1.1: Schematic diagram showing the symmetries and degrees of freedom of correlated electrons that can be engineered at oxide systems.

Within this thesis several different goals will be addressed:

- To growth thin transition metal oxide films of bulk-like quality with a micrometric size, on a metallic substrate (Ru),
- To determine the structural, electronic and magnetic properties of these films, including the valence states of the cations and their distribution within the structure,
- To understand on the atomic level the mechanism responsible for magnetism in these in-situ grown oxide films,
- To understand how their properties can be manipulated by internal features (doping, defects, thickness) or external agents (e.g. external magnetic field).

Scope

The thesis is organized as follows:

The thesis begins with Chapter 2 in which the experimental methods are presented. We follow by discussing the main aspects of magnetic spectroscopies using x-rays (Chapter 3). Since the most important insight in the magnetic properties of surfaces and interfaces are provided by linear and circular dichroism we introduce all prerequisite concepts that we will apply in the following, in order to better understand the experimental results.

In the following chapters, we study the growth and structural properties of thin oxides films exploring the influence of the ratio between different cations on their properties, as well as their chemistry and magnetism by means of x-ray absorption spectromicroscopy.

Chapter 4 is dedicated for ferrimagnetic NiFe_2O_4 . The spinel has received a lot of attention recently due to its various applications in spintronics, catalysis and even in biomedicine. Thus, the fabrication of this oxide with well defined properties is an important challenge. At first we will give an overview about the growth process and its structural properties. Next, the magnetic properties of nickel ferrite will be studied with particular emphasis on the magnetic domain distribution within a given structure. Finally, the spin and orbital magnetic moments are determined by x-ray magnetic circular dichroism.

Chapter 5 is dedicated to grow mixed nickel-cobalt oxide films on Ru(0001). The chapter begins with a short introduction of the main properties of NiO and CoO and their mixed form, followed by studies found in literature about their mixed form. Next, the growth process for different cation ratios and the structural properties of the obtained thin films are presented. The corresponding magnetic properties are further investigated by means of x-ray magnetic linear dichroism. The last part of Chapter 5 is focused on the Néel temperature in mixed NCO films, where we show how the Néel temperature can be adjusted by changing the Ni:Co ratio.

Chapter 6 focuses on the growth and characterization of thin nickel oxide (NiO) films on Ru(0001). Since, the growth of pure NiO is a very subtle issue, in this chapter we are providing an alternative approach (doping by Fe) which allows to obtain high-quality nickel oxide microstructures. After the comparative structural analysis, we will turn our attention to the study of its magnetic domain configurations. In order to resolve this problem we develop a vectorial magnetometry method based on a theoretical model.

Chapter 7 closes the experimental part of this thesis. This chapter begins with a brief introduction of Fe_3O_4 and its possible applications in a future spintronic devices.

Further, we present the growth process and the structural properties of magnetite thin films prepared by means of a new custom-made exchangeable sample holder. Finally, we focus on the magnetic domains in Fe_3O_4 and their behaviour under applied external magnetic field.

Finally, we conclude our analysis and summarize the main results in Chapter 8.

1.1 References

- [1] H. Y. Hwang et al. Emergent phenomena at oxide interfaces. *Nat. Mater.*, 2012. doi:[10.1038/nmat3223](https://doi.org/10.1038/nmat3223).
- [2] U. Lüders et al. NiFe_2O_4 : A versatile spinel material brings new opportunities for spintronics. *Advanced Materials*, 2006. doi:[10.1002/adma.200500972](https://doi.org/10.1002/adma.200500972).
- [3] J.-B. Moussy. From epitaxial growth of ferrite thin films to spin-polarized tunnelling. *J. Phys. D : Appl. Phys.*, 2013. doi:[10.1088/0022-3727/46/14/143001](https://doi.org/10.1088/0022-3727/46/14/143001).
- [4] M. Opel. Spintronic oxides grown by laser-MBE. *J. Phys. D : Appl. Phys.*, 2011. doi:[10.1088/0022-3727/45/3/033001](https://doi.org/10.1088/0022-3727/45/3/033001).
- [5] T. Jungwirth et al. Antiferromagnetic spintronics. *Nat. Nano.*, 2016. doi:[10.1038/nnano.2016.18](https://doi.org/10.1038/nnano.2016.18).
- [6] X. Zhang et al. Prediction of A_2BX_4 metal-chalcogenide compounds via first-principles thermodynamics. *Phys. Rev. B*, 2012. doi:[10.1103/PhysRevB.86.014109](https://doi.org/10.1103/PhysRevB.86.014109).
- [7] P. Silwal et al. Thickness dependent structural, magnetic, and electronic properties of the epitaxial films of transparent conducting oxide NiCo_2O_4 . *J. Appl. Phys.*, 2013. doi:[10.1063/1.4820930](https://doi.org/10.1063/1.4820930).
- [8] K. Yoshimatsu et al. Reversible superconductor-insulator transition in LiTi_2O_4 induced by li-ion electrochemical reaction. *Sci. Rep.*, 2015. doi:[10.1038/srep16325](https://doi.org/10.1038/srep16325).
- [9] C. M. Varma. Heavy fermions in the transition-metal compound LiV_2O_4 . *Phys. Rev. B*, 1999. doi:[10.1103/PhysRevB.60.R6973](https://doi.org/10.1103/PhysRevB.60.R6973).
- [10] M. Hoppe et al. Enhanced ferrimagnetism in auxetic NiFe_2O_4 in the crossover to the ultrathin-film limit. *Phys. Rev. B*, 2015. doi:[10.1103/PhysRevB.91.054418](https://doi.org/10.1103/PhysRevB.91.054418).

- [11] S. Thota and S. Singh. Nature of magnetic ordering in cobalt-based spinels. In M. S. Seehra, editor, *Magnetic Spinels*, chapter 4. IntechOpen, 2017. doi: [10.5772/65913](https://doi.org/10.5772/65913).

Part I

Theoretical and experimental background

2 Experimental Details

In the following chapter the experimental techniques used in this thesis will be presented, with particular emphasis on the epitaxial process employed to grow thin films of transition metal oxides. The second part of this chapter will give a brief overview about the Low-Energy Electron Microscopy and its possible working modes. Finally, a brief description of the preparation method of the samples studied in this work will be provided.

2.1 Molecular beam epitaxy (MBE)

Epitaxy, is the growth of a (solid) film on a crystalline substrate in which the atoms mimic the arrangement of the film atoms in the substrate. Accordingly, the epitaxially grown layer should possess the same orientation as the substrate. Thus, the substrate itself plays an important role in the growth process, because it has a direct influence on the atomic arrangement of the growing film.

One of the most common methods for preparation of thin films is Molecular Beam Epitaxy (MBE). In MBE a flux of atoms is directed towards the substrate. The atoms condense on the substrate, and depending on the substrate temperature, they diffuse around the surface and form islands. MBE is the most versatile technique for preparing clean and well-defined surfaces and interfaces. It allows for a controlled growth of films with sharp doping profiles and different chemical composition changing over a depth (e.g. multilayer structures).

Experimentally the atom beam during the MBE process is generated with sources heated by electron bombardment. Evaporation is possible either from a rod or a crucible, where the pellets are introduced. A (tungsten) filament is placed in the immediate vicinity of the electrically conducting rods or crucible (which are held at high positive potential) and provide electrons which are accelerated towards the evaporant rod/crucible producing a high heating-power densities. The evaporation crucibles are highly efficient water-cooled to limit outgassing (Figure 2.1)[1].

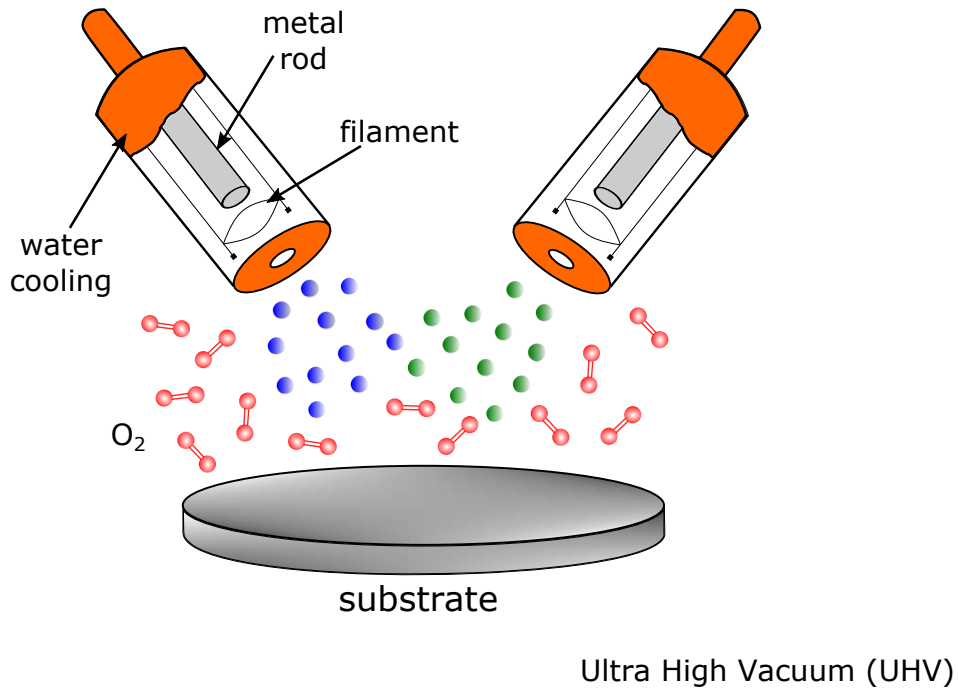


Figure 2.1: Schematic draw of molecular beam epitaxy system

The oxide films which are the subject of this thesis, are grown by oxygen-assisted molecular beam epitaxy: (molecular or atomic) oxygen is supplied during the MBE process. This technique was employed to grow mixed transition metal oxide films by co-depositing a combination of Fe, Co and Ni in an oxygen atmosphere on Ru(0001) substrate at elevated temperature.

It has to be pointed out that this method in comparison with pulse laser deposition (PLD) or sputtering, is quite slow and requires ultra high vacuum (UHV) conditions[2]. In our work, typical deposition rates are of the order of 1 monolayer (ML) per several minutes. By growing on a single crystal, at high temperature and slow rate results in low nucleation density, and thus allows for preparing well-defined surfaces and interfaces. That makes the MBE process much more demanding, but it allows for a better control of the growth process cleanliness. This is important for the preparation of thin films with a high crystalline quality.

During this thesis, we have been using both commercial and homemade evaporators of Fe, Co and Ni. A schematic draw of the evaporation is shown in Figure 2.1. The evaporation rate of each doser was calibrated carefully by evaporating 1 ML of Fe, Co on Ru(0001) and Ni on W(110) (Ni metal was not evaporated directly on Ru because it is known that it alloys severely) respectively. The nominal evaporators power used during the growth was typically 30 W ($HV=2$ kV, $I_{filament}=5$ A, $I_{emission}=15$ mA). While growing oxides, the oxygen base pressure was 10^{-6} mbar.

2.1.1 Models for epitaxial growth

The growth process of thin epitaxial films strongly depends on the interaction between adatoms and the surface. While it is possible to grow epitaxial layers from a liquid solution, most epitaxial growth occurs via a physical or chemical vapor techniques such as molecular beam epitaxy. Once a particle has condensed from the vapor phase it may re-evaporate or diffuse along the surface. The diffusion process can lead to adsorption at special sites on the surface like step edges or other defects. Nucleation of more than one adsorbed particle might also occur. In order to understand the processes occurring on the surface the kinetic theory is required[3]. Instead of following more theoretical approach we will present the process of film growth more phenomenologically.

Three main growth modes on the substrate can be distinguished[4–6]. These modes are illustrated schematically in Figure 2.2.

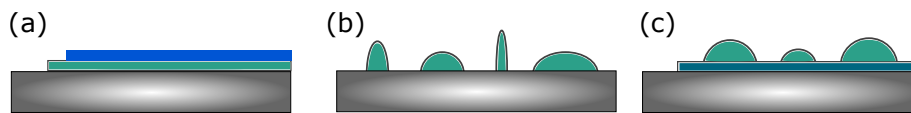


Figure 2.2: Schematic representation of three major film growth processes: (a) Frank van der Merwe layer-by-layer growth; (b) Volmer-Weber island growth; (c) Stranski-Krastanov layer-plus-island growth;

- Layer-by-layer (Frank-van der Merwe) - the atoms preferentially attach to the surface site rather than to each other. As a result they condense and form atomically smooth, fully closed layers. This mode is often observed in systems such as metal on metal or in semiconductor on semiconductor.
- Islands (Volmer-Weber) - in the opposite case to the previous one. In it the deposited atoms are more strongly bound to each other than to the substrate. This gives rise to the island growth mode. This mode is characteristic for many systems of metals growing on insulating substrates.
- Layer plus island (Stranski-Krastanov) - is an intermediate case. Material deposited onto the substrate forms an atomic monolayer (or a thin film). However the growth of subsequent layers is unfavourable. Thus islands formation occurs. Many factors can account for this mode of growth, for example a lattice mismatch between substrate and deposited film may not be able to be continued into the bulk of the epitaxial crystal.

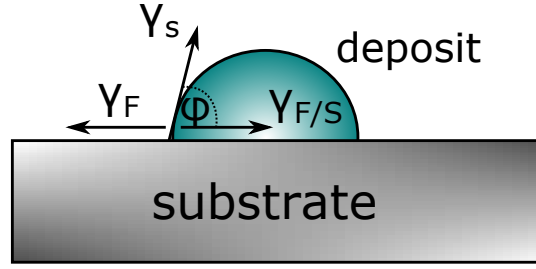


Figure 2.3: Schematic drawing of an island deposited on the surface. γ_S , γ_F and $\gamma_{S/F}$ are the surface tension between substrate and vacuum, between film and vacuum and between substrate and film, respectively.

The occurrence of the various growth modes can be explained in terms of surface and interface tension γ the characteristic free energy per unit area needed to create an extra surface or interface (Figure 2.3). In the equilibrium form, when the surface and deposited film are in contact:

$$\gamma_S = \gamma_{S/F} + \gamma_F \cos\theta \quad (2.1)$$

where γ_S is the surface tension at the substrate/vacuum interface, γ_F at the film/vacuum, $\gamma_{S/F}$ the one at the substrate/film interface. In the two opposite growth modes (a) layer-by-layer and (b) island Equation 2.1 can be rewritten:

- layer-by-layer growth (FM)

$$\gamma_S \geq \gamma_{S/F} + \gamma_F \quad \theta = 0 \quad (2.2)$$

- islands growth (VW)

$$\gamma_S < \gamma_{S/F} + \gamma_F \quad \theta > 0 \quad (2.3)$$

In many realistic cases is hard to predict the exact growth mode. In the cases study in the following, growth is performed out-of-equilibrium, by mixing two or three components at the same time. Hence, it limits the application of the model described above.

2.2 Characterization Techniques

2.2.1 Low Energy Electron Microscope

Low Energy Electron Microscopy (LEEM) is a technique invented by Ernst Bauer at the beginning of 1970s[7]. This powerful technique combines real-time imaging with high temporal and spatial resolution with complementary diffraction mode imaging, allowing to study and monitor in real time surfaces, thin films, interfaces and physical processes on a surface (growth, chemical reactions, phase transitions). A schematic draw of the LEEM microscope installed at Alba synchrotron is presented in Figure 2.4.

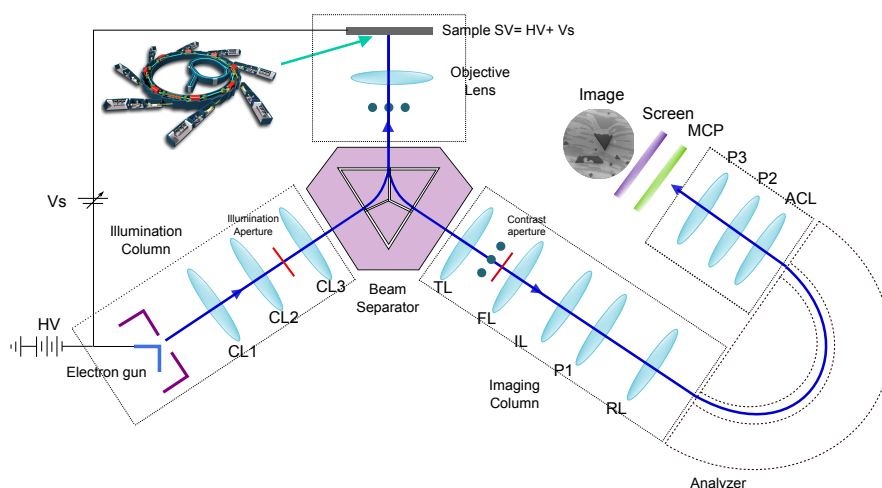


Figure 2.4: Spectroscopic Photoemission and Low Energy Electron Microscope (SPELEEM) - general layout.

2.2.1.1 Experimental setup

From a technical point of view a low energy electron microscope has a similar design to a Transmission Electron Microscope (TEM). It consists of set of electromagnetic lenses which manipulate and focus an electron beam illuminating the sample. However, unlike TEM, LEEM works typically with slow electrons at an energy of a few eV. A LEEM comprises of four main parts: an illumination column, a beam separator, a main chamber with an objective lens and an imaging column. It should be pointed out also that LEEM is so called cathode lens microscope i.e. the sample located in the main chamber is a part of the objective.[8–10].

1. The illumination column - equipped with an electron gun (a thermionic-emission based LaB_6 single crystal and Wehnelt cylinder for controlling the

electron emission). Electron beam is further collimated by a set of three condenser lenses with magnetic deflection coils. The final beam spot size is improved by a pair of stigmators. Additionally an illumination aperture placed in the illumination column allows to reduce the beam spot on the sample surface and is particularly useful for selected area electron diffraction. The electrons traverse the focusing field within the illumination column at a high electron energy of 20 keV to avoid the influence of external fields (electric and magnetic).

2. The beam separator - is a part of both illumination and imaging column. It separates the incoming electrons from the outgoing ones backscattered from the sample. The deflection is achieved by applying a magnetic field to bend an electron beam through a desired angle in moving from one arm of the microscope to another. Typically a LEEM uses 120° prism deflectors but also 90° systems are commercially available (Elmitec/SPECS).
3. The main chamber with an objective lens - the heart of the whole microscope. The objective lens is responsible for decelerating the incoming electrons from the energy of 20 keV to the energy of few eV before reaching the sample. After interaction with a surface, the backscattered electrons are re-accelerated again by the same objective lens. In that part of the microscope a lot of images aberrations are produced, affecting the final resolution of the microscope (2.2.3.1). A surface diffraction pattern is formed at a back-focal plane of the objective lens.
4. The imaging column - equipped with a set of lenses which form and transfer the image of backscattered electrons onto a screen. The electron beam coming from the sample surface passes through the beam splitter, behind which the first lens of the imaging column is located - the transfer lens (TL) which relays the first intermediate image, formed by the objective lens, towards the intermediate (IL) and field lens (FL), that are coupled together. A contrast aperture is placed at the back focal plane of the objective lens, where parallel rays coming from the sample plane are focused and the diffraction pattern is formed (LEED). FL and IL allow to switch between imaging the real space (image plane - LEEM) and reciprocal space (back-focal plane - LEED). Finally, a set of two projective lenses (PL) magnify and project the image on a multiple channel plate (MCP) detector. MCP acts as an amplifier and relay a highly magnified image on a fluorescent screen for a video rate image acquisition by CCD camera.

The microscope can additionally work as a Photoemission Electron Microscope (PEEM) (2.2.3), once a light source (mercury lamp or synchrotron radiation) is available. The instrument can also be equipped with an electron energy analyzer installed in the imaging column. Thus, the combination of light source with an energy analyzer offer a wide range of other surface-sensitive characterization techniques like X-ray absorption spectroscopy (XAS), X-ray Pho-

toemission Spectroscopy (XPS), Angle-resolved Photoemission Spectroscopy (ARPES) or X-ray Photoelectron Diffraction (XPD)[11].

2.2.1.2 Image contrast in LEEM

The interaction of low-energy electrons with a substrate can give rise to a different contrast mechanisms. For that reason LEEM is a powerful technique that allows for a variety of structure characterization methods[12].

One of the most common image contrast observed in LEEM is the so called **diffraction contrast** (Figure 2.5a). It arises due to the local variation of the structure factor (it express how materials scatters incident radiation). Diffraction contrast can be observed for example, in a bright-field imaging at normal incidence (the specular beam is selected for imaging) when the geometric structures differ between different phases. A well-known example is the Si(111) surface in which there is a coexistence of two different surface reconstructions: (1×1) and (7×7) . Those two phases will appear in the LEEM image as a black and white areas respectively[13].

Diffraction contrast is also important in dark-field imaging. Dark-field imaging is especially useful for identifying the spatial distribution of co-existing phases or domains on the surface. The image is form by selecting a higher order diffraction spot (e.g $(1,0)$). The diffraction order is selected by placing the contrast aperture on the desired beam. The resulting image gives a direct image of the corresponding surface structure.

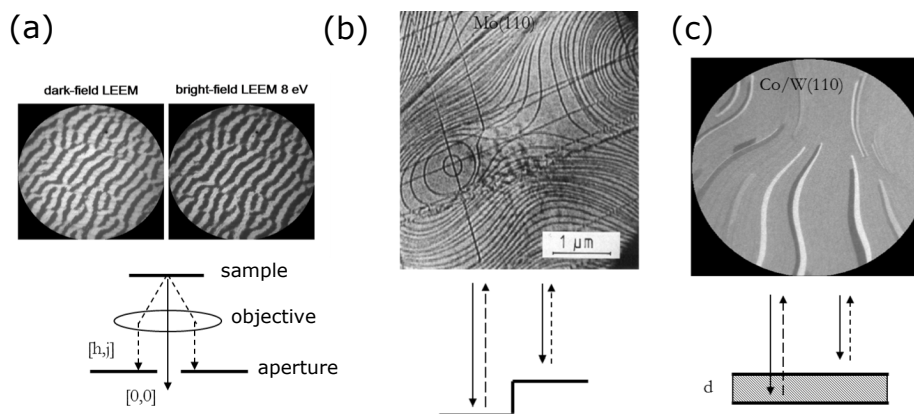


Figure 2.5: Main contrast mechanisms in LEEM (a) diffraction contrast, (b) step contrast and (c) quantum size effect contrast

One important class of LEEM contrast mechanisms are those coming from the phase difference of the imaging electron waves. Two examples of phase contrast are atomic

step contrast and quantum size contrast. Both of them provide atomic resolution perpendicular to the surface. **Step contrast** (Figure 2.5b) arises from the interference of the electron wave that is reflected from terraces on opposite sides of the step. As a consequence a phase shift appears from the path length difference of the two waves. This can be converted into an amplitude difference by slightly defocusing the image which makes the surface steps visible. Since the wavelength of electrons can be chosen of the order of the step height, this contrast allows to determine the step sense (the up and down-sides of a step) and its height[14].

Quantum size contrast is a vivid manifestation of the quantum size effect (QSE) in electron reflectivity. It is an interface phenomena that occur between the electron waves reflected from the surface of a thin films and its interface with the substrate. It produces intensity maxima and minima depending on thickness of the thin film and the electron energy[15]. This mechanism allows quantitative measurement of film thickness on surfaces. A LEEM image that shows quantum size contrast is shown in Figure 2.5c.

2.2.1.3 Working modes

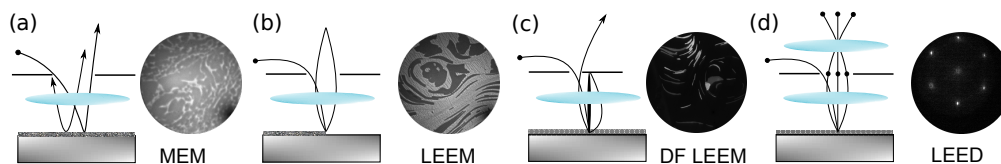


Figure 2.6: Different working modes of a LEEM instrument: (a) Mirror Electron Microscopy of Gr on Ru(0001), (b) Bright Field Low Energy Electron Microscopy of Gr/Ru(0001), (c) Dark Field Low Energy Electron Microscopy and (d) μ -Low Energy Electron Diffraction of Fe_3O_4 islands on Ru(0001).

The complexity of the LEEM setup gives the possibility for a different of imaging modes (MEM, LEEM, PEEM) and complementary methods (selected area LEED) which will be briefly discussed in the following[16].

1. Mirror Electron Microscopy (MEM) (Figure 2.6a) - the specimen is at a more negative potential than the electron source. Thus, the incident electrons are reflected in front of the surface. Imaging at or near the MEM transition allows to map the local work function but also variations in the surface topography. The main advantage of this method is that the sample does not have to be crystalline, unlike for LEEM or LEED.
2. Diffraction imaging (bright and dark field LEEM) (Figure 2.6b) - images the surface with elastically backscattered low energy electrons. The contrast is determined by morphology and crystal structure of the surface. Due to the

short inelastic mean free path (IMFP) at low electron energies, it is a surface sensitive technique that probes only few atomic layers near the surface.

3. μ - Low Energy Electron Diffraction (μ LEED) Figure 2.6d - is a natural extension of low energy electron microscope. By placing a small aperture on the path of the electron beam in the illumination column the illuminated sample area can be limited to a micrometer-sized region, giving rise to micro-LEED operation. In comparison with a conventional system it allows one to select small areas on the surface for LEED (e.g. islands, domains).

2.2.2 Low Energy Electron Diffraction

In order to determine the film crystallography the common electron-based diffraction techniques such as Low Energy Electron Diffraction (LEED)[17] or Reflection of High Energy Electron Diffraction (RHEED)[18] are used.

Low Energy Electron Diffraction (LEED) is one of the most important techniques available for surface structural analysis[19]. A conventional LEED diffractometer comprises an electron gun that generates a mono-energetic electron beam and a retarding field analyser (RFA) which is a set of three or four hemispherical grids with a phosphorus screen at the end. Inelastically scattered electrons are suppressed by the set of grids. Elastically scattered electrons impinge on a phosphorus screen after being accelerated[17; 20]. The energy of the electrons in LEED experiments is typically in the range 10 – 500 eV and the associated e^- wavelength given by the de Broglie formula:

$$\lambda = \frac{h}{\sqrt{2mE}} \quad (2.4)$$

is of the order of Åi.e., is comparable with the inter-atomic distances in solids, required to achieve the diffraction effects from atoms[21]. The inelastic mean free path of electrons (IMFP) shows how far the electrons travel in the solid before losing an energy. For this electrons with energy 10 – 500 eV energy, is of order of a few nanometers (the energy dependent IMFP for different materials is represented by universal curve[22] shown in Figure 2.7). Thus, only the near surface structure can be probed by LEED. This makes the technique highly surface sensitive.

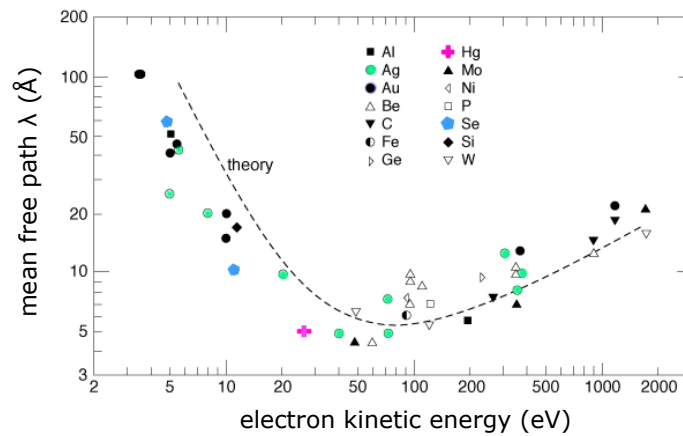


Figure 2.7: Electrons mean-free path universal curve in solids as a function of their energy, reprinted from [22].

Apart from commercial LEED systems described above, low energy electron diffraction can be measured in a Low Energy Electron Microscope (LEEM), as presented in detail in the previous section.

2.2.2.1 Direct and reciprocal lattice

To better understand the diffraction process, the concept of real and reciprocal space will be discussed.

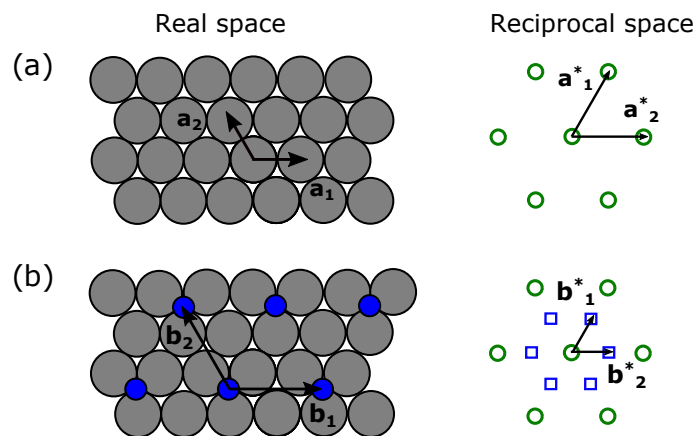


Figure 2.8: (a) Schematic representation of the atomic arrangement of a hexagonal surface. The real-space (and corresponding reciprocal-space) unit cell is shown on the left (right). (b) Schematic representation of the (2×2) superstructure on a hexagonal surface. The real (and reciprocal-space) unit cell is shown on the left (right).

The surface of a crystal can be considered as a two-dimensional lattice described by unit vectors a_1 and a_2 . The space in which the lattice is defined is called the direct or real space, as real objects like atoms or molecules lie on it. As an example, a hexagonal surface lattice together with its unit cell is shown in Figure 2.8a.

The diffraction pattern observed in LEED are directly related to a reciprocal lattice. The reciprocal space is based on the concept that real space planes are represented by reciprocal space points and vice versa. Thus the reciprocal space of a two-dimensional lattice can be described by two vectors a_1^* and a_2^* . The mathematical transformation between the real a_1 and a_2 and the reciprocal space lattice a_1^* and a_2^* is as follow:

$$a_1^* = 2\pi \frac{a_2 \times a_3}{a_1 \cdot (a_2 \times a_3)} \quad a_2^* = 2\pi \frac{a_3 \times a_1}{a_2 \cdot (a_3 \times a_1)} \quad (2.5)$$

The third vector a_3^* is a unit vector, perpendicular to the plane (a_1^* , a_2^*). Each vector defined in the equation 2.5 is orthogonal to two axis vectors of the crystal lattice. Thus they fulfil the condition:

$$a_i^* \cdot a_j^* = 2\pi \delta_{i,j} \quad (2.6)$$

where $\delta_{i,j} = 1$ if $i = j$ and $\delta_{i,j} = 0$ if $i \neq j$.

Any reciprocal lattice point can be mapped by the set of vectors, given by $G = h \cdot a_1^* + k \cdot a_2^*$ where h, k are integers. A vector G of this form is a reciprocal lattice vector and the set of G is associated with a crystal structure. If we now consider an incident electron wave $k_0 = 2\pi/\lambda_0$ and diffracted wave $k = 2\pi/\lambda$, the diffraction condition can be defined by the following:

$$k_0 - k = \Delta k = G \quad (2.7)$$

Generally speaking, an incoming electron beam can be scattered in many directions, but only those electrons which follow equation 2.7 will contribute to constructive interference. Thus, the diffraction image is just an image of the reciprocal space[23].

2.2.2.2 Notation for surface structures

Adsorbed or surface atoms frequently exhibit long range ordering. However, they do not always follow the arrangement of the substrate. This is called a surface reconstruction. In general, the change of surface lattice between the bulk truncated

surface and the reconstructed surface can be analysed studying the diffraction pattern. The surface reconstruction unit cell can be specified by a matrix¹ or using Wood notation[24; 25].

The Wood's notation is particularly suited to commensurate structures and relates the overlayer net to the substrate mesh. If one takes the structure shown in Figure 2.8b, which present a simple overlayer on a hexagonal substrate, it is seen that the adsorb overlayer unit cell is defined by the two vectors b_1 and b_2 parallel to the substrate vectors a_1 and a_2 . In addition:

$$|b_1| = 2|a_1| \quad |b_2| = 2|a_2| \quad (2.8)$$

what means that the b_1 and b_2 are twice as long as the surface unit vectors. Thus, the overlayer unit cell is referred to as (2×2) (two by two) overlayer. Apart from vectors length, the Wood's notation takes into account additionally the angle between substrate and overlayer net. Hence, the Wood's notation can be described fully as:

$$M(hkl) - \left(\frac{|b_1|}{|a_1|} \times \frac{|b_2|}{|a_2|} \right) - R\alpha^\circ - A \quad (2.9)$$

where M is chemical symbol of the substrate, (hkl) Miller index of the surface plane, $|a_1|$ and $|a_2|$ length of substrate net vectors, $|b_1|$ and $|b_2|$ length of surface overlayer net vectors, α° angle between substrate and overlayer meshes (omitted if $\alpha = 0^\circ$ and A chemical symbol of surface species (for clean surface $A = M$). For example, when oxygen adsorbs on Ru(0001) (up to 0.25 ML) creates (2x2) superstructure. In the Wood's notation, the oxygen phase would be described as Ru(0001)(2x2) - O[26].

2.2.3 Photoemission Electron Microscope

In Photoemission Electron Microscopy (PEEM) instead of using an electron beam, the sample is illuminated by UV (ultra-violet) or X-ray photons (XPEEM). Incoming photons stimulate the emission of photoelectrons. The general XPEEM setup is similar to LEEM and is based on a cathode lens system, which accelerate photoelectrons to an energy of 20 keV and transfer them into the imaging column. Conventional photon sources available in most laboratories provide some limitations, as most of the information on the surface chemistry is accessible only by using higher photon energies (from few eV up to 1 keV). Using a tunable X-ray source greatly extends the application field of the PEEM microscope. XPEEM has become a widely

¹Matrix notation is more general and can be used to described overlayer structures that are both commensurate and incommensurate.

used technique for the element-specific, direct imaging of the surfaces and interfaces. The chemical, magnetic and electronic structure contrast can be achieved through the implementation of well-known photoelectron spectroscopies: X-ray absorption spectroscopy (XAS), X-ray photoelectron spectroscopy (XPS), and angle-resolved photoemission spectroscopy (ARPES). The first method combined with the manipulation of x-ray polarization has been extensively employed to image magnetic domains on a magnetic surface via X-ray magnetic circular dichroism (XMCD) and X-ray magnetic linear dichroism (XMLD). In the following chapter 3.3.2 we will introduce the main concepts of XAS, XMCD and XMLD techniques[27–29].

Furthermore, the combination of energy-filtered PEEM with LEEM and micro-spot LEED offers a multimethod approach for structural and chemical surface investigations.

2.2.3.1 Resolution

Spatial resolution

One of the most important factor of a microscope is the resolution limit. In the LEEM/PEEM microscope the spatial resolution is only determined by the electron optics. The main limits for the final resolution arise from the aberrations (chromatic and spherical) of the objective lens. Those aberrations are caused by the acc/decelerating field and the resulting energy spread (Figure 2.9a). The chromatic aberration is proportional to the starting electron angle α_0 , while the spherical one to α_0^3 . Additionally, a resolution limitation is caused by diffraction at contrast aperture. The optimum resolution can be determined by minimizing the sum of the squares of three aberrations: $\delta^2 = \delta_c^2 + \delta_s^2 + \delta_D^2$ [10]. Figure 2.9b shows the influence of the aberrations on the final resolution limit:

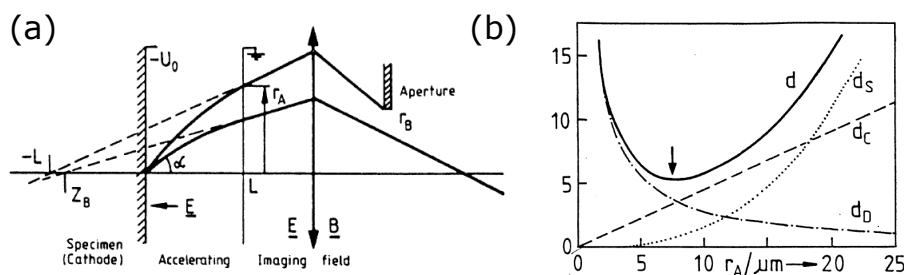


Figure 2.9: (a) Simplified schematic draw of the optics of the cathode lens. (b) The resolution-determining factors. Solid curve represents the final resolution as a function of the angle-limiting aperture r_A . Reprinted from [10].

Spherical aberrations are typically minimized using a contrast aperture placed in the diffraction plane of the illumination column. While the chromatic aberration in LEEM is reduced by decreasing the energy spread of the electron source.

The lateral resolution for typical operation conditions in LEEM ($HV = 20\text{kV}$) is lower than 10 nm, while in XPEEM is around 20 nm. However, there are a lot of factors limiting the final resolution of the microscope, thus the real value is slightly reduced and is around 30 nm. The resolution of the microscope is improved if the aberrations are reduced. This is performed by electron mirrors in systems called aberration corrected LEEM/PEEM that offer a spatial resolution of 4 nm or better[30].

Energy resolution

The energy resolution is important in spectroscopy for the contrast between two or more species with core levels of similar energy. Its value is combination of both the resolution of the hemispherical electron energy analyzer (below 0.15 eV) and that of the illuminating x-ray source. The beamline resolving power $E/\Delta E$ is up to 8000 and its tunable throughout the photon energy range. Therefore, in most of the practical cases, the energy analyzer is the limiting factor for the energy resolution[27].

2.2.4 CIRCE-PEEM end station at Alba synchrotron

The Alba XPEEM end-station is based on Spectroscopic PhotoEmission and Low Energy Electron Microscope (SPELEEM), commercially available from Elmitec GmbH. The APPLE II helical undulator with variable polarization is used as an x-ray source and allows a full polarization control. A plane-grating monochromator provides soft x-ray photons in the 100-2000 eV energy range that are shared between two independent branches: PEEM and NAPP (Near Ambient Pressure Photoemission). After the monochromator chamber, there are two toroidal mirrors which focus the beam onto exit slit. Further, a couple of deflecting mirrors directs the beam to one branch or to the other. The microscope chamber is tilted 16° with respect to the incoming photons, thus the geometry imposes a near-grazing incidence. Beam spot size at PEEM position (vertical \times horizontal) is $3.2 \times 36 \mu\text{m}^2$ and it can be varied in the vertical direction up to 50 μm . The fine beam steering is performed with the KB focussing mirrors installed upstream of the microscope.

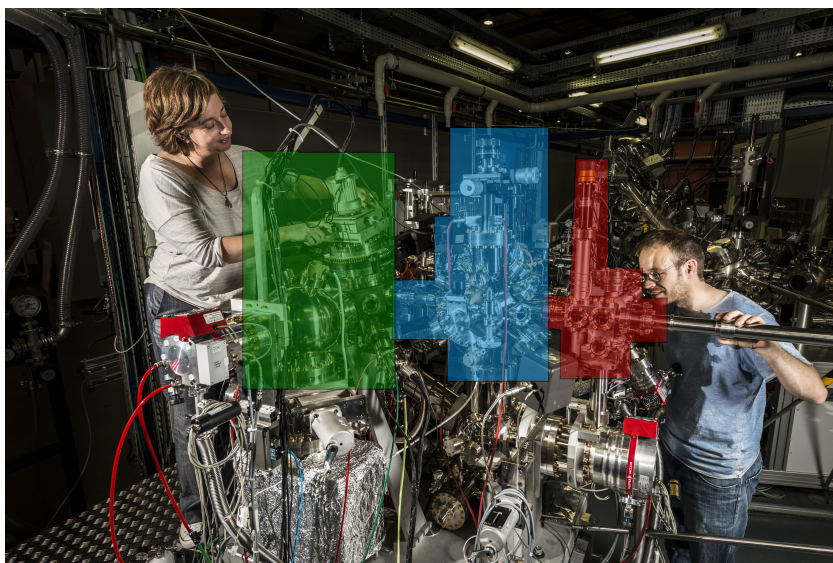


Figure 2.10: CIRCE-PEEM end station installed at Alba synchrotron.

The full setup of the CIRCE SPELEEM is shown in Figure 2.10. It consists of a microscope chamber (marked in green in Figure 2.10), a preparation chamber (blue) and an entrance chamber connected to fast load-lock entry (red). A preparation chamber is equipped with different tools for surface preparation (i.e. sputter gun and heating stage for oxygen treatment). The entrance column comprises of parking stage and a wobble stick providing a fast and convenient way to transfer the sample between two sample holder bodies without breaking the ultra-high vacuum (using the new sample holder described in the Appendix A). The surface preparation can be performed also in the main chamber where the sample can be heated up to 2000 K for a few second. The temperature is measured by a W/Re thermocouple attached to the sample holder. The microscope chamber includes several evaporators (for MBE deposition) installed on linear manipulators. A six-fold manipulator attached to the MCH allows for rotating the sample with respect to the photon beam (around the normal to the sample)[31].

The system offers a full range of different characterization techniques. LEEM and LEED requiring an electron source, and also synchrotron-based spectromicroscopies such as XPEEM, XAS or XPS.

2.3 Sample preparation

Transition metal oxide films are deposited onto a (0001)-oriented ruthenium single crystal (commercially available from Mateck). The Ru substrate is first sputtered with Ar^+ ions in order to remove previously grown films. Then it is annealed to 1170 K in 10^{-6} mbar molecular oxygen and flashed to 1800 K in vacuum, in order to remove carbon diffusing from the bulk and the surface oxide, respectively. Oxide films were synthesized by oxygen-assisted MBE 2.1, i.e., co-depositing Ni, Co or Fe onto Ru at elevated temperature (1150 K) in a molecular oxygen atmosphere (1×10^{-6} mbar). Dosers were previously calibrated by measuring the time needed to complete a monolayer on the W(110) and Ru(0001) surfaces respectively. Typical rates used in the experiments were around $1.6 \times 10^{-3} \text{ ML}_{\text{Ru}}$ (where 1 ML_{Ru} is defined as $1.4 \times 10^{19} \text{ atoms/m}^2$).

Growth was performed during (in-situ) observation by LEEM in order to optimize the growth parameters such as substrate temperature, evaporator flux and oxygen partial pressure. After the growth process, the sample was cooled down to room temperature in an oxygen atmosphere. The synchrotron experiments were typically performed a few days after growth. Before measurements, the sample was flashed up to 900 K in 10^{-6} mbar oxygen atmosphere to remove adsorbates while avoiding a possible reduction of the film.

2.4 References

- [1] M. A. Herman and H. Sitter. *Molecular Beam Epitaxy: Fundamentals and Current Status*. 2012. doi:10.1007/978-3-642-80060-3.
- [2] M. S. Jilani, A. A. and A. Hosny Hammad. Advance Deposition Techniques for Thin Film and Coating. *Modern Technologies for Creating the Thin-film Systems and Coatings*, 2017. doi:10.5772/65702.
- [3] J. A. Venables. *Introduction to Surface and Thin Film Processes*. 2000. doi:10.1017/CB09780511755651.
- [4] E. Bauer and H. Poppa. Recent advances in epitaxy. *Thin Solid Films*, 1972. doi:10.1016/0040-6090(72)90412-9.
- [5] H. Ibach and H. Lüth. Structure of Solid Matter. In *Solid-State Physics: An Introduction to Principles of Materials Science*, pages 21–49. Springer, 2009. doi:10.1007/978-3-540-93804-0_2.
- [6] M. Prutton. *Introduction to Surface Physics*. Oxford University Press, 1994.

-
- [7] E. Bauer. Low energy electron microscopy. *Rep. Prog. Phys.*, 1994. doi:
[10.1088/0034-4885/57/9/002](https://doi.org/10.1088/0034-4885/57/9/002).
- [8] E. Bauer. *Surface Microscopy with Low Energy Electrons*. Springer-Verlag, 2014. doi:
[10.1007/978-1-4939-0935-3](https://doi.org/10.1007/978-1-4939-0935-3).
- [9] R. M. Tromp. Low-energy electron microscopy. *IBM J. Res. Dev.*, 2000. doi:
[10.1147/rd.444.0503](https://doi.org/10.1147/rd.444.0503).
- [10] E. Bauer. LEEM Basics. *Surf. Rev. Lett.*, 1998. doi:
[10.1142/S0218625X98001614](https://doi.org/10.1142/S0218625X98001614).
- [11] A. Locatelli et al. Photoemission electron microscopy with chemical sensitivity: SPELEEM methods and applications. *Surf. Interface Anal.*, 2006. doi:
[10.1002/sia.2424](https://doi.org/10.1002/sia.2424).
- [12] M. S. Altman. Trends in low energy electron microscopy. *J. Phys. Condens. Matter*, 2010. doi:
[10.1088/0953-8984/22/8/084017](https://doi.org/10.1088/0953-8984/22/8/084017).
- [13] W. Teliëps and E. Bauer. The $(7 \times 7) \leftrightarrow (1 \times 1)$ phase transition on Si(111). *Surf. Sci.*, 1985. doi:
[https://doi.org/10.1016/0039-6028\(85\)90890-8](https://doi.org/10.1016/0039-6028(85)90890-8).
- [14] W. Chung and M. Altman. Step contrast in low energy electron microscopy. *Ultramicroscopy*, 1998. doi:
[https://doi.org/10.1016/S0304-3991\(98\)00043-6](https://doi.org/10.1016/S0304-3991(98)00043-6).
- [15] M. Altman et al. Quantum size effect in low energy electron diffraction of thin films. *Appl. Surf. Sci.*, 2001. doi:
[https://doi.org/10.1016/S0169-4332\(00\)00644-9](https://doi.org/10.1016/S0169-4332(00)00644-9).
- [16] T. O. Mendes et al. Cathode lens spectromicroscopy: methodology and applications. *Beilstein J. Nanotechnol.*, 2014. doi:
[10.3762/bjnano.5.198](https://doi.org/10.3762/bjnano.5.198).
- [17] M. A. VanHove et al. *Low-Energy Electron Diffraction: Experiment, Theory and Surface Structure Determination*. 2012. doi:
[10.1007/978-3-642-82721-1](https://doi.org/10.1007/978-3-642-82721-1).
- [18] G. Koster et al. Growth studies of heteroepitaxial oxide thin films using reflection high-energy electron diffraction (RHEED). In *Epitaxial Growth of Complex Metal Oxides*, Woodhead Publishing Series in Electronic and Optical Materials, pages 3–29. 2015. doi:
[10.1016/B978-1-78242-245-7.00001-4](https://doi.org/10.1016/B978-1-78242-245-7.00001-4).
- [19] C. J. Davisson and L. H. Germer. Reflection of Electrons by a Crystal of Nickel. *Proc Natl Acad Sci USA*, 1928.
- [20] E. J. Scheibner et al. Apparatus for Direct Observation of Low-Energy Electron Diffraction Patterns. *Rev. Sci. Instrum.*, 1960. doi:
[10.1063/1.1716903](https://doi.org/10.1063/1.1716903).

- [21] H. Ibach and H. Lüth. Diffraction from Periodic Structures. In *Solid-State Physics: An Introduction to Principles of Materials Science*, pages 51–82. Springer, 2009. doi:[10.1007/978-3-540-93804-0_3](https://doi.org/10.1007/978-3-540-93804-0_3).
- [22] M. P. Seah and W. A. Dench. Quantitative electron spectroscopy of surfaces: A standard data base for electron inelastic mean free paths in solids. *Surf. Interface Anal.*, 1979. doi:[10.1002/sia.740010103](https://doi.org/10.1002/sia.740010103).
- [23] C. Kittel. *Introduction to Solid State Physics*. 2004.
- [24] R. I. Masel. *Principles of Adsorption and Reaction on Solid Surfaces*. 1996.
- [25] M. Prutton. *Surface physics*. 1983.
- [26] K. Oura et al. *Surface Science: An Introduction*. Advanced Texts in Physics. Springer-Verlag, 2003. doi:[10.1007/978-3-662-05179-5](https://doi.org/10.1007/978-3-662-05179-5).
- [27] T. Schmidt et al. SPELEEM: Combining LEEM and Spectroscopic Imaging. *Surf. Rev. Lett.*, 1998. doi:[10.1142/S0218625X98001626](https://doi.org/10.1142/S0218625X98001626).
- [28] J. Feng and A. Scholl. Photoemission Electron Microscopy (PEEM). In P. W. Hawkes and J. C. H. Spence, editors, *Science of Microscopy*, pages 657–695. Springer, 2007. doi:[10.1007/978-0-387-49762-4_9](https://doi.org/10.1007/978-0-387-49762-4_9).
- [29] T. O. Menten and A. Locatelli. Angle-resolved X-ray photoemission electron microscopy. *J Electron Spectrosc*, 2012. doi:[10.1016/j.elspec.2012.07.007](https://doi.org/10.1016/j.elspec.2012.07.007).
- [30] R. M. Tromp et al. A new aberration-corrected, energy-filtered LEEM/PEEM instrument. i. principles and design. *Ultramicroscopy*, 2010. doi:<https://doi.org/10.1016/j.ultramicro.2010.03.005>.
- [31] L. Aballe et al. The ALBA spectroscopic LEEM-PEEM experimental station: layout and performance. *J Synchrotron Radiat*, 2015. doi:[10.1107/S1600577515003537](https://doi.org/10.1107/S1600577515003537).

3 Magnetic spectroscopy using x-rays

In the following chapter X-ray absorption spectroscopy (XAS) and its applications for magnetic materials will be presented. Since the focus of this thesis lies on ferri- and antiferromagnetic materials, special weight will be put on the detailed description of X-ray magnetic circular and linear dichroism (XMCD and XMLD respectively). We start with a brief summary of terminology associated with absorption effects of X-rays in matter. Further, an overview of the concepts underlying the various X-ray dichroism effects will be presented.

3.1 Interaction of X-rays with Matter

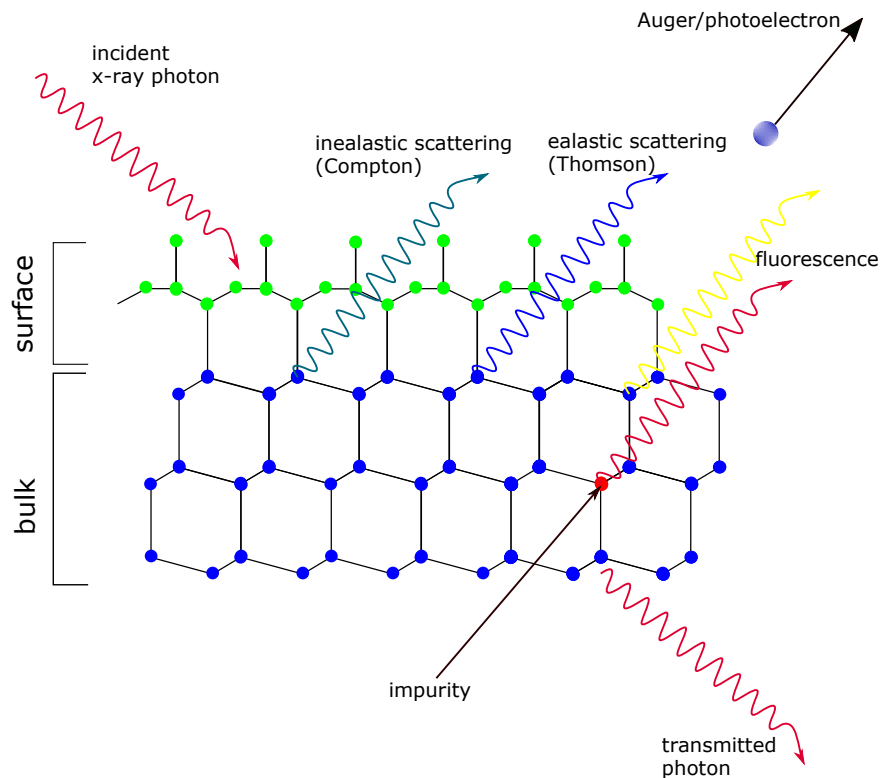


Figure 3.1: Interactions of X-rays with matter

X-rays refers to electromagnetic radiation with zero mass, zero charge and a velocity that is always c , the speed of light. Because x-rays are electrically neutral, they do not lose the energy while interacting with atomic electrons as do charged particles. Their wavelength is ranging from 10 to 0.01 nanometers, corresponding to energies in the range 100 eV to 100 keV. Since the X-ray energy is a broad range, a large number of possible interactions with matter can occur. The cross-section of these interactions depends on the energy of X-rays and the elemental composition of the material, but not much on the chemical properties as the chemical binding energy is lower than the X-ray photon one. The X-rays may be elastically or inelastically scattered, or absorbed, in which case electrons or lower-energy photons can be emitted. If none of the above mentioned effects occur, the photon is transmitted through the sample[1]. The most important interactions of X-rays with matter are sketched in Figure 3.1.

3.2 X-ray Absorption Spectroscopy (XAS)

When an x-ray photon is absorbed by an atom, the energy is transferred to an electron that is expelled from the inner atomic shell, creating a hole in that shell. The process is known as photoelectric absorption (Figure 3.2a). Subsequently, the hole is filled by an electron from the outer shell. The energy released by the electron hopping is transferred to another electron from the outer shell resulting in its emission (as shown in Figure 3.2b). This electron is called an Auger electron. A primary Auger electron on its way to the surface causes a secondary electron cascade (through the inelastic scattering processes) that escape from the sample.

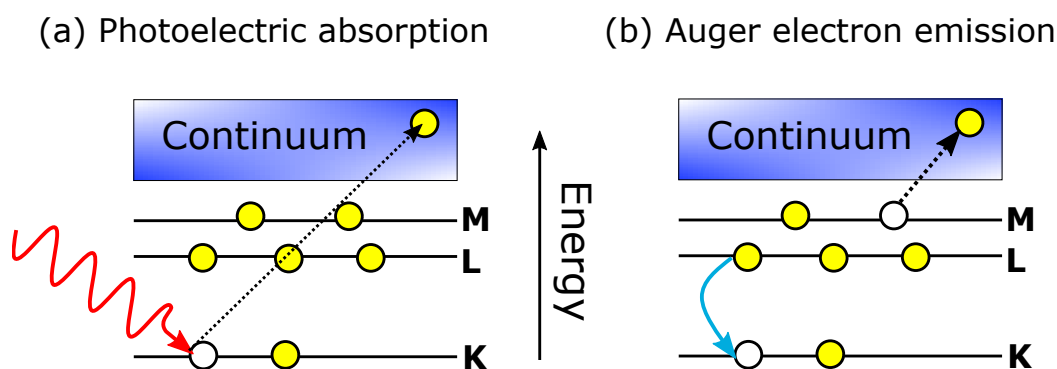


Figure 3.2: Schematic energy diagram of an atom. (a) The photoelectron absorption process. (b) Auger electron emission

The energy and momentum of incoming photons is transferred to the inner shell electron distribution around the atom. Thus, it makes an the absorption process a local probe. The right excitation energy allows to determine element-specific

quantities like the number of electron/holes in specific shells or spin and orbital momenta in magnetic atoms. In the case of solids, where the atom environment is influenced by solid state properties x-ray absorption spectroscopy can be then applied to study the local changes of crystal fields, orbital symmetry or magneto-crystalline anisotropy[2].

Experimentally, X-ray absorption spectroscopy of solids can be measured in two main different ways: X-ray fluorescence and total electron yield (TEY). The second one is typically used in a soft X-ray region and technically is simpler to perform. The emitted electron yield is measured by an amperometer measuring the electrons flowing back to the sample from the ground. XAS measurements can be also performed in PEEM. In this case the sample illuminated by monochromatic x-ray beam emits a broad spectrum of photoelectrons, including secondary electrons. Thus, the energy analyzer incorporated in PEEM microscope acts as a filter allowing to select secondary electrons and hence to record a XAS spectra. The local absorption spectra are acquired by collecting a sequence of images as a function of photon energy, which can be further processed in order to extract a single spectra from the region of interest on the surface (a more detailed description will be provided in Experimental Part of the thesis).

In transition metals and their oxides, an absorption process occur from the $2p$ core levels of the transition metal atom into its $3d$ states (for example for nickel it would be $2p^63d^8 \rightarrow 2p^53d^9$). The spin-orbit splitting of the $2d$ core shell affects the final shape of XAS spectra, giving rise to a characteristic two peaks structure, corresponding to the L_3 and L_2 absorption edges¹ respectively. In addition to the spin-orbit splitting, exchange and correlation effects can also occur. The interplay between spin-orbit and multiplet splitting leads to more complex shape of the XAS spectra (the so-called multiplet structure), typical for oxides[3]. Comparison of the XAS spectra for Fe, Co and Ni metal and their oxides are presented in Figure 3.3.

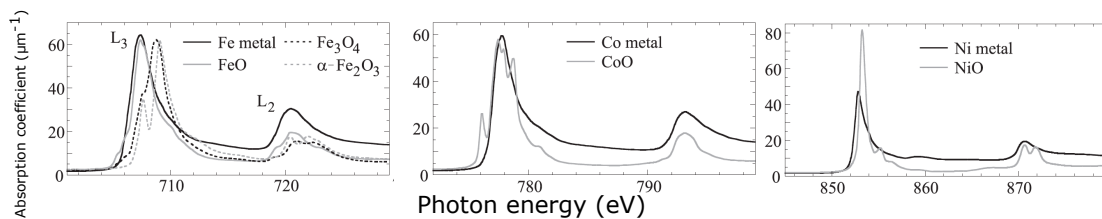


Figure 3.3: XAS spectra for metallic (black curve) Fe, Co and Ni and their oxides (gray). Reprinted from [3].

Multiplet effects play an important role in magnetic X-ray absorption spectroscopy as they can enhance dichroic effects such as linear or circular dichroism.

¹In spectroscopic notation the transition from spin-orbit split p levels to unoccupied d levels are denoted as L_2 (for $2p_{1/2} \rightarrow 3d$ transition) and L_3 ($2p_{3/2} \rightarrow 3d$).

3.3 Dichroism

The concept of dichroism comes from mineralogy and literally means "two-colors". In the optical approach it describes the effect of a solid changing color upon irradiation of light of different incidence angle or polarization. Nowadays, the term dichroism is more often used to describe the dependence of photon absorption on the polarization. From the microscopic point of view the dichroic effect originates from the spatial anisotropy of the charge or the spin distribution of electrons on an atom. We can distinguish two types of dichroic effect, the nonmagnetic (also called natural) and the magnetic one.

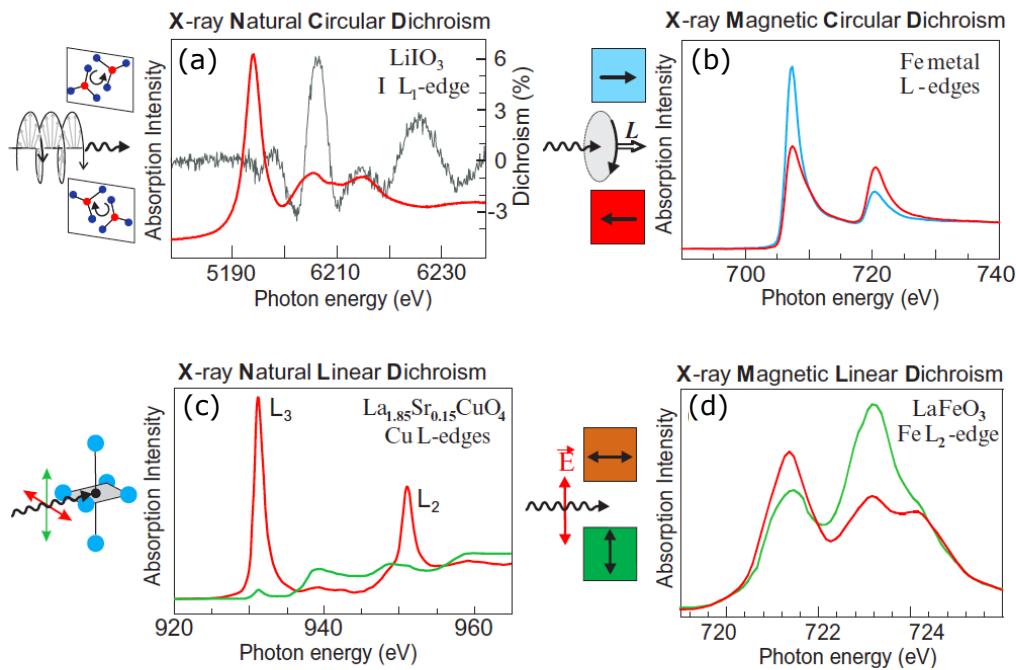


Figure 3.4: a) X-ray Natural Circular Dichroism of single-crystal LiIO_3 [4]. (b) X-ray Magnetic Circular Dichroism measured at $L_{3,2}$ edge of Fe metal[5]. (c) X-ray Natural Linear Dichroism measured at the Cu-edge in $\text{La}_{1.85}\text{Sr}_{0.15}\text{CuO}_4$ [6]. (d) X-ray Magnetic Linear Dichroism of epitaxial thin films of antiferromagnetic LaFeO_3 [?].

3.3.1 X-ray Natural Circular Dichroism

An X-ray natural circular dichroism effect (XNCD) can be observed in optical biaxial crystals without the inversion symmetry. It may be understood by visualizing the bonding around the absorbing atom that has a handedness in space[4; 7]. Thus,

the X-ray absorption depends whether the handedness of the incoming photons and the charge are the same or opposite. An example of XNCD spectra is presented in Figure 3.4b.

This technique is much less used than XMCD but it presents a fundamental interest giving rise to element specific stereochemical information. Renewed interest on this technique has recently grown as it can be applied to a new materials that present both chirality and magnetism[8–10].

3.3.2 X-ray Magnetic Circular Dichroism

X-ray magnetic circular dichroism (XMCD) is widely used to study magnetic materials (ferro- and ferrimagnetic). An XMCD signal is acquired by measuring the difference of two XAS spectra taken with left and with right circularly polarized light respectively. In comparison with other magnetic characterization techniques XMCD has several advantages:

- It is element specific, it allows to study the valency, the site symmetry and magnetization of each element;
- It provides information on the spin and orbital moment separately (other techniques like neutron scattering are sensitive to the total magnetization);
- It is very sensitive, it allows to determine magnetic moments² and study nano-scale structures (multilayers, thin films).

In ferromagnetic materials the exchange interaction splits the valence band into two bands of spin-up and spin-down electrons (Stoner model) Figure 3.5 (left panel). Thus, the spin moment, which is given by the imbalance of spin-up and spin-down electrons, has non-zero value (equivalently, by the imbalance of spin-up and spin-down holes - states above the Fermi level). By knowing that the XAS intensity is proportional to the number of holes, one can make it spin-dependent if circularly polarized photons are used. Circularly polarized photons (right RCP and left LCP) transfer their angular momentum $+\hbar$ and $-\hbar$ respectively to the photoelectron as a spin or angular moment, or both. For transition metals photoelectrons originate from spin-orbit-split level $p_{3/2}$ (L_3 edge), then the angular momentum of photon is transferred in part to the spin. The two levels $p_{3/2}$ (L_3) and $p_{1/2}$ (L_2) have opposite spin-orbit coupling, thus transferred spins have opposite sign at both edges. One important thing to be mentioned that the spin-flop is forbidden in electric dipole transition. Thus the spin-up (spin-down) electrons from the p core shell can be only excited into spin-up (spin-down) d hole states. Hence, in the second step of the x-ray absorption, the exchange split valence state acts as a detector for spins excited by

²It works quite well for transition metal compounds. However, for the light rare earth elements (less than half filled f shells) the deviation in the spin sum rule is larger than 100%.

photoelectrons and the transition intensity is proportional to the number of holes (at a given spin) of empty d states. The maximum dichroic effect is obtained when the photon spin is aligned with magnetization direction[11; 12]. This is schematically presented for the Fe $L_{3,2}$ absorption spectra in Figure 3.5 (right panel).

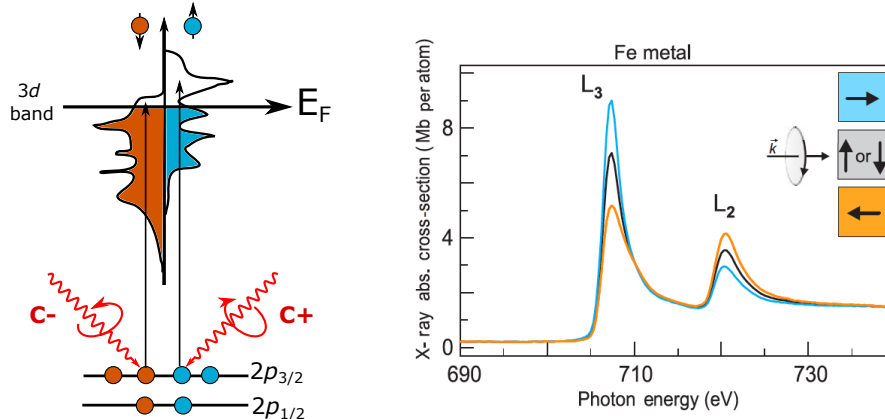


Figure 3.5: The XMCD effect illustrated for L-edge absorption in metallic Fe. (left panel) Schematic illustration of spin-up and spin-down states. (right) Experimental XAS spectra measured at $L_{3,2}$ edge of Fe with left (orange) and right (blue) circular polarized light (reprinted from [11]).

When considering XMCD, it has to be pointed out that the size of this effect is influenced by three parameters:

- the degree of circular polarization P ,
- the value of magnetic moment for a given shell (for transition metals $3d$) $\langle m \rangle$,
- the angle θ between the direction of photon angular momentum L and the magnetic moment m

It can be summarize by the following formula:

$$I_{XMCD} \propto P \cdot \vec{m} \cdot \vec{L} \propto P \langle m \rangle \cos \theta \quad (3.1)$$

The situation is quite different for the K-edge (e.g. XAS measured at the O edge). The excitation of the photoelectron from the $1s$ state transfers only angular momentum $+\hbar$ or $-\hbar$. The orbital angular momentum of photoelectron is detected once there is imbalance in the valence band empty states with quantum number $+m$ and $-m$. If the valence shell does not possess an orbital momentum, photoelectrons that transfer orbital moment $+\hbar$ or $-\hbar$ cannot be distinguished and no dichroic effect will be observed[13; 14].

The XMCD spectra are obtained by taking the difference of the two XAS spectra with opposite circular polarizations. For this reason XMCD experiments are conducted at synchrotron where tunable high-brightness X-ray beams are provided. In addition a special type of insertion devices (undulator) allows for variable polarization (circular or linear) of the photon beam. Typically XMCD spectra are obtained by measuring the absorption spectra in total electron yield mode. The sample is positioned in the center of magnet with the field axis aligned along the horizontal beam directions. The XAS spectra are recorded in magnetic field (M^+ or M^-) for right μ^+ and left μ^- circularly polarized X-rays, normalized by the incoming X-ray beam intensity (I_0), measured by grid in front of the sample. Further, the XMCD spectra are extracted by applying the following formula:

$$\begin{aligned} XMCD(M^+) &= XAS(M^+, \mu^+) - XAS(M^+, \mu^-) \\ XMCD(M^-) &= XAS(M^-, \mu^+) - XAS(M^-, \mu^-) \end{aligned} \quad (3.2)$$

The final XMCD spectra is an average of two spectra defined in Equation 3.2 in order to remove non-magnetic contributions.

An alternative method to obtain the XMCD spectra is the XPEEM microscope (section 2.2.3). In comparison to TEY mode, in XPEEM the measurements under an applied magnetic field are limited. Thus, most of the XAS spectra with two opposite circular polarization are measured in remanence. Although, measurements of XMCD spectra in XPEEM have one important advantage: it allows to measure the dichroic signal from a single domain area. Aside from the XMCD spectra, XPEEM images can be used to obtain the magnetization distribution on a magnetic surface[15; 16]. This method was followed for nickel ferrite thin films which are the subject of the Chapter 4.

XMCD sum rules

For understanding the macroscopic magnetic properties of matter it is necessary to know spin and orbital moments of electron of an atom in a sample. These values can be obtained by applying different techniques, although their determination with element specificity remains a difficult task. Based on X-ray absorption spectroscopy and its associated magnetic circular dichroism three magneto-optical sum rules have been established. They link polarization dependent resonance intensity with the number of holes N_h per atom, the spin (m_s) and orbital (m_o) magnetic moment per atom[5].

1. The charge sum rule - it describes the relation between the measured averaged X-ray absorption intensity of a core to valence to the number of holes N_h per atom. It is defined as:

$$\langle I \rangle = r \cdot N_h \quad (3.3)$$

2. The orbital moment sum rule - links the average orbital moment per atom

with the angle averaged dichroism intensities according to equation:

$$m_{orb}[\mu_B/atom] = -\frac{4q \cdot N_h}{r} \quad (3.4)$$

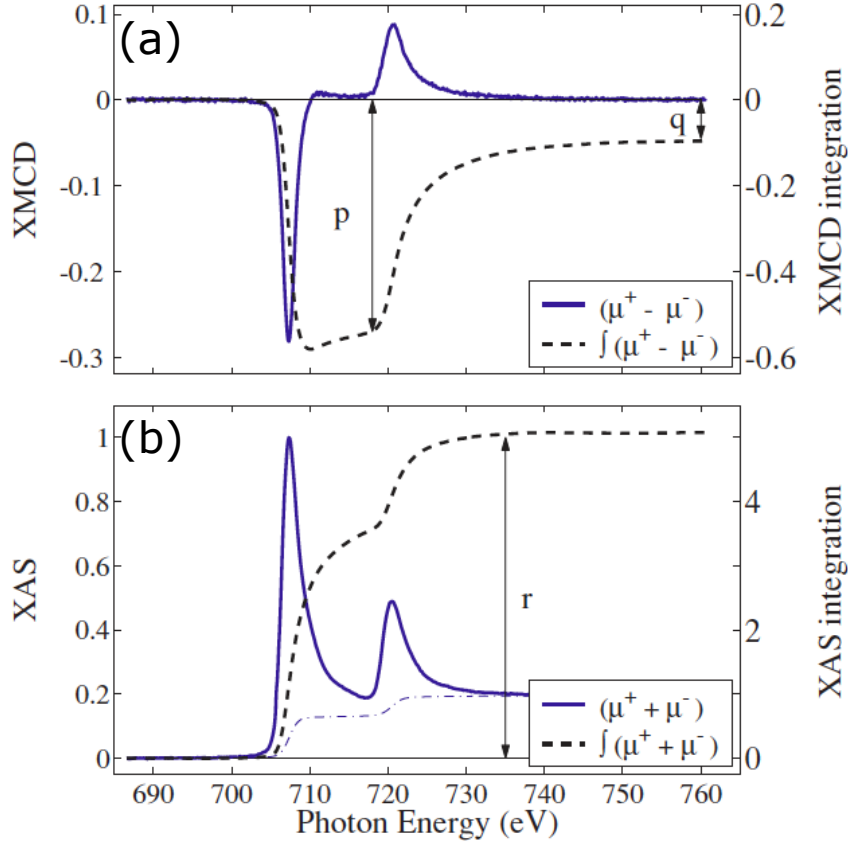


Figure 3.6: Fe XMCD and summed XAS spectra and their integration. The dotted line shown in Figure 3.6b is a step like function for the background correction before en integration. Reprinted from[5].

3. The spin moment sum rule - links the spin moment per atom with the angle averaged dichroism intensities.

$$m_{spin}[\mu_B/atom] = -\frac{6p - 4q}{r} \cdot \left(1 + \frac{7 \langle T_Z \rangle}{2 \langle S_Z \rangle}\right) \cdot N_h \quad (3.5)$$

$\langle T_Z \rangle$ is the expected value of the magnetic dipole operator that reflects a quadrupole term in the anisotropic spin density of the $3d$ final state. This term is zero for a system with cubic or higher symmetry. $\langle T_Z \rangle$ contributes to

the magnetic dichroism in a systems like epitaxial strained films. $\langle S_Z \rangle$ is equal to half of the m_{spin} in Hartree atomic units³[5; 17].

p , q and r are given by the following formulas:

$$p = \int_{L_3} (\mu^+ - \mu^-) dE \quad (3.6)$$

$$q = \int_{L_3+L_2} (\mu^+ - \mu^-) dE \quad (3.7)$$

$$r = \frac{1}{2} \int_{L_3+L_2} (\mu^+ + \mu^-) dE \quad (3.8)$$

where the $L_{3,2}$ denote the integration range. The procedure to obtain spin and orbital magnetic moment is shown in Figure 3.6 using the example of a Fe XAS and XMCD spectra[5].

Despite its versatility, a number of approximations have been made which affect the final accuracy of the sum rule analysis. First of all, other than $2p \rightarrow 3d$ transitions like for example $2p \rightarrow 4s$ have been neglected. Another issue is that it does not take into account the intra atomic hybridization. Experimentally, the other transition and intra atomic hybridization have to be accounted by subtracting background from XAS spectra. The background modelled by a two step arctangent function, to be subtracted from the summed XAS spectrum, as shown in Figure 3.6a. Furthermore, the post-edge background of the edge-jump that is very often difficult to determine because of the multiple-scattering resonance in the signal (so called NEXAFS or EXAFS scattering). In practice, determination of orbital moment m_{orb} requires high quality data and precise data treatment. In many cases the q value is very small and the error level of orbital moment becomes larger.

Next, an important limitation is coming from the partial overlap of the spin-orbit split edges, assumed in the model to be completely separated. This overlap affects mainly the spin-moment, since its contribution to the XMCD signal has opposite sign at both edges. It is also worth to mention that the number of holes/electrons is not known directly in the $3d$ states and it has to be obtained from theoretical calculations. All mentioned limitations affects the final value of spin and orbital moment and even with really careful evaluation it will not allow to yield these values with the error smaller than 10%.

3.3.3 X-ray Natural Linear Dichroism (XNLD)

Another powerful technique from the dichroism family is X-ray Linear Dichroism (XLD). It is caused by several different microscopic mechanisms. We can distinguish

³Hartree atomic units are the system of natural units useful for atomic physics calculations. In this system the fundamental physical constant like electron mass or elementary charge are unity.

two main types of linear dichroism: X-ray Natural Linear Dichroism (XNLD) and X-ray Magnetic Linear Dichroism. The first one, is due to the anisotropic charge distribution, while the second one, XMLD, is a combination of different effects. The origin of XMLD will be a subject of next paragraph 3.3.4. We turn now to the description of natural linear dichroism.

X-ray Natural Linear Dichroism (also called crystal-field dichroism) arises from the anisotropic (nonspherical) charge distribution at the absorbing atom due to bonding. In such a systems certain orbitals are selectively populated as their energy becomes nondegenerate. One can now probe the empty (molecular) valence states by using the "search light effect"[18]. In a standard X-ray absorption experiment the core shell electrons are excited into empty valence states. For linear polarized XAS the electric field vector \mathbf{E} of the incoming photons acts as search light. Thus the transition intensity from the core shell to valence state will be proportional to the number of empty valence states in the direction of \mathbf{E} . It can be nicely understood with a symmetry simple example. Lets consider the excitation from a s orbital to p orbital. There are three different orbitals one can excite to - p_x, p_y, p_z . If we now use z polarized light then the maximum intensity will be for the transition from s orbital to p_z orbital. Moreover the ratio of intensity with x, y or z polarized light will be equal to the ratio of holes in the p_x, p_y, p_z orbital[19; 20].

An application of XNLD illustrated by Chen et al.[6] for excitation from p to d shell can be found in Figure 3.4c. An example is shown for the Cu L-edge of high-temperature superconductor $\text{La}_{1.85}\text{Sr}_{0.15}\text{CuO}_4$. High T_C superconductors have a CuO plane with the valnce of the Cu d^9 . The one hole at the Cu site is in the in-plane $d_{x^2-y^2}$ orbital. This means that when the \mathbf{E} lies in the x, y plane a large peak-like transition will be observed to this orbital. The resonance is absent for z polarized light, since there are no empty states in the perpendicular direction.

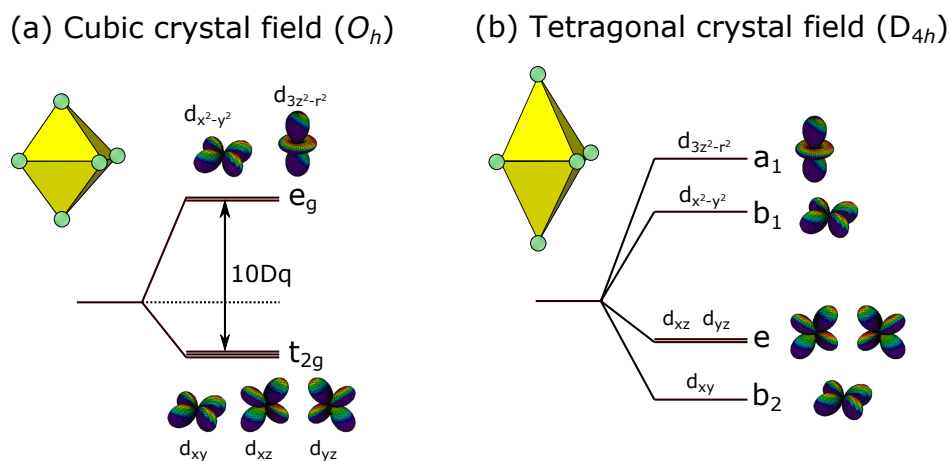


Figure 3.7: Crystal field splitting in (a) cubic crystal field and (b) tetragonal crystal field.

Not only orbital ordering can lead to linear dichroism. The polarization dependent XAS also allows to study the splitting between orbitals and measure the energy of the splitting. As an example, we will show the crystal field dichroism for Ni^{2+} ion. In octahedral symmetry O_h (when the Ni ion is surrounded by 6 oxygen atoms) the crystal field splits into two levels e_g and t_{2g} as shown in Figure 3.7. By summing up two contributions from e_g and t_{2g} leads to spherical symmetry, corresponding to a full shell. Thus no dichroism will be observed. Once the crystal symmetry is lowered e.g. tetragonal, with compression or elongation along the z -axis, the formerly degenerated orbitals of e_g level split into two states a_1 (d_{z^2} orbital) and b_1 ($d_{x^2-y^2}$ orbital), while the t_{2g} orbitals splits into two degenerate e (d_{xz} , d_{yz}) and b_2 (d_{xy}) (Figure 3.7). The energy splitting due to the tetragonal distortion can be observed in the polarized dependent XAS spectra. By using z polarized light one can excite d_{z^2} orbital, but not into $d_{x^2-y^2}$. With x polarized light, the opposite is true. This is clearly visible in the XAS spectra of Ni^{2+} of 1 ML strained NiO films on MgO, where the two spectra taken at different polarizations are shifted to each other (Figure 3.8). The difference observed at the L_3 edge is therefore equal to the energy splitting between $d_{x^2-y^2}$ and the d_{z^2} orbital. In chapter 5 we will discuss this in more detail in the frame of mixed nickel-cobalt oxide thin films[21].

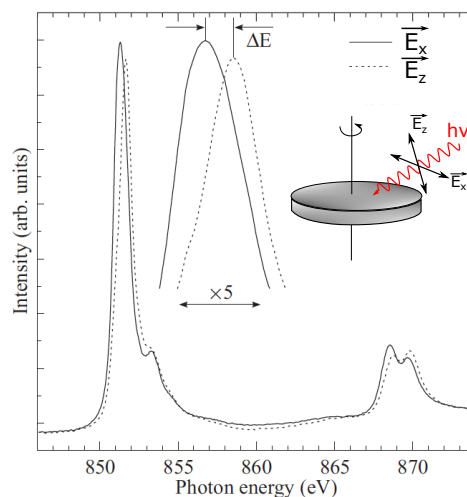


Figure 3.8: Linear dichroism in NiO due to the crystal field splitting. The energy difference ΔE is equal to the splitting energy between $d_{x^2-y^2}$ and d_{z^2} orbital. Reprinted from [21].

3.3.4 X-ray Magnetic Linear Dichroism (XMLD)

X-ray magnetic linear dichroism (XMLD) can be used to map domains in antiferromagnetic materials as XMCD for ferromagnetic ones. In many cases it coexists with natural linear dichroism and distinguish both contributions is often very tricky. There is a major difference between natural and magnetic linear dichroism: XMLD

3 Magnetic spectroscopy using x-rays

occur only in the presence of magnetic alignment and vanishes at the transition temperature (from anti- to paramagnetic state - Néel temperature), or for paramagnetic materials in the absence of external magnetic field.

The XMLD signal can arise from different effects. It may arise from a pure spin effect due to the exchange-correlation effects but also from nonspherical distortion of the atomic charge caused by spin-orbit interaction[22].

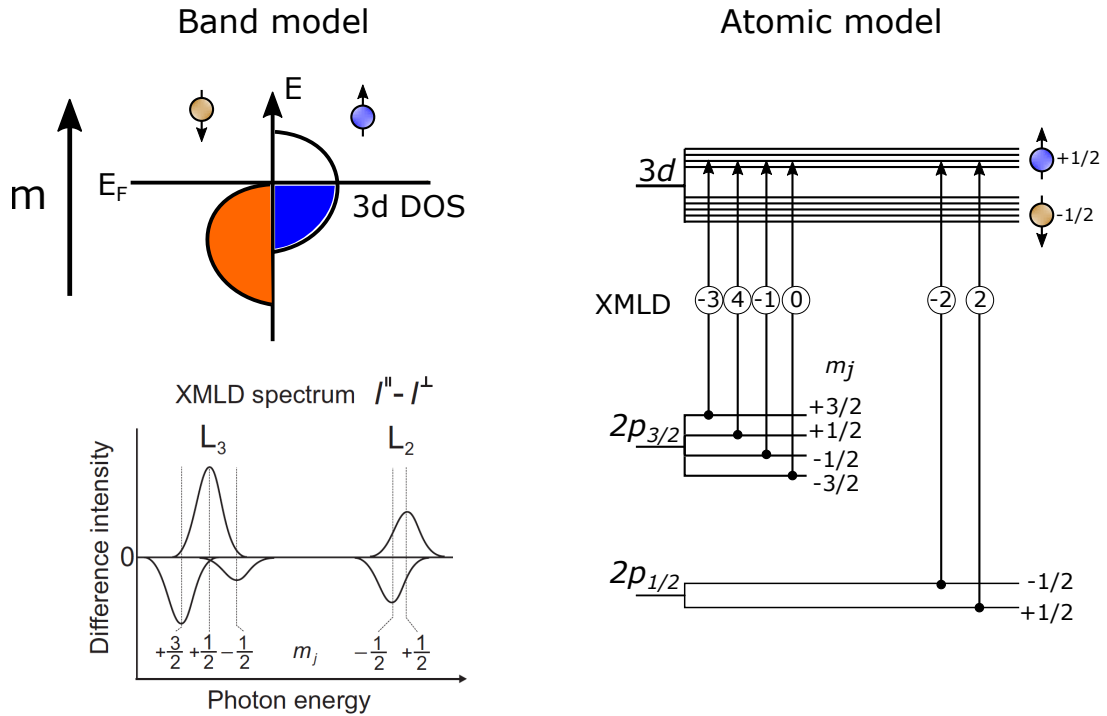


Figure 3.9: L-edge X-ray absorption process of linearly polarized photons. For the d shell we show the comparison between a band model (Stoner) (upper left) and atomic model (right panel). Resulting XMLD spectra is drawn in the lower left[11].

In order to illustrate how XMLD arises from spin-only effects we will consider a simple model. The model of magnetic linear dichroism can be described by a Stoner-like band model already used for the XMCD. We assume again the splitting of $3d$ band for majority (spin-up) and minority (spin-down) band, without taking into account the crystallographic structure of the sample. This simplify the symmetry of the problem to be axial: the XMLD signal will be only dependent on the angle between magnetization and photon polarization vector[12]. However, as it will be shown later, there can be additional effects caused by the site symmetry of the excited atom due to its surrounding neighbours, which lead to the so called anisotropic XMLD, i.e. spectral shape and magnitude of the XMLD is not only determined

by the relative orientation of magnetic moments and x-ray polarization but their orientations relative to the crystallographic axes has to be taken into account.

An x-ray absorption process with linearly polarized photons is schematically shown in Figure 3.9. In the simple model we have assumed the magnetization direction such that the spin-down band is completely filled and spin-up partially unfilled (left panel). The incoming X-rays are parallel to the atomic magnetic moment. The exchange interaction of the p state lifts the degeneracy in m_j . The possible transitions are depicted in the right panel. The relative transition intensities $2p_{1/2,3/2} \rightarrow 3d$ in a simple atomic model are calculated by applying the selection rules for dipole radiation, as well as the Fermi's golden rule. The excitation probabilities are given by Clebsch-Gordon coefficients which are the same as for the XMCD and do not take into account the number of unoccupied final states. The resulting XMLD spectrum (difference of two spectra $I_{\parallel} - I_{\perp}$) in the bottom left in Figure 3.9

Note that in order to observe the XMLD in a simple systems as the one presented in Figure 3.9, a large energetic splitting of the core hole m_j has to exist. The exchange splitting of the $2p$ shell in $3d$ transition metals is rather small of the order of 0.1 eV (266 meV for Co), and the detection of XMLD requires high resolution x-ray beamlines. The model described above is a simplification; there are additional effects which influence the final XMLD signal. For strongly correlated systems, as for example transition metal oxides, multiplet effects have to be taken into account.

It has to be pointed out that the simple model described above is incomplete, as it takes into account the exchange splitting of the core hole as an important prerequisite, but do not explain the intrinsic origin of this effect. A more realistic approach assumes that the polarized photon couple to the spatial part of the electron wave function resulting in an orbitally polarized core hole. In the final state this core hole interacts via exchange and correlation with the target shell of the transition. Both effects are responsible for the XMLD, and are related to the magnetic symmetry of the system (crystal field and spin axis, respectively).

In conclusion, there are two important prerequisites for the existence of XMLD: the presence of atomic magnetic moment and the spin-orbit interaction. Thus, in both ferro- and antiferromagnets, the exchange interaction creates a spin magnetic moment and the spin-orbit interaction an orbital magnetic moment locked to both spin moment and the lattice. The only difference between those types of magnetic materials is that ferro- or ferri-magnets are directional since there is a net moment direction while antiferromagnets are axial since all spins lie along a particular axis of the crystal. Both can be studied with XMLD. However, x-ray magnetic linear dichroism is nowadays extensively used to determine the orientation of the AF axis in thin films and near surfaces, and the imaging of antiferromagnetic domains. The latter can be obtain by means of XPEEM[23–27]. XMLD photoemission electron microscopy (XMLD-PEEM) in particular is able to map out the AF contrast down to the nanometre scale (see section 2.2.3). However, to determine the AF domain

vectors from this data one needs to understand the angular dependence of the XMLD in the given material as it will be shown in Chapter 6.

3.3.4.1 Isotropic and anisotropic XMLD

When the symmetry of the final state is not spherical the XAS spectra cannot be described by means of a single angle (between the photon polarization vector \mathbf{E} and magnetization axis \mathbf{S}). In cubic symmetry the angles of \mathbf{E} and \mathbf{S} with respect to the crystalline symmetry of the sample have to be taken into account. Thus, we can differentiate two contributions to XMLD: "isotropic" part that is independent of the material lattice symmetry and "anisotropic", which depends on the crystal symmetry [28; 29].

XMLD in the presence of cubic crystal field

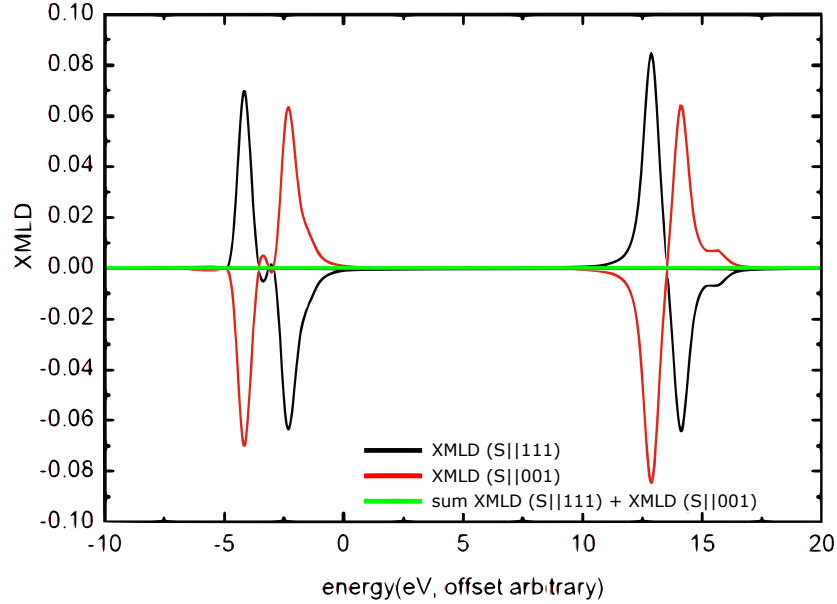


Figure 3.10: Calculated XMLD spectra of (001) and (111) magnetized Ni crystal. Reprinted from [30].

The crystal field of an atom in cubic symmetry (O_h), as already mentioned in 3.3.3, causes a splitting of the $3d$ band into two states e_g and t_{2g} . The classical way to calculate the XMLD spectra $I_{XMLD} = I_{E||S} - I_{E\perp S}$ will only work for the special case that the spin axis \mathbf{S} is aligned along the high symmetry directions [001] (C_4) and [111] (C_3 symmetry). This means that there is only one spectrum $I_{E\perp S}$ for an arbitrary polarization direction in the plane perpendicular to \mathbf{S} . In any other case the XMLD signal cannot be calculated from the aforementioned formula. However, it has to be pointed out that by measuring the XMLD for two different magnetization

orientations, (111) and (001), the spin-polarized part of the e_g and t_{2g} unoccupied partial density of states could be determined for the cubic $3d$ systems[30; 31].

The spectra for two spin axis were modelled theoretically for the transition metals (Fe, Co and Ni). Details of the $L_{3,2}$ XMLD spectra for Ni are shown in Figure 3.10. Surprisingly the XMLD spectra for $S||111$ and $S||001$ are inverse[32]. This is an important fact that will be take into account in our further consideration.

Isotropic XMLD

The classical derivation of XMLD stated that it is due to the magnetically induced charge quadrupole moment that rotates with the spin axis \mathbf{S} . This means that the effect would depend only on the relative orientation of photon polarization \mathbf{E} and spin \mathbf{S} .

Intuitively understanding the origin of xmlD is not simple, but it can be derived rather straightforward from the classical theory of electromagnetism where the absorption intensity of a XAS spectrum can be calculated from the imaginary part of dielectric tensor[33]

$$\mu_{XAS} = -\frac{\omega}{8\pi} \text{Im}\{E^* \cdot \hat{\epsilon} \cdot E\} \quad (3.9)$$

where \mathbf{E} is the incoming photon polarization vector and $\hat{\epsilon}$ a complex dielectric tensor. The dielectric tensor for a system with cubic or higher symmetry is represented by[34]:

$$\hat{\epsilon} = \begin{bmatrix} \epsilon_{xx} & 0 & 0 \\ 0 & \epsilon_{xx} & 0 \\ 0 & 0 & \epsilon_{xx} \end{bmatrix} \quad (3.10)$$

Since the XMLD arises from the charge anisotropies induced by exchange and spin-orbit interaction, the quadrupol moment will be a tensor of rank $k=2$

$$\hat{Q} = \begin{bmatrix} Q_{xx} & Q_{xy} & Q_{xz} \\ Q_{yx} & Q_{yy} & Q_{yz} \\ Q_{zx} & Q_{zy} & Q_{zz} \end{bmatrix} = \begin{bmatrix} 1 - 3x^2 & -3xy & -3xz \\ -3xy & 1 - 3y^2 & -3yz \\ -3xz & -3yz & 1 - 3z^2 \end{bmatrix} \quad (3.11)$$

where $\mathbf{S} = (x, y, z)$ is the unit vector along the spin axis. Thus, the dielectric tensor in the presence of linear dichroism can be rewritten as a combination of isotropic and quadrupole part.

$$\hat{\epsilon} = \hat{\epsilon}_{iso} + q\hat{Q} \quad (3.12)$$

$$\hat{\epsilon} = \begin{bmatrix} \epsilon_{xx} + q(1 - 3x^2) & -3qxy & -3qxz \\ -3qxy & \epsilon_{xx} + q(1 - 3y^2) & -3qxz \\ -3qxz & -3qxz & \epsilon_{xx} + q(1 - 3z^2) \end{bmatrix} \quad (3.13)$$

Orienting \mathbf{S} parallel to z direction makes $\hat{\epsilon}$, diagonal with two independent elements:

$$\hat{\epsilon}_z = \begin{bmatrix} \epsilon_{xx} + q & 0 & 0 \\ 0 & \epsilon_{xx} + q & 0 \\ 0 & 0 & \epsilon_{xx} - 2q \end{bmatrix} = \begin{bmatrix} \epsilon_{\perp} & 0 & 0 \\ 0 & \epsilon_{\perp} & 0 \\ 0 & 0 & \epsilon_{\parallel} \end{bmatrix} \quad (3.14)$$

whereas, orienting the spin parallel to x direction, will result in:

$$\hat{\epsilon}_x = \begin{bmatrix} \epsilon_{\parallel} & 0 & 0 \\ 0 & \epsilon_{\perp} & 0 \\ 0 & 0 & \epsilon_{\perp} \end{bmatrix} \quad (3.15)$$

Consequently, the dielectric tensor for arbitrary spin direction $\mathbf{S} = (x, y, z)$ will look like[34]:

$$\hat{\epsilon}_{MLD} = \begin{bmatrix} \epsilon_{\perp} + (\epsilon_{\parallel} - \epsilon_{\perp})x^2 & (\epsilon_{\parallel} - \epsilon_{\perp})xy & (\epsilon_{\parallel} - \epsilon_{\perp})xz \\ (\epsilon_{\parallel} - \epsilon_{\perp})yx & \epsilon_{\perp} + (\epsilon_{\parallel} - \epsilon_{\perp})y^2 & (\epsilon_{\parallel} - \epsilon_{\perp})yz \\ (\epsilon_{\parallel} - \epsilon_{\perp})zx & (\epsilon_{\parallel} - \epsilon_{\perp})zy & \epsilon_{\perp} + (\epsilon_{\parallel} - \epsilon_{\perp})z^2 \end{bmatrix} \quad (3.16)$$

The two independent elements ϵ_{\parallel} and ϵ_{\perp} of dielectric tensor 3.16 can be measured in the geometries when the spin axis is parallel ($\mathbf{S} \parallel \mathbf{E}$) and perpendicular ($\mathbf{x} \parallel \mathbf{S} \perp \mathbf{E} \parallel z$) to photon polarization vector, respectively. The corresponding XAS spectra are the fundamental spectra. Following equation 3.9 one can calculate the XMLD spectra by using the standard rule[11]:

$$\mu_{MLD} = \mu_{S \parallel E} - \mu_{S \perp E} \quad (3.17)$$

This can be cast into the general XMLD intensity dependence, no matter where \mathbf{S} is pointing:

$$\mu_{MLD} = \epsilon_{\parallel} - \epsilon_{\perp} \propto m^2 \quad (3.18)$$

where m^2 is the squared magnetization of the sample.

The above considerations assume that the quadrupole moment is locked to the spin. Combined with simple mathematics it leads us to the conclusion that the XMLD for cubic or higher symmetry systems will only depend on the relative angle between the spin axis \mathbf{S} and photon polarization vector \mathbf{E} .

Anisotropic XMLD

It has been shown theoretically and experimentally confirmed, that the magnetic linear dichroism does not only depend on the direction of the polarization with respect to the spin but also on the crystalline orientation. It complicates more the analysis of XMLD data and leads to quite different results where e.g. the sign of the MLD spectra can be reversed. This is crucial in order to determine the spin direction of antiferromagnetic domains by means of XMLD PEEM[35; 36].

For cubic symmetry one finds both experimentally and theoretically that the exchange-correlation effects make XMLD anisotropic. Thus, the off diagonal parts of the dielectric tensor $\hat{\epsilon}$ (Equation 3.16) become negative, which is why the set of XMLD spectra for all possible polarizations directions does not rotate along with \mathbf{S} any more[32; 37].

In cubic symmetry the dielectric tensor can be rewritten as:

$$\hat{\epsilon}_{MLD} = \begin{bmatrix} \epsilon^0 + \epsilon_{e_g}^2(x^2 - \frac{1}{3}) & \epsilon_{t_{1u}}^1 z + \epsilon_{t_{2g}}^2 xy & -\epsilon_{t_{1u}}^1 y + \epsilon_{t_{2g}}^2 xz \\ -\epsilon_{t_{1u}}^1 z + \epsilon_{t_{2g}}^2 xy & \epsilon^0 + \epsilon_{e_g}^2(y^2 - \frac{1}{3}) & \epsilon_{t_{1u}}^1 x + \epsilon_{t_{2g}}^2 yz \\ \epsilon_{t_{1u}}^1 y + \epsilon_{t_{2g}}^2 xz & -\epsilon_{t_{1u}}^1 x + \epsilon_{t_{2g}}^2 yz & \epsilon^0 + \epsilon_{e_g}^2(x^2 - \frac{1}{3}) \end{bmatrix} \quad (3.19)$$

where ϵ^0 defines an isotropic spectrum, ϵ^1 the XMCD and ϵ^2 the XMLD spectra respectively. At first we neglect the circular dichroic spectra. Next, the isotropic part of dielectric tensor can be substituted by the following formula $\epsilon^0 = \frac{1}{3}\epsilon_{\parallel} + \frac{2}{3}\epsilon_{\perp}$, where ϵ_{\parallel} defines the magnetic linear dichroic spectrum one measures if the sample is magnetized along the C_4 direction [001] ($S \parallel E \parallel C_4$) and ϵ_{\perp} if the sample is magnetized along the C_3 direction [111] ($S \parallel C_3 \perp E \parallel C_4$). For small deviations from spherical symmetry $\epsilon_{t_{2g}}^2$ must be roughly equal to $\epsilon_{e_g}^2$. However this true just for some special cases as e.g. in NiO (Figure 3.10) where the XMLD spectra at L_2 edge are reversed $\epsilon_{t_{2g}}^2 = -\epsilon_{e_g}^2$. Moreover $\epsilon_{e_g}^2 = \epsilon_{\parallel} - \epsilon_{\perp}$ [37].

With the previous assumptions we arrive to the much simpler form of the dielectric tensor:

$$\hat{\epsilon}_{MLD} = \begin{bmatrix} \epsilon_{\perp} + (\epsilon_{\parallel} - \epsilon_{\perp})x^2 & -(\epsilon_{\parallel} - \epsilon_{\perp})xy & -(\epsilon_{\parallel} - \epsilon_{\perp})xz \\ -(\epsilon_{\parallel} - \epsilon_{\perp})yx & \epsilon_{\perp} + (\epsilon_{\parallel} - \epsilon_{\perp})y^2 & -(\epsilon_{\parallel} - \epsilon_{\perp})yz \\ -(\epsilon_{\parallel} - \epsilon_{\perp})zx & -(\epsilon_{\parallel} - \epsilon_{\perp})zy & \epsilon_{\perp} + (\epsilon_{\parallel} - \epsilon_{\perp})z^2 \end{bmatrix} \quad (3.20)$$

This equation shows that in cubic symmetry (in some special cases) two fundamental spectra are still sufficient to describe the effect of an arbitrary direction of S and therefore determine the spin axis of antiferromagnetic systems. This model will be employed in the analysis presented in Chapter 6.

3.4 References

- [1] D. M. Jens Als-Nielsen. *X-rays and their interaction with matter*. 2011. doi:10.1002/9781119998365.ch1.
- [2] P. Willmott. *The Interaction of X-rays with Matter*. 2011. doi:10.1002/9781119970958.ch2.
- [3] T. J. Regan et al. Chemical effects at metal/oxide interfaces studied by x-ray-absorption spectroscopy. *Phys. Rev. B*, 2001. doi:10.1103/PhysRevB.64.214422.
- [4] J. Goulon et al. X-ray natural circular dichroism in a uniaxial gyrotropic single crystal of LiIO_3 . *J. Chem. Phys.*, 1998. doi:10.1063/1.476046.
- [5] J. Stöhr and H. König. Determination of spin- and orbital-moment anisotropies in transition metals by angle-dependent x-ray magnetic circular dichroism. *Phys. Rev. Lett.*, 1995. doi:10.1103/PhysRevLett.75.3748.
- [6] C. T. Chen et al. Out-of-plane orbital characters of intrinsic and doped holes in $\text{La}_{2-x}\text{Sr}_x\text{CuO}_4$. *Phys. Rev. Lett.*, 1992. doi:10.1103/PhysRevLett.68.2543.
- [7] L. Alagna et al. X-Ray Natural Circular Dichroism. *Phys. Rev. Lett.*, 1998. doi:10.1103/PhysRevLett.80.4799.
- [8] R. D. Peacock and B. Stewart. Natural Circular Dichroism in X-ray Spectroscopy. *J. Phys. Chem. B*, 2001. doi:10.1021/jp001946y.
- [9] R. Sessoli et al. Strong magneto-chiral dichroism in a paramagnetic molecular helix observed by hard X-rays. *Nat. Phys.*, 2015. doi:10.1038/nphys3152.
- [10] G. van der Laan and A. I. Figueroa. X-ray magnetic circular dichroism—A versatile tool to study magnetism. *Coord. Chem. Rev.*, 2014. doi:10.1016/j.ccr.2014.03.018.
- [11] J. Stöhr and H. C. Siegmann. *Magnetism: From Fundamentals to Nanoscale Dynamics*. Springer Series in Solid-State Sciences. Springer-Verlag, 2006. doi:10.1007/978-3-540-30283-4.
- [12] J. Stöhr. X-ray magnetic circular dichroism spectroscopy of transition metal thin films. *J. Electron Spectros.*, 1995. doi:10.1016/0368-2048(95)02537-5.
- [13] A. Koide and T. Yokoyama. Effects of spin-orbit interaction in chromium on oxygen K-edge x-ray magnetic circular dichroism spectra in CrO_2 . *Phys. Rev. B*, 2017. doi:10.1103/PhysRevB.96.144419.

-
- [14] D. J. Huang et al. Orbital magnetic moments of oxygen and chromium in CrO₂. *Phys. Rev. B*, 2002. doi:10.1103/PhysRevB.66.174440.
- [15] O. Sandig et al. Imaging magnetic responses of nanomagnets by XPEEM. *J. Electron Spectrosc.*, 2012. doi:10.1016/j.elspec.2012.07.005.
- [16] A. Locatelli and E. Bauer. Recent advances in chemical and magnetic imaging of surfaces and interfaces by XPEEM. *J. Phys. Condens. Matter*, 2008. doi:10.1088/0953-8984/20/9/093002.
- [17] P. Carra et al. X-ray circular dichroism and local magnetic fields. *Phys. Rev. Lett.*, 1993. doi:10.1103/PhysRevLett.70.694.
- [18] J. Stöhr. *NEXAFS Spectroscopy*. Springer Series in Surface Sciences. Springer-Verlag, 1992. doi:10.1007/978-3-662-02853-7.
- [19] M. Sacchi et al. Crystal field induced linear dichroism in the 3d X-ray absorption of rare-earths. *Solid State Commun.*, 1992. doi:10.1016/0038-1098(92)90849-5.
- [20] M. Sacchi et al. Surface X-ray dichroism for crystal field studies. *Appl. Surf. Sci.*, 1992. doi:10.1016/0169-4332(92)90205-C.
- [21] M. W. Haverkort et al. Magnetic versus crystal-field linear dichroism in NiO thin films. *Phys. Rev. B*, 2004. doi:10.1103/PhysRevB.69.020408.
- [22] M. Haverkort. Spin and orbital degrees of freedom in transition metal oxides and oxide thin films studied by soft x-ray absorption spectroscopy. 2005.
- [23] P. Wadley et al. Control of antiferromagnetic spin axis orientation in bilayer Fe/CuMnAs films. *Scientific Reports*, 2017. doi:10.1038/s41598-017-11653-8.
- [24] S.-W. Cheong et al. Seeing is believing: visualization of antiferromagnetic domains. *npj Quantum Materials*, 2020. doi:10.1038/s41535-019-0204-x.
- [25] J. Stöhr et al. Images of the antiferromagnetic structure of a nio(100) surface by means of x-ray magnetic linear dichroism spectromicroscopy. *Phys. Rev. Lett.*, 1999. doi:10.1103/PhysRevLett.83.1862.
- [26] A. Scholl et al. X-ray photoemission electron microscopy, a tool for the investigation of complex magnetic structures (invited). *Review of Scientific Instruments*, 2002. doi:10.1063/1.1445485.
- [27] J. Lüning et al. Determination of the antiferromagnetic spin axis in epitaxial

- lafe₃ films by x-ray magnetic linear dichroism spectroscopy. *Phys. Rev. B*, 2003. doi:10.1103/PhysRevB.67.214433.
- [28] G. van der Laan and E. Arenholz. Anisotropic X-ray magnetic linear dichroism. *EPJ ST*, 2009. doi:10.1140/epjst/e2009-00991-x.
- [29] G. van der Laan et al. Anisotropic x-ray magnetic linear dichroism and spectromicroscopy of interfacial Co/NiO(001). *Phys. Rev. B*, 2011. doi:10.1103/PhysRevB.83.064409.
- [30] I. Krug. *Magnetic Proximity Effects in Highly-ordered Transition Metal Oxide Heterosystems studied by Soft X-Ray Photoemission Electron Microscopy*. PhD thesis, 2008.
- [31] G. van der Laan. Anisotropic X-ray Magnetic Linear Dichroism. In E. Beaupaire et al., editors, *Magnetism and Synchrotron Radiation: Towards the Fourth Generation Light Sources*, Springer Proceedings in Physics, pages 239–256, 2013. Springer International Publishing. doi:10.1007/978-3-319-03032-6_8.
- [32] J. Kuneš and P. M. Oppeneer. Anisotropic x-ray magnetic linear dichroism at the L_{2,3} edges of cubic Fe, Co, and Ni: *Ab initio* calculations and model theory. *Phys. Rev. B*, 2003. doi:10.1103/PhysRevB.67.024431.
- [33] V. M. Agranovich and V. Ginzburg. *Crystal Optics with Spatial Dispersion, and Excitons*. Springer Series in Solid-State Sciences. Springer-Verlag, Berlin Heidelberg, 1984. doi:10.1007/978-3-662-02406-5.
- [34] T. Hibma and M. W. Haverkort. *Antiferromagnetic Oxide Films on Nonmagnetic Substrates*. 2010. doi:10.1002/9783527630370.ch4.
- [35] I. Krug et al. Impact of interface orientation on magnetic coupling in highly ordered systems: A case study of the low-indexed Fe₃O₄/NiO interfaces. *Phys. Rev. B*, 2008. doi:10.1103/PhysRevB.78.064427.
- [36] I. Krug et al. Magnetic coupling in highly ordered NiO/Fe₃O₄(110): Ultrasharp magnetic interfaces vs. long-range magnetoelastic interactions. *EPL*, 2008. doi:10.1209/0295-5075/81/17005.
- [37] M. W. Haverkort et al. Symmetry analysis of magneto-optical effects: The case of x-ray diffraction and x-ray absorption at the transition metal L_{2,3} edge. *Phys. Rev. B*, 2010. doi:10.1103/PhysRevB.82.094403.

Part II

Experimental results

4 Nickel ferrite - NiFe_2O_4

The results presented in this chapter are published in:

- A. Mandziak, J. de la Figuera, S. Ruiz-Gómez G. D. Soria, L. Pérez, P. Prieto, A. Quesada, M. Foerster, L. Aballe, *Structure and magnetism of ultrathin nickel-iron oxides grown on Ru(0001) by high-temperature oxygen-assisted molecular beam epitaxy*, Scientific Reports (2018) 8:17980

4.1 Introduction

Magnetic oxides with the spinel structure[1], such as ferrites, are versatile, low-cost materials with a high electromagnetic performance over a wide frequency range[2; 3]. When two different metal cations are incorporated into the spinel structure, the possibility of changing the stoichiometry and the cation distribution allows to tune the electronic and magnetic properties over a large range. In particular, nickel ferrite, NiFe₂O₄ (NFO) has attracted interest due to a high Curie temperature of 850 K, good insulating behaviour with a band gap of ~ 1.5 eV[4] and a large exchange splitting. Additionally, soft magnetic behaviour of NFO, high electrical resistivity or high thermal and chemical stability make it interesting for technological applications such as high frequency magnetostatic devices, microwave applications e.g. circulators and phase shifters, magnetic recording devices or spintronics. However, in order to integrate ferrites into electronic or spintronic devices, it is needed to fabricate thin films of these materials. And often thin films show novel magnetic properties compared to the bulk material, which can considerably influence their performance. In the case of NFO, there are reports of increased magnetic moments in the ultrathin limit[5; 6].

It was already shown that by changing the conditions of the preparation method[7] we can tune its properties, even to the point of ordering the Ni cations within the octahedral sites[8; 9] (the Ni cations have a strong preference towards the octahedral sites, i.e., NFO is an inverse spinel). In addition, it has been directly observed that NFO thin films are affected by growth defects - antiphase boundaries resulting in disappointing properties in comparison with its bulk counterpart[10; 11].

4.1.1 Crystal structure

In its bulk structure nickel ferrite adopts an inverse spinel structure (Figure 4.1). The spinel structure is based on face-centered cubic (fcc) unit cell of O²⁻ anions with a general formula AB₂O₄ where A and B are divalent (A²⁺) and trivalent (B³⁺) cations, respectively. In the normal spinel structure, the A²⁺ cations occupy 1/8 of the fcc tetrahedral sites (T_d) while the B³⁺ occupy 16 of the 32 octahedral sites (O_h).

In the inverse spinel structure the B³⁺ cations are equally distributed between tetrahedral and octahedral site, while A²⁺ cations occupy half of the octahedral sites. The general formula can be written as [B]_{T_d}[AB]_{O_h}O₄.

Thus, within the NiFe₂O₄ crystal structure the Ni²⁺ cations are located at octahedral sites while the Fe³⁺ cations are equally distributed between octahedral and tetrahedral sites of the O²⁻ fcc cell. The corresponding formula can be written as:



Due to the variation of cation concentration non-stoichiometric nickel ferrite is also possible. In the case of Ni:Fe<1:2, some octahedral sites are occupied by additional Fe^{2+} cations.

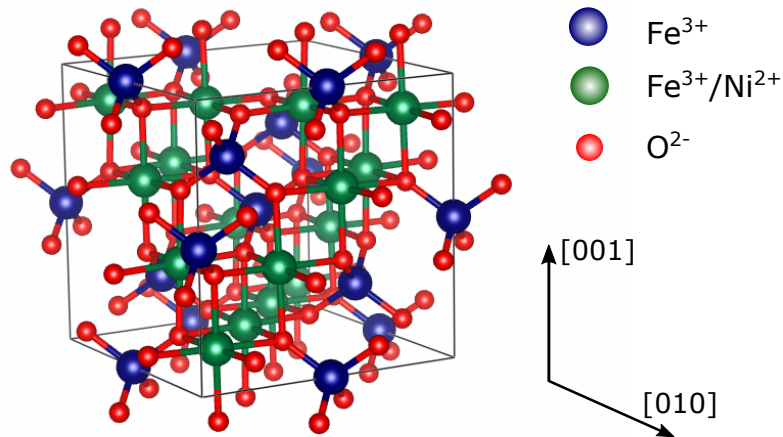


Figure 4.1: Schematic illustration of nickel ferrite crystal structure

4.1.2 Magnetism properties of nickel ferrite

Magnetic interactions

In its bulk form nickel ferrite shows ferrimagnetic order up to 850 K. The magnetic structure consists of two antiferromagnetically coupled sublattices, in each of which the coupling is ferromagnetic. This arrangement arises from several different interactions. In the following we will discuss them, starting from those particularly important in transition metal oxides.

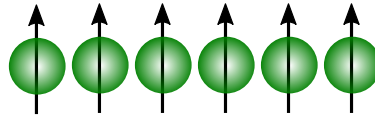
1. Exchange interaction - short range (few Å), strong interaction (0.1-50 eV) originate from electrostatic interaction between neighbouring atoms. Although it is not magnetic interaction it gives rise to coupling between spins (magnetic moments). The cost of exchange interaction can be described by the following formula:

$$E = -2J_{ij}S_i \cdot S_j \quad (4.2)$$

where J_{ij} is the exchange integral and S_i and S_j are the spin angular momentum. Depending on the sign of J_{ij} the ordering of magnetic moments can be:

- $J > 0$ ferromagnetic (Figure 4.2a);
- $J < 0$ antiferromagnetic (Figure 4.2b).

(a) $J > 0$ ferromagnetism



(b) $J < 0$ antiferromagnetism

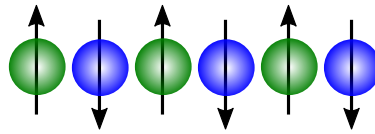


Figure 4.2: Schematic illustration of ferro and antiferromagnetic order.

2. Superexchange interaction - it appears in materials where the magnetic cations (usually $3d$ metals) are separated by non-magnetic anions[12]. The cations cannot be coupled via direct exchange interaction because the distance between them is too large. Thus, the interaction involves an intermediate anion. In the case of nickel ferrite Ni^{2+} and Fe^{3+} cations are coupled via the overlapping of their $3d$ orbitals with the $2p$ orbital of oxygen (Figure 4.3a). This leads to antiferromagnetic coupling between neighbouring cations when the overlap angle¹ α is 180° . While for $\alpha = 90^\circ$ the interaction is ferromagnetic and is much weaker (Figure 4.3b). For NiFe_2O_4 it was found both experimentally and theoretically that the superexchange interaction between Ni and Fe ions located in tetrahedral (A) and octahedral (B) sites is antiferromagnetic (AF) with an interaction energy $J_{A-B} = -27.4 k_b$ (where k_b is Boltzman constant). There is also AF coupling between ions at A sites ($J_{A-A} = -15 k_b$) and ferromagnetic interaction between ions at B sites ($J_{B-B} = 29 k_b$)[13; 14].

¹The magnetic ion-ligand-magnetic ion angle.

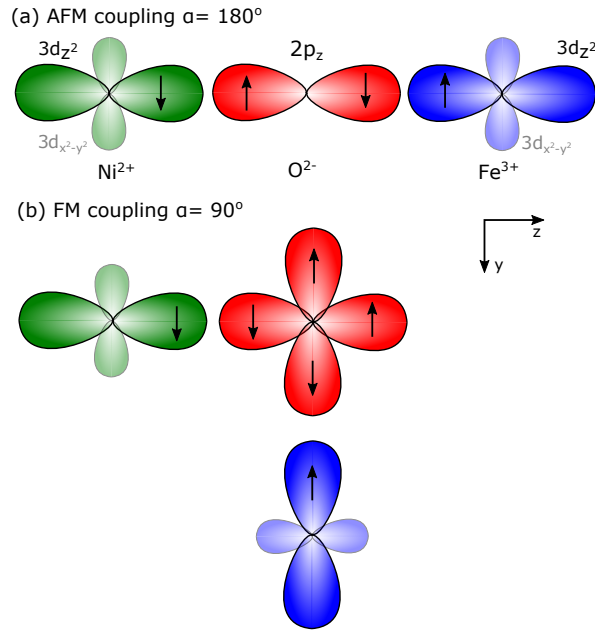


Figure 4.3: Schematic illustration of (a) antiferromagnetic and (b) ferromagnetic superexchange interaction in oxides.

3. Double-exchange interaction - referred as cation-cation interaction, similar to superexchange. It can occur between neighbouring cations with different valence. For NiFe_2O_3 the extra electron from Ni^{2+} (d^8) is transferred through oxygen to an empty d -state in Fe^{3+} (d^5) via a two step process: the transfer of an electron from O to Fe followed by transfer of electron from a vacated oxygen orbital. This interaction results in ferromagnetic alignment of cations located in octahedral sites (Ni^{2+} and Fe^{3+})[12]. The contribution to the total energy of the system of double-exchange interaction is then:

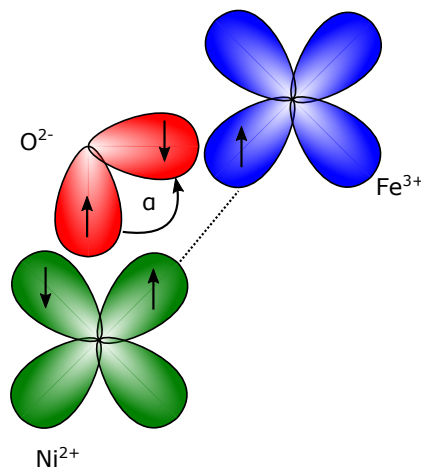


Figure 4.4: Schematic illustration of ferromagnetic double exchange interaction in nickel ferrite.

$$E = -t(\alpha)\cos(\alpha/2) \quad (4.3)$$

where $t(\alpha)$ is the hopping probability and α the overlapping angle.

Magnetic domains

In magnetic materials (ferri- or ferromagnetic), strong short range exchange interaction forces all moments into a ferromagnetic alignment. However, much more weaker long range interactions such as dipole-dipole interaction tends to destroy the ferromagnetic order. To minimize the internal energy of magnetic materials, they spontaneously divide into separate regions (domains) within each the magnetization is pointing in the same direction. In order to fully understand the magnetic domains in nickel ferrite films, one has to take into account different energy contributions. In the following we will introduce the most relevant ones[15–17].

1. Magnetostatic energy - the energy related to the magnetic field generated by the sample itself. It takes the value

$$-\frac{\mu_0}{2} \int_V M \cdot H_d dV \quad (4.4)$$

where the integral is taken over the whole volume of the sample. Term H_d is given by

$$H_d = \frac{1}{\mu}(B - M) \quad (4.5)$$

and the field outside the magnetic material $H_S = \frac{1}{\mu}B$. (The magnetic fields inside a magnetic material is called the demagnetization field, while that outside the magnetic material the stray field). The magnetostatic energy depends on the shape of the sample and is normally not homogeneous over the whole volume. For thin films the magnitude of H_d is nearly zero for in-plane magnetization, otherwise (for out-of-plane magnetization) the demagnetization field has a maximum value: $H_d = -\frac{M}{\mu_0}$. Therefore, shape can be the source of another type of magnetic anisotropy called shape anisotropy.

The magnetostatic energy can be decreased by breaking the sample into domains. However each domain produces additional energy cost because of domain wall formation. Thus, the final size of the domain is the balance between the exchange and the shape anisotropy energies.

2. Magnetocrystalline anisotropy energy - is responsible for the fact that it is easier to magnetise a material along some crystalline directions than along others (so-called easy and hard axis, respectively). It arises from the spin-orbit interaction (coupling between the orbital motion of electron with crystal electric field) and is much weaker than the exchange interaction. The magnetocrystalline anisotropy depends on the crystallographic structure of a given

material and e.g for nickel ferrite, a cubic system, can be expressed by the following formula:

$$E = K_1(m_x^2m_y^2 + m_y^2m_z^2 + m_x^2m_z^2) \quad (4.6)$$

where K_1 is first order cubic anisotropy constant and $m = (m_x, m_y, m_z) = M/|M|$. Note that if $K_1 > 0$ the easy axis points along $\langle 100 \rangle$ direction. If otherwise $K_1 < 0$ it points along $\langle 111 \rangle$. Usually higher order terms of magnetocrystalline anisotropy energy:

$$E = K_2m_x^2m_y^2m_z^2 \quad (4.7)$$

are $K_2 \ll K_1$, but sometimes they play a role and must be taken into account. It has been found experimentally that the magnetocrystalline anisotropy constant for nickel ferrite at room temperature has a negative value resulting in $\langle 111 \rangle$ easy-axis[18; 19]. The evolution of anisotropy constants K_1 and K_2 with the temperature is shown in Figure 4.5.

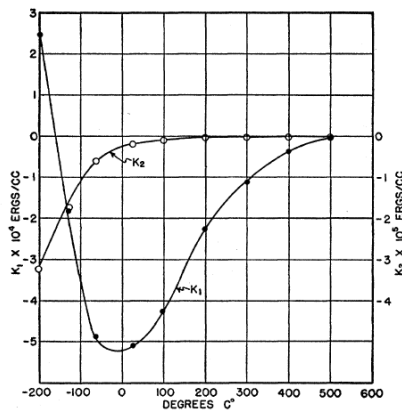


Figure 4.5: Temperature dependence of magnetocrystalline anisotropy constants K_1 and K_2 in bulk NiFe_2O_3 . Reprinted from [18].

The values of K_1 and K_2 at room temperature will be considered further in this chapter in order to explain the magnetic domains in thin nickel ferrite films.

3. Magnetostrictive energy - it links the magnetic and elastic behaviour of magnetic materials. It depends on the crystal structure of the material and for a cubic crystal is defined as:

$$E = B_1(\eta_1m_x^2 + \eta_2m_y^2 + \eta_3m_z^2) + B_2(\eta_1m_x^2m_y^2 + \eta_2m_y^2m_z^2 + \eta_3m_x^2m_z^2) \quad (4.8)$$

where η_i are strain components and B_1 and B_2 magnetoelastic coupling constants related to magnetostrictive deformations λ_{100} and λ_{111} via the following equations:

$$B_1 = -\frac{3}{2}\lambda_{100}(c_{11} - c_{12}) \quad B_2 = -3\lambda_{111}c_{44} \quad (4.9)$$

c_{11}, c_{12}, c_{44} are the elastic moduli. The values of λ_{100} and λ_{111} represent the fractional change in length $\lambda = \frac{\delta l}{l}$ and they are called saturation magnetostrictions.

The magnetostriction constants λ_{100} and λ_{111} for nickel ferrite have been measured over a wide range of temperatures using the ferromagnetic resonance technique. The results presented in Figure 4.6 show that these parameters are constant in a broad range of temperature[20; 21].

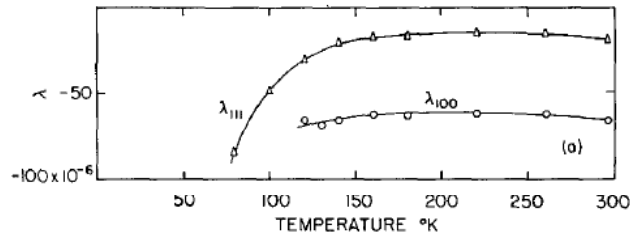


Figure 4.6: Saturation magnetostriction as a function of temperature measured in single crystal of NiFe_2O_3 . Reprinted from [20]

4.2 Growth of nickel ferrite films by high temperature oxygen-assisted MBE

NFO thin films have been previously reported by several groups[5–7; 9; 11; 22–26]. However, films grown by molecular beam epitaxy (MBE) or grown on metal substrates are scarce[27]. As will be shown, growth at a slow rate on a substrate at high temperature can lead to a very low nucleation density and a high crystalline quality of the mixed oxides.

Growth is observed in real time and real space by means of LEEM. The Ni-Fe oxide thin films are deposited onto a (0001)-oriented Ru single crystal while exposing it to molecular oxygen (1×10^{-6} mbar) at high temperature (1150 K). The Ni and Fe dosing rates were 1:2 with the goal of obtaining stoichiometric nickel ferrite (NiFe_2O_4) at rates of the order of 10^{-3} ML/s where 1 ML is defined as $1.4 \cdot 10^{19}$ atoms/ m^2 [28; 29]).

The initial step is to expose the bare Ru substrate to molecular oxygen. Oxygen adsorption is dissociative above room temperature, and forms, at high temperature, a disordered 2-dimensional atomic oxygen gas. The LEED patterns in Figure 4.7 present the temperature dependence of the oxygen phases on Ru(0001). It can be noticed that 2×2 reconstruction starts to appear around 500 K. It has been found that the 2×2 oxygen ordered phase is stable at coverages near $\Theta = 0.25$ ML and low substrate temperatures ($T < 500$ K). The latter is preserved up to $\Theta = 0.6$ ML. At higher coverages the strong repulsive interaction between neighbouring oxygen atoms causes an increased disorder[30].

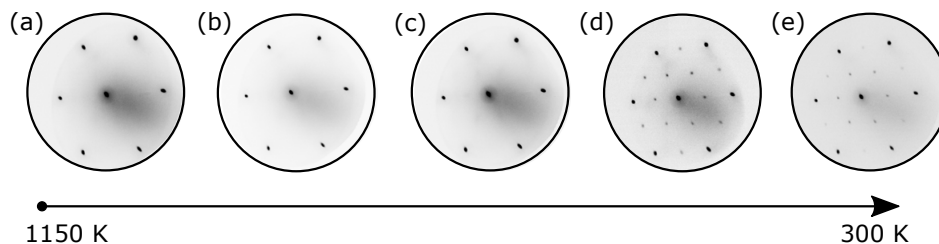


Figure 4.7: LEED pattern of the O/Ru(0001) phases at different substrate temperatures (a) 1150 K, (b) 800 K, (c) 560 K, (d) 480 K, (e) 300 K.

A LEEM image of the substrate with oxygen adsorbed on it just after opening the Fe and Ni dosers is shown in Figure 4.8a. In addition to the uniform decrease of reflected electron intensity due to the adsorbed gas[31], many small nuclei of the iron-nickel oxide decorate the substrate steps (curved lines). As shown in Figure 4.8b–d, with further deposition islands grow until they coalesce, forming a continuous layer covering the substrate, which we call the wetting layer in the following. Continuing the deposition, large islands grow on top of the wetting layer, albeit at a much

slower rate, suggesting they grow 3-dimensionally. Thus the NFO growth seems to be similar to the high temperature growth of both iron oxides[32] and cobalt-iron oxides[33; 34]: a flat wetting layer is followed by 3D triangular islands.

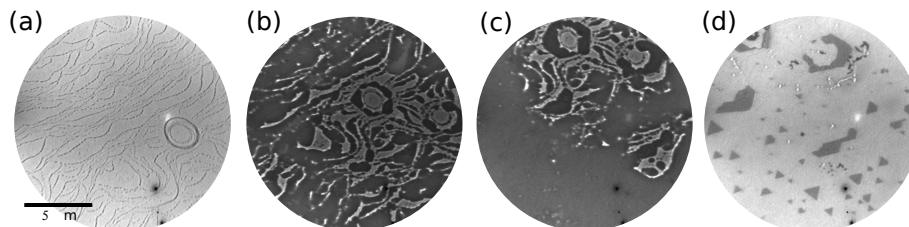


Figure 4.8: Frames selected from a sequence of images acquired during the growth of NFO at 1150 K at a background pressure of $1 \cdot 10^{-6}$ mbar of molecular oxygen. The frames corresponds to (a) 12 sec, (b) 12 min, (c) 27 min and (d) 49 min after the start of the growth at the rate described in the Methods. The electron energy is 19 V.

A microspot low-energy electron diffraction pattern (microLEED) from the wetting layer is shown in Figure 4.9b. The pattern corresponds to an hexagonal unit cell with a lattice spacing of 0.31 nm forming a moiré pattern with a periodicity of 2.0 nm (Figure 4.9e). The pattern is similar to the one observed for FeO upon iron growth in the same conditions[32; 35], with minor differences in the spacings involved. We thus assign it to a similar structure, $\text{Fe}_x\text{Ni}_{1-x}\text{O}$. Like in FeO/Ru[35] the observed pattern is likely to arise from the multiple scattering on the wetting layer due to the formation of a coincidence lattice with the Ru substrate. The lack of additional diffracted spots indicate that there is no further ordering of Fe and Ni, i.e. they form a solid solution. This is unexpected, as the bulk phase diagram indicates a limited solubility of Ni in FeO[36]. From the amount of material deposited at the time needed to close the wetting layer together with the LEED lattice spacing, the wetting layer should correspond to a bilayer of $\text{Fe}_x\text{Ni}_{1-x}\text{O}$. This is corroborated by the LEEM IV spectra of the wetting layer, i.e. the electron reflectivity at very low energy for the specular beam[37], shown in Figure 4.9d. It is very similar to the one corresponding to a bilayer of FeO, and very different from the single FeO layer one[35; 38].

The microLEED pattern from the islands shows a 2×2 structure (Figure 4.9c), marked in the figure with circles, together with very closely spaced satellite spots around each main beam². The distance of the main spots is slightly reduced, corresponding to a spacing of 0.30 nm, while the satellite spots correspond to a 5.6 nm periodicity (Figure 4.9f). The 2×2 pattern is characteristic of the spinel phase, that along the $\langle 111 \rangle$ direction has a unit cell twice as large as the rocksalt one due to the distribution of iron cations on the (111) planes in the former phase[39]. The 0.30 nm distance in turn corresponds to the oxygen-oxygen distance[32]. The

²The spinel spots can in fact also be weakly detected in Fig. 4.9b due to the presence of small islands in the area where the microLEED was acquired.

satellite spots are characteristic of the so-called “biphase” surface reconstruction of iron oxides[40], which was reported also observed on magnetite[38; 41] and cobalt ferrite[33] on Ru(0001). By knowing the angle between the LEED patterns and the real space images, we find that the edges of the spinel islands are oriented along the $[1\bar{1}0]$ direction (which corresponds to $[11\bar{2}0]$ Ru direction). The LEEM IV for an island is also shown for comparison in Figure 4.9d.

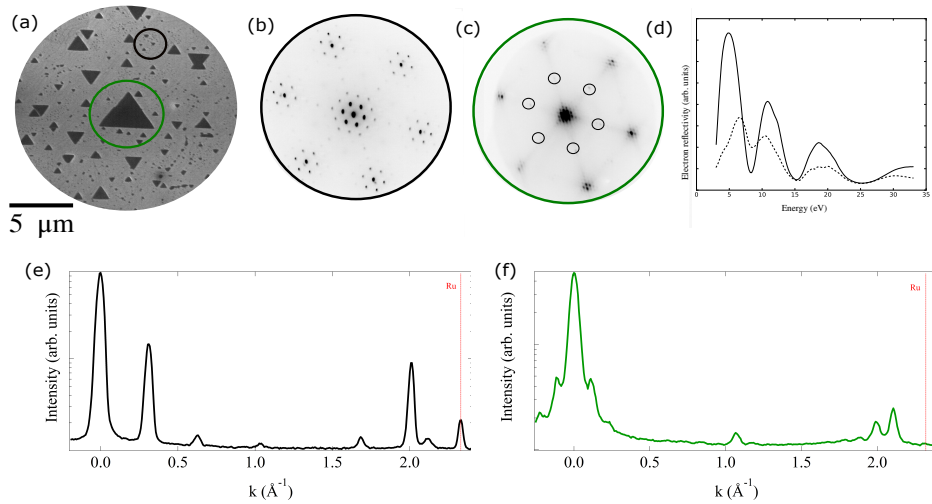


Figure 4.9: LEEM image (a) and corresponding LEED patterns at 35 eV from different regions of the sample: (b) wetting layer, (c) large triangular island, where some of the 2×2 beams are marked with circles. (d) LEEM IV spectra (electron reflectivity of the specular beam) from the wetting layer (continuous line) and an island (dashed line). Cross sectional cuts along the moiré pattern at the (e) wetting layer (black) and (f) island (green), compared to ruthenium (red dashed line).

The similarity to the growth of both magnetite[38] or cobalt ferrite[33] on Ru(0001) should not hide the fact that this is an unexpected result considering the bulk phase diagram of Fe-Ni-O[36; 42]: with less than 80% Ni a NiFe alloy should be found in coexistence with FeO with minute amounts of dissolved Ni, while with a larger Ni ratio, the alloy should be in coexistence with Ni-Fe spinels (Figure 4.10). Our observations highlight the influence of the substrate, as already discussed for iron oxides[43]. One open question linked to the substrate influence is whether the spinel islands rest directly on the Ru substrate, or whether they lie on the rocksalt oxide wetting layer. We have no proof either way, specially as unlike in ultrathin magnetite[38], the oxygen lattice in-plane spacing in the wetting layer and the spinel islands differ.

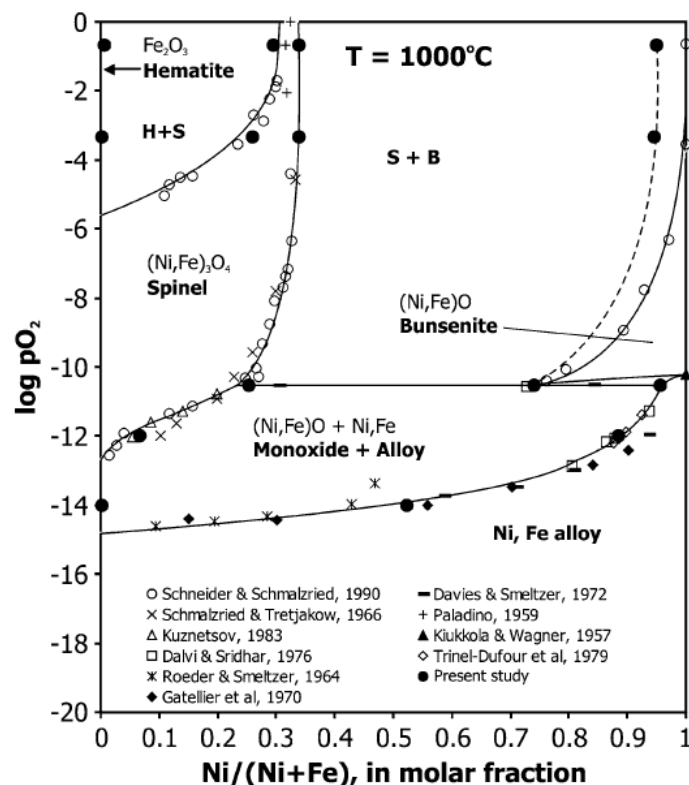


Figure 4.10: Isothermal phase diagram of Fe-Ni-O (logarithm of oxygen partial pressure versus molar fraction of Ni) at 1000°. Reprinted from [44].

4.3 Chemical and magnetic properties

The chemical and magnetic properties of our films were investigated by means of XAS and XMCD spectra acquired at the Fe and Ni L edges. A XAS-PEEM image at the L_3 iron edge is shown on the Figure 4.11a. Several islands are shown, some of them touching by the edge. The trapezoidal island in the middle shows a shadow on the side of an island opposite to the x-ray beam incidence so its height can be determined: typical heights are tens of nanometers or less (e.g. the island shown in figure 4.11c-d is 40 nm thick). We note this implies that, unlike the moiré pattern observed on the wetting layer, the bi-phase structure observed on the surface of the islands is a true surface reconstruction and unrelated to the Ru substrate. The islands appear brighter in Fe L_3 images than the wetting layer, suggesting that they contain more iron. A similar XAS-PEEM image acquired at the Ni L_3 edge is shown in Figure 4.11b. The same features are seen, although the contrast is reversed relative to the wetting layer and much weaker. This suggests that while the islands are clearly richer in Fe than the wetting layer, that is not the case for Ni. To detect the magnetic domains, XMCD-PEEM[45] images are acquired, subtracting XAS

images acquired with opposite light helicities, at an energy close to the maximum of the Fe or Ni L_3 absorption edge. The islands are shown in image 4.11c-d, for Fe and Ni respectively. Only the islands show black and white regions, corresponding to areas where there is a component of the magnetization along or opposite the x-ray direction. Thus only the islands present magnetic domains. The domain structures associated to iron and nickel match perfectly, although the Ni one is noisier. The black ribbon that corresponds to the shadow in the XAS image presents a reversed magnetic contrast in the XMCD images. This effect is due to x-rays transmitted through the island that reach the wetting layer. But being an XMCD transmission pattern instead of an emission one, their contrast is reversed relative to the latter [46]. They show the same pattern as the edge, indicating that the domains extend through the thickness of the island.

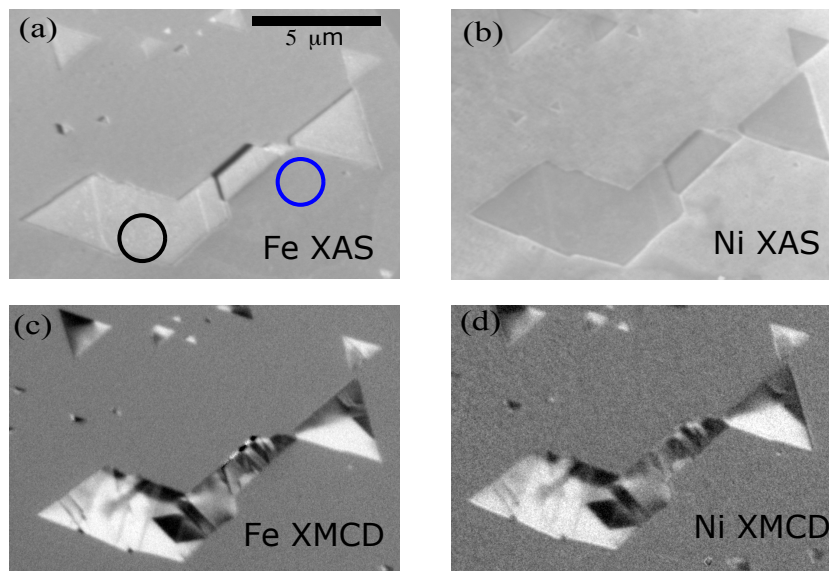


Figure 4.11: a) Fe and (b) Ni XAS-PEEM images acquired at the respective L_3 edges, normalized by the same images acquired at pre-peak energies. (c) Fe and (d) Ni XMCD-PEEM images acquired in the same location.

From the stack of PEEM images collected at different photon energies, we have extracted the XAS spectra at Fe and Ni L-edges for the wetting layer and islands, respectively. The spectra of wetting layer are presented in Figures 4.12 and 4.13

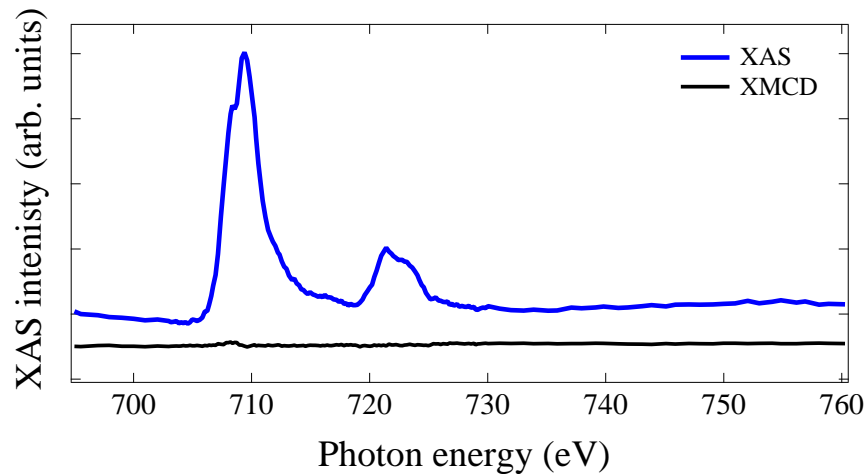


Figure 4.12: XAS and XMCD spectra Fe-edge from the wetting layer (the region indicated by a blue circle in Figure 4.11a)

Information of the cation oxidation state and site can also be obtained from the spectra. The XMCD spectra for both Ni and Fe do not show any magnetic contrast (black curve). It is reflected on the XMCD-PEEM images where the wetting layer has a gray color, corresponding to no magnetic contrast (Figure 4.11c–d). The spectra of the wetting layer (Figure 4.13) and island (Figure 4.15) are similar to the ones of nickel oxide[47] and of nickel ferrite grown by sputtering[24], where nickel occupies octahedral sites with an oxidation state of +2 (Ni_{oct}^{2+}). The L_2 edge shows a characteristic double peak structure. The Fe spectrum corresponding to the wetting layer is more difficult to interpret, although it is similar to spectra measured in ultrathin FeO[48] and mixed Co-Fe oxide[49].

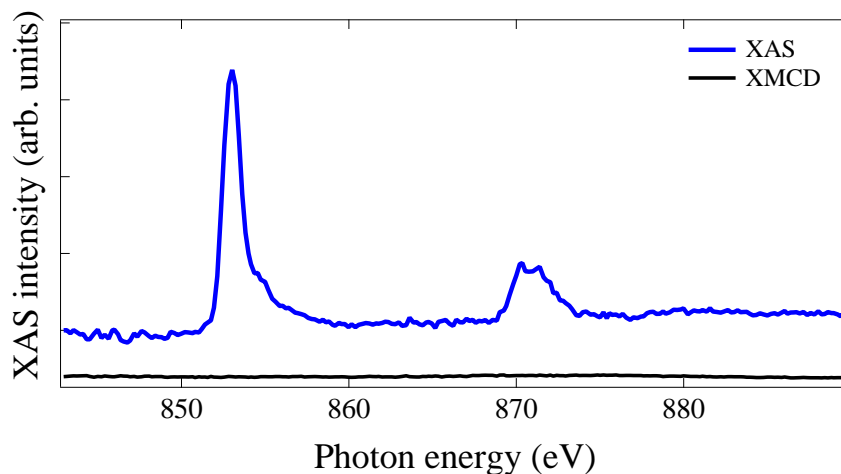


Figure 4.13: XAS and XMCD spectra Ni-edge from the wetting layer (the region indicated by blue circle in Figure 4.11a)

The situation is quite different for the islands. From stack of images acquired with opposite light helicities (Figure 4.15 4.14), integrated from a single domain area the

spectra are obtained. The Fe L_3 edge XAS spectrum from the island (black circle in Figure 4.11d) is somewhat similar to that of Fe_3O_4 [50; 51]. The nickel XMCD spectrum has a single valley, which corresponds to a single contribution, as expected for Ni_{oct}^{2+} [52]. For iron it presents a three peak structure at the L_3 edge similar to the one from magnetite[50; 51]: first a valley attributed usually to a contribution of Fe_{oct}^{2+} , next a peak which arises mostly from Fe_{tet}^{3+} and finally a valley assigned to Fe_{oct}^{3+} . Thus octahedral positions are occupied by both Ni^{2+} , Fe^{2+} and Fe^{3+} , while the tetrahedral positions are populated only by Fe^{3+} . Furthermore, from the Ni XMCD spectra it is clear that the Ni cations have the same magnetization direction as the octahedral Fe^{2+} and Fe^{3+} cations, i.e. they are coupled ferromagnetically. The energies at which the XMCD images shown in Figure 4.11c and d were taken correspond to the main peak for the Ni XMCD spectrum and the first minimum of the Fe XMCD spectrum (which corresponds mostly to Fe_{oct}^{2+}).

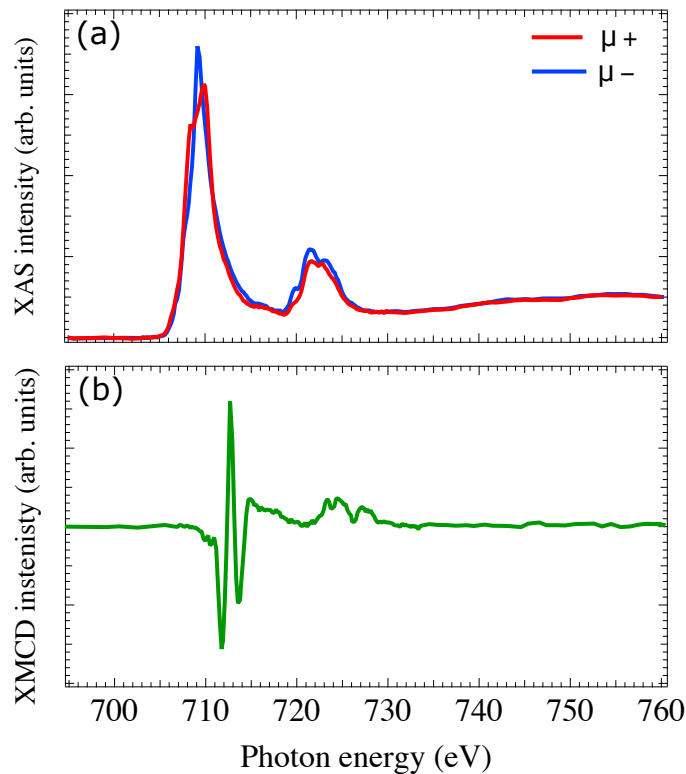


Figure 4.14: XAS and XMCD spectra measured at Fe-edge from the island (the region indicated by black circle in Figure 4.11a)

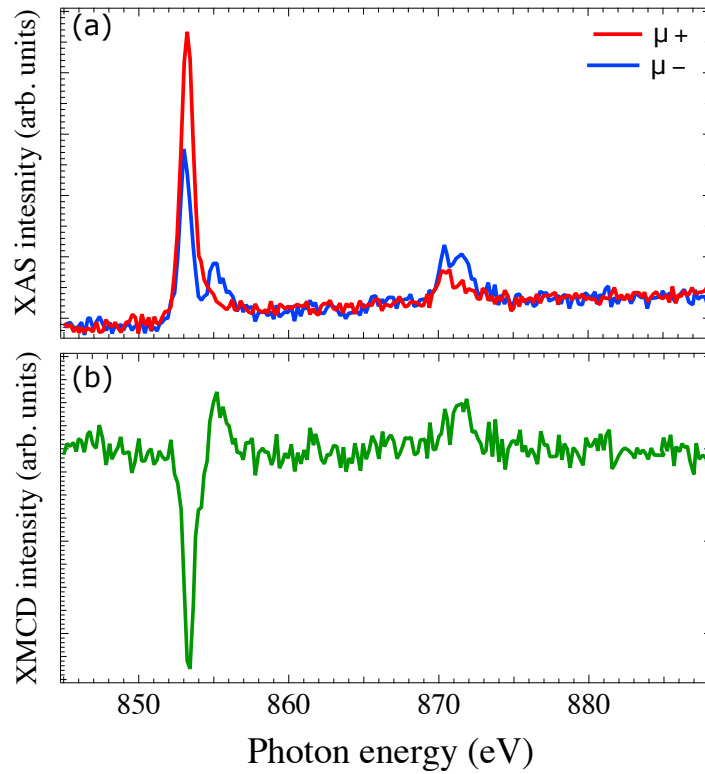


Figure 4.15: XAS and XMCD spectra measured at Ni-edge from the island (the region indicated by black circle in Figure 4.11a)

Element	μ_x [nm^{-1}] 10 eV below L_3	μ_x [nm^{-1}] at L_3 peak	μ_x [nm^{-1}] 40 eV above L_3
Fe	1.8×10^{-3}	6.0×10^{-2}	1.2×10^{-2}
Ni	1.6×10^{-3}	4.6×10^{-2}	1.2×10^{-2}
Co	1.8×10^{-3}	6.4×10^{-2}	1.2×10^{-2}

Table 4.1: Linear absorption coefficients μ_x [nm^{-1}] for Fe, Ni, Co for three energies. Reprinted from [12].

Furthermore, the XAS intensity is proportional to the number of absorbing atoms in the sample. As a consequence, the edge jump, defined as the difference of the intensities above and below an absorption edge, is proportional to the number of absorbing atoms and linear absorption coefficient (μ_x). Thus the intensity ratio at the minimum between L_3 and L_2 edges can be used to provide an estimate of the composition of the area under observation[12]. We find that while the wetting layer has a Fe:Ni ratio of 1:1, on the islands it is closer to 5:1, corroborating that the islands are richer in iron than the wetting layer. The composition is preserved regardless of the thickness of islands and of the position within the island. Taking together the LEED and the XAS/XMCD information, we suggest that the wetting layer is composed of Fe_{0.5}Ni_{0.5}O forming a moiré pattern, while the islands have a

composition close to $\text{Ni}_{0.5}\text{Fe}_{2.5}\text{O}_4$ and present a bi-phase reconstruction. This implies that there is a significant population of Fe^{2+} , as expected from the presence of excess iron relative to the canonical NiFe_2O_4 spinel

One striking observation is that neither the composition of the wetting layer nor of the islands correspond to the deposited ratio of Fe:Ni of 2:1; from the XAS spectra we estimate an iron/nickel ratio of 5:1 in the islands and close to 1:1 in the wetting layer. Only when we consider the total amount of deposited material (islands plus wetting layer) it is in reasonable agreement with the deposited ratio. These observations of iron-enriched spinel are in line with reports on the oxidation of NiFe alloys, that also produce iron-rich spinel phases[53; 54]. We made attempts to increase the Ni ratio in the spinel islands by changing the dosing ratio to Fe:Ni 1:2, but instead of obtaining islands with a higher amount of Ni, the nucleation of 3-dimensional Fe-doped nickel oxide islands was observed (which is in line with the bulk phase diagram[36; 42]). Growth at lower temperatures (800 K - 900 K), on the other hand, resulted in segregation into magnetite and metallic Ni. Our results underscore the difficulties to predict the details of the growth of oxides in the ultrathin regime, where the combination of substrate effects, kinetic limitations and thermodynamic factors can give rise to unexpected phases or compositions.

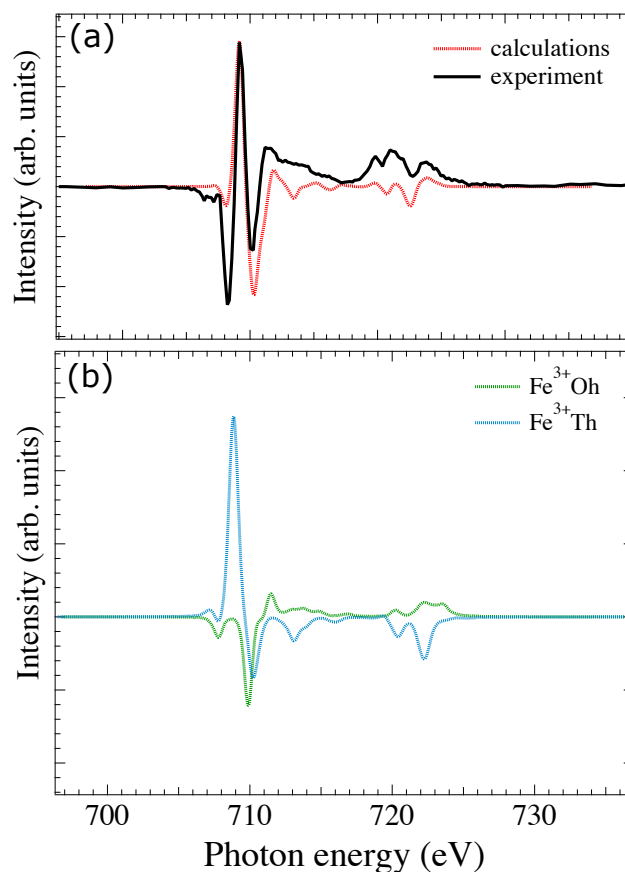


Figure 4.16: (a) Experimental XMCD spectrum from Fe $L_{2,3}$ edge of the $\text{Ni}_{0.5}\text{Fe}_{2.5}\text{O}_4$ films on Ru(001) and the corresponding fit. (b) Calculated Fe cations contribution to the XMCD spectrum of a nickel ferrite.

In order to identify any changes in distribution of Fe and Ni cations between T_d and O_h sites for NiFe_2O_3 we have performed ligand field multiplet calculations utilizing the software Crispy. Site and valency specific XMCD spectra for both Fe and Ni $L_{2,3}$ edge are presented in Figure 4.16 and 4.17.

It can be noticed in Figure 4.16 that the first experimental peak is much larger than in the calculated spectrum, indicating the presence of some of Fe^{2+} cations within the NFO films. This agrees with the XAS study, where we have found that the composition of islands is non-stoichiometric and hence it could explain the occurrence of Fe^{2+} cation in octahedral site. The Ni $L_{3,2}$ spectra shown in Figure 4.17 confirm the presence of Ni^{2+} cation in the spinel islands.

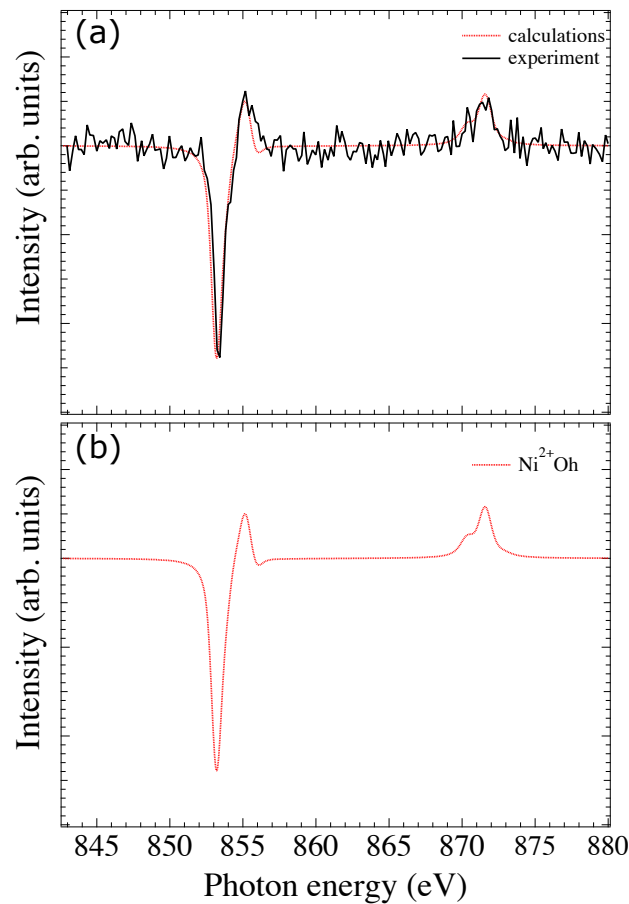


Figure 4.17: (a) Experimental XMCD spectrum from Ni $L_{2,3}$ edge of the $\text{N}_{0.5}\text{Fe}_{2.5}\text{O}_4$ films on Ru(001) and the corresponding fit. (b) Calculated Ni^{2+} cation contribution to the XMCD spectrum of a nickel ferrite.

Magnetic domain structure

The magnetic domain structure of each island was imaged via XMCD-PEEM. The energies used for XMCD image acquisition correspond to the main peak at the Ni XMCD spectra and the first peak of the Fe XMCD, respectively. The domain

structure present in Figure 4.11c–d is the same for Fe and Ni, a clear indication of ferromagnetic alignment of both cations in an octahedral position. Additionally, the high crystalline quality results in remarkably large domains (up to few μm^2), compared to other NFO films prepared by different methods.

Using XMCD-PEEM images the component of the magnetization along the x-ray incidence direction is measured. In order to determine the full magnetization vector within each domain, at least three different components along non-coplanar directions have to be measured. The XMCD images acquired at three different azimuthal angles 0° , 60° and 120° after distortion corrections and transformations are shown in Figure 4.18 for both Fe and Ni.

Further, by transforming the XMCD images (Figure 4.18) from the skew reference frame to an orthogonal one[55], the spatially resolved vector maps can be obtained. The results obtained for the island shown in Figure 4.18 are presented below.

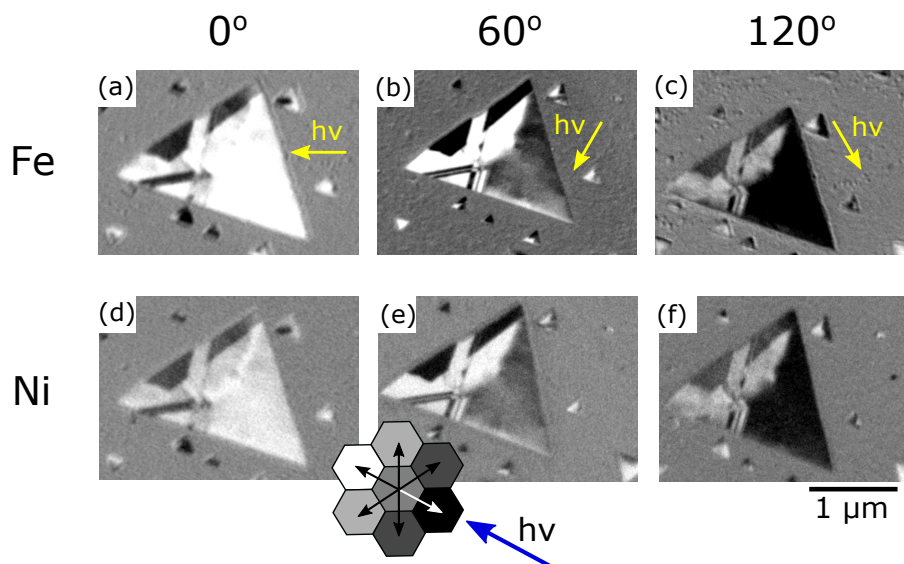


Figure 4.18: XMCD PEEM images acquired at different azimuthal angles at the (a)-(c) Fe and (d)-(f) Ni L edges, respectively.

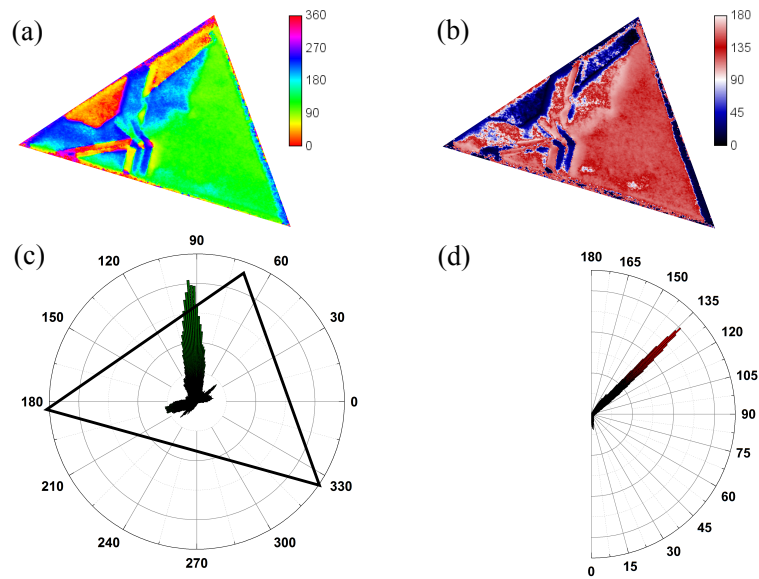


Figure 4.19: Fe image of the (a) in-plane and (b) out-of-plane orientation of the magnetization (with the colour to angle correspondence shown in the color bar located next to it). (c),(d) Distribution of the in-plane and out-of-plane magnetization angles, obtained from the data shown in (a) and (b) respectively.

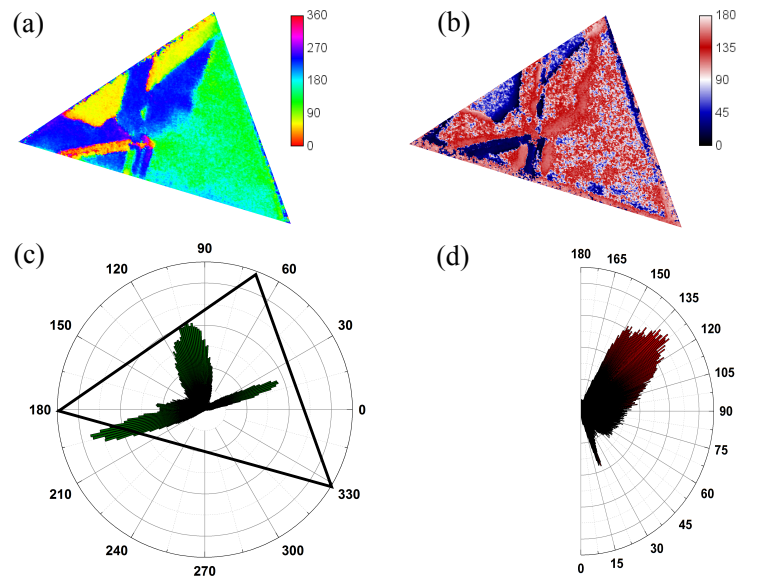


Figure 4.20: Ni image of the (a) in-plane and (b) out-of-plane orientation of the magnetization (with the colour to angle correspondence shown in the color bar located next to it). (c),(d) Distribution of the in-plane and out-of-plane magnetization angles, obtained from the data shown in (a) and (b) respectively.

The orientation of the magnetization in the different domains is shown in Figure 4.19 and 4.20 as obtained from dichroic images at the L_3 edges of both Fe and Ni. Both give similar results, the Ni having a worse signal to noise ratio. There the in-plane and out-of-plane angles are indicated by the color palette shown next to vector maps. The magnetic domain size depends on the particular island, but it is often remarkably large, up to several μm^2 . The island presents a large domain occupying half of its area, and some intricate domains on the left portion. A significant out-of-plane angle for the magnetization is detected throughout the island. The in-plane orientation of the largest (green) domain is not too far off the side of the island, as also happens with the smaller blue and yellow ones on the opposite side. This suggests that the magnetocrystalline anisotropy is overcome by the shape anisotropy, as expected in a soft magnet such as an iron-rich iron-nickel spinel, and as has been recently reported for magnetite islands[55]. However, the magnetization has a well defined out-of-plane component, which is half way from in-plane to out-of-plane (45°). This is quite unexpected, as the shape anisotropy term is expected to drive the magnetization in-plane.

We performed micromagnetic simulations of triangular islands similar in size to the experimental ones using the MuMax3[56] software and the material parameters for bulk NFO[57]. For such case, the in-plane magnetization should point in-plane along the projection of the magnetocrystalline axis, and out of plane with an angle of $\pm 20^\circ$ with the film plane. As our islands are iron rich with a larger magnetic moment, we expect the shape anisotropy to dominate the magnetization directions, driving the in-plane component to be parallel to the triangles edges -as observed-. But the same effect should also drive the magnetization further in plane, in contrast with the experimental observation. In addition, the domain walls are often remarkably sharp, suggesting a strong influence of contributions such as interface and surface anisotropies or quantum size effects. The latter have been observed sometimes in ultrathin magnetite and often in cobalt ferrite islands[33; 38].

It remains to be determined whether the wetting layer mixed FeNi oxide presents antiferromagnetic order and if so, with which Néel temperature. If the wetting layer is magnetically ordered at room temperature, exchange bias effects might play a role in the magnetic properties of the spinel islands, specially if, as discussed before, underlying the spinel layers there is a rocksalt layer.

Spin and orbital magnetic moment

According to the crystal field theory, the magnetic moments of nickel ferrite arise from the local moments of Ni^{2+} and Fe^{3+} cations, both with $3d^8$ configuration. The net magnetization comes from the Ni^{2+} cations in octahedral site ($\sim 2\mu_B$), while the moments of Fe^{3+} cations ($\sim 5\mu_B$ in high spin state) for both sites (tetrahedral and octahedral) are antiparallel and thus cancel each other. This leads to the total magnetic moment per formula unit $\sim 2\mu_B$.

Various methods have been applied to synthesize nickel ferrite films, but only few of them maintain the NFO bulk magnetic properties. In Table 4.2 we have summarized some of the magnetic moments reported in literature.

Sample	μ_{spin} (Ni)	μ_{orb} (Ni)	μ_{spin} (Fe)	μ_{orb} (Fe)	μ_{total}	Ref.
NiFe ₂ O ₄ nanoparticles	-	-	-	-	2.3	[58]
6 nm NiFe ₂ O ₄ /Nb-SrTiO ₃	-	-	-	-	1.3 - 1.5	[6]
2 nm NiFe ₂ O ₄ /Nb-SrTiO ₃	0.78	0.09	0.63	0.09	1.1	[59]
2 nm NiFe ₂ O ₄ /SrTiO ₃	-	-	-	-	8	[5]
NiFe ₂ O ₄ powder	-	-	-	-	1.54	[60]
NiFe ₂ O ₄ theory	1.33	-	3.4	-	2	[61]
NiFe ₂ O ₄ theory	1.57	0.36	4.11	0.11	2	[62]

Table 4.2: Spin and orbital magnetic moment of NiFe₂O₄ reported in the Literature.

The values reprinted in Table 4.2 have been obtained both theoretically and experimentally for NFO in different forms (nanoparticles, powder, films). In most of the cases the value of total magnetic moment is reduced compared to the bulk one. These results were attributed to the increased presence of antiphase boundaries (APBs) which is a common problem in oxides with spinel structure. These defects appear mainly in the structure with reduced thickness (thin films) and they strongly influence the final properties of materials. The formation of APBs appear at the initial stage of the growth process when growth nuclei whose atomic structures are shifted with respect to each other, coalesce. As a result the anion lattice remains unchanged while the cationic lattice is shifted at the interface affecting the magnetic and transport properties of the material, and often resulting in the properties that not exist in the bulk form.

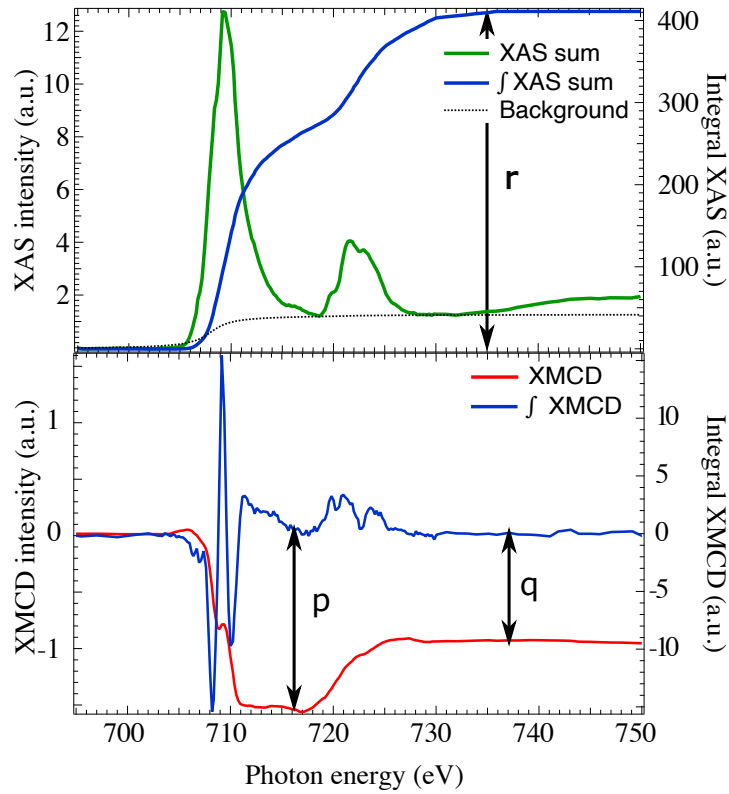


Figure 4.21: a) XAS summed (in green, top) and XMCD (in blue, bottom) spectra at the Fe $L_{2,3}$ absorption edge from a $\text{Ni}_{0.5}\text{Fe}_{2.5}\text{O}_4$ island. The blue line represents an integral of the XAS summed spectrum after background subtraction. The red line corresponds to the integral of the XMCD curve. The dashed black line is a background (two-step function based on arctangent function).

We have determined the spin and orbital magnetic moment of a NFO films, grown by oxygen-assisted high temperature MBE. According to the XMCD sum rules[63] we can estimate the orbital m_{orb} and spin m_{spin} magnetic moments from the XAS and XMCD spectra (Figure 4.14 and 4.15). If the number of holes per unit cell is known for each cation, the individual values of m_{orb} and spin m_{spin} magnetic moments can be obtained as well. In our case the number of holes used for Fe is 4.7 (corresponding to Fe^{3+} [64]). For Ni^{2+} we have used 2, as for Ni^{2+} in several compounds it is within 10% of that value[65]. The orbital moment is obtained directly while an effective spin moment is estimated, which includes the expectation value of the magnetic dipole operator $\langle T_z \rangle$. However, the latter is expected to be small for transition metal compounds at room temperature[66].

Self-absorption effects can also be neglected since we are measuring secondary electrons and the probing depth of about 1 nm[67] is well below the x-ray absorption length even for grazing incidence (10 and 20 nm at L_3 and L_2 edges, respectively). The moments obtained are $m_{orb} = 0.18 \mu_B$ and $m_{spin} = 0.94 \mu_B$ for Fe and $m_{orb} = 0.13 \mu_B$ and $m_{spin} = 1.13 \mu_B$ for Ni per cation, giving a total moment $3.45 \mu_B$.

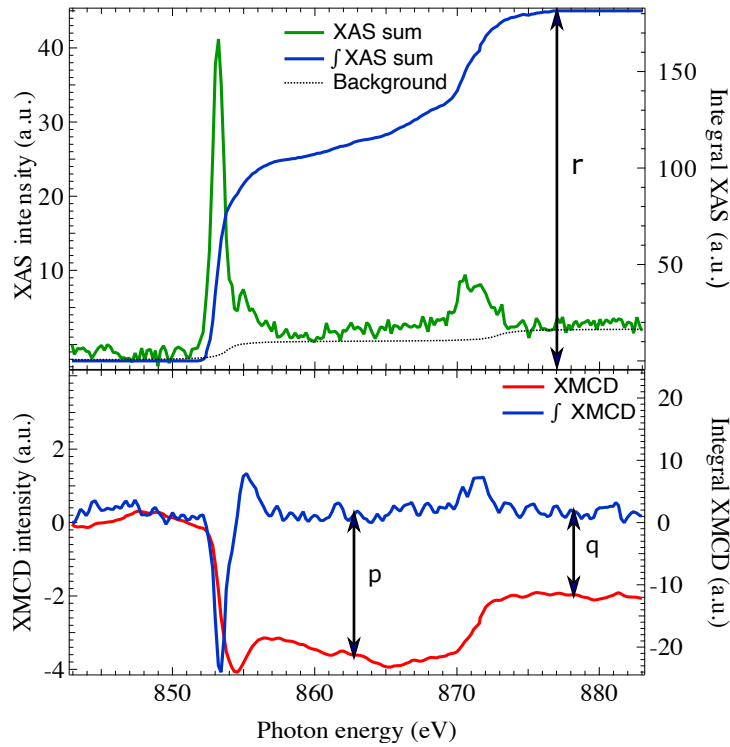


Figure 4.22: (a) XAS summed (in green, top) and XMCD (in blue, bottom) spectra at the Ni $L_{2,3}$ absorption edge from a $\text{Ni}_{0.5}\text{Fe}_{2.5}\text{O}_4$ island. The blue line represents an integral of the XAS summed spectrum after background subtraction. The red line corresponds to the integral of the XMCD curve. The dashed black line is a background (two-step function based on arctangent function).

The total magnetic moment estimated from the sum rules is $3.45 \mu_B$ per formula unit. In stoichiometric NFO the net magnetic moment of $\sim 2 \mu_B$ arises from the Ni^{2+} cations as the octahedral and tetrahedral iron cation contributions cancel each other. The larger total magnetization arises in our case from the extra Fe^{2+} , which has a moment per atom twice as large as Ni^{2+} . In particular, the spin magnetic moments of Fe and Ni were estimated from the sum rules to be 0.94 and $1.13 \mu_B$, respectively. From density functional theory calculations[62] the Fe and Ni spin magnetic moments are typically reduced when compared with the nominal spin counting values. For example, in Ref. [62] the spin magnetic moment for Ni^{2+} in NFO is predicted to be $1.6 \mu_B$ instead of $2 \mu_B$, while the spin magnetic moment of Fe^{2+} (in magnetite) is $3.6 \mu_B$. Considering our stoichiometry, we would thus expect $1.4 \mu_B$ per Fe cation and 1.6 per Ni cation giving a total of $4.3 \mu_B$ per formula unit. Our values are reduced relative to these predictions. However, we note that the small mean free path for electrons[67] means that our experiment probes a very shallow surface region. The local magnetization in such region can be affected by the particular surface termination, as has been shown for magnetite[68]. The observation of the bi-phase termination indicates a reconstructed surface. While the exact character of the bi-phase structure is still under discussion[40], a recent

proposal [69] might imply a reduced magnetization. A definitive conclusion will have to await a detailed atomistic calculations for the bi-phase reconstruction.

XMCD contrast at the O K absorption edge

Finally, we have acquired local O K-edge X-ray absorption spectra from the domains shown in Figure 4.11c–d. The XAS and XMCD spectra are shown below (Figure 4.23). The XMCD signal reveals a small peak at the energy 531 eV, but its origin is not clear. We have mentioned in Chapter 3 that the dichroic effect at the K-edge will occur only if the empty p valence shell posses an orbital moment and its sensitivity to the spin moment (of the p shell) arises indirectly through SO interaction.

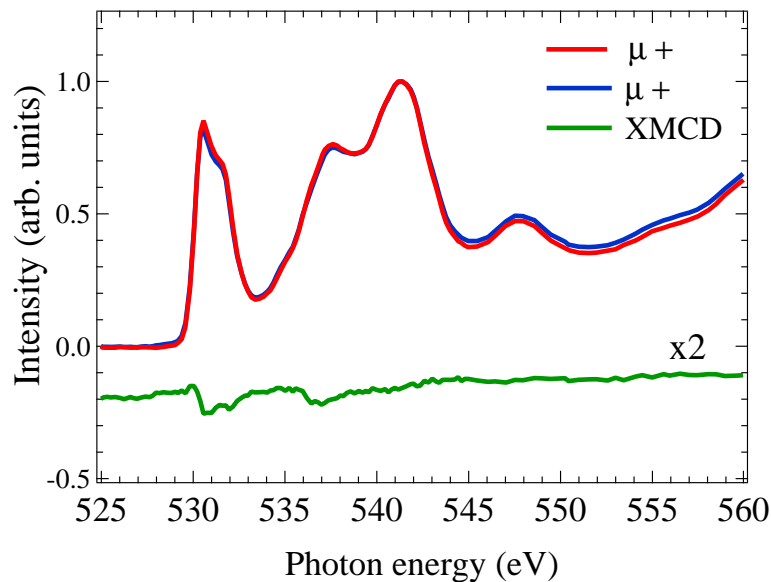


Figure 4.23: XAS and XMCD spectra O K-edge.

To check if there is some magnetic contrast at the oxygen edge, XMCD-PEEM images were acquired. The results are shown in Figure 4.25c together with XMCD Fe and Ni L_3 edge images for comparison. The domains structure associated to Fe, Ni and O match perfectly. However, the contrast observed at O K-edge is much more weaker. It has been found theoretically that small magnetic moment is induced also on the oxygen ($+0.1 \mu_B$), [61; 62] what could explain our XMCD contrast.

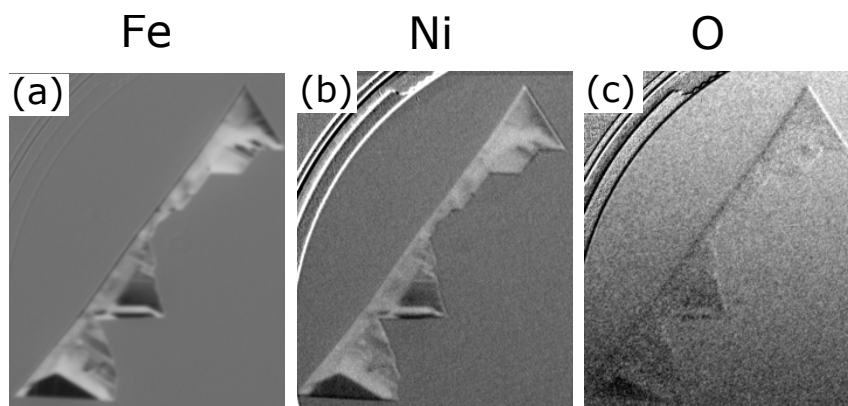


Figure 4.24: XMCD PEEM images acquired at the (a) Fe L_3 , (b) Ni L_3 and (c) O K-edges.

To understand the origin of the oxygen K-edge XMCD intensity in our system, we present DFT calculations performed by Silvia Gallego. It was found that the ground state of NiFe_2O_4 is insulating and of the inverse spinel kind. The octahedral sites are occupied by Ni^{2+} and Fe^{3+} , while the tetrahedral sites are populated exclusively by Fe^{3+} ions. According to the calculation the spin magnetic moment of the Ni ions is $1.57 \mu_B$ and of the Fe^{3+} $4.12 \mu_B$. The oxygen spin moments are aligned parallel to the spin moments of cations in octahedral sites and their value depends on the local environment. The DFT calculations revealed that if the oxygen anions are surrounded by nickel cations the spin moment is $0.05 \mu_B$. Whereas the local environment consists mainly of Fe cations the spin moment of oxygen increases to $0.1 \mu_B$ [70], as illustrated in Figure 4.25. In our case the oxygen anions are surrounded by nickel and iron cations, thus the value should be between 0.05 and $0.1 \mu_B$.

For comparison, the XMCD sum rules at the O K absorption edge have been applied to estimate the orbital magnetic moment [71]. With an arctangent-like edge-jump function for the background of the XAS spectra, the O orbital magnetic moment is therefore estimated to be $(0.03 \pm 0.005) \mu_B$. The value is in good agreement with the one found by DFT calculations. However, it has to be taken into account that the quantitative orbital moment estimation depends strongly on the background function of XAS and electron occupation number in O $2p$ valence band, thus a small uncertainty can occur.

The features observed in light-element K-edge XMCD spectra are attributed to the large orbital localization, hybridization and spin polarization of neighbouring magnetic atoms (Ni, Fe). Because of this O- p states become polarized (spin and orbital) and it leads to the XMCD signal observed at O K-edge.

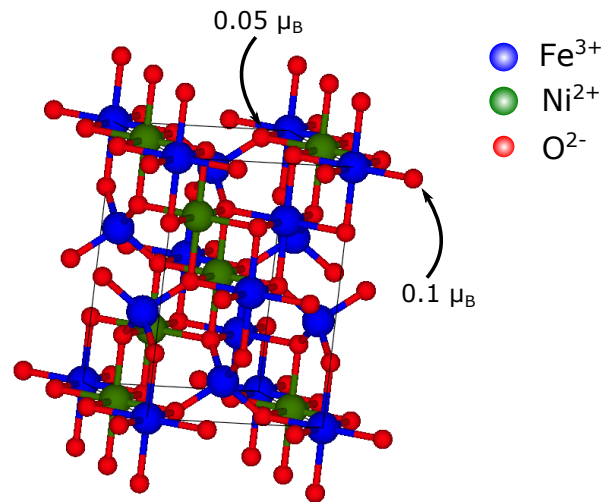


Figure 4.25: Schematic illustration of magnetic moments induced in the oxygen[70].

4.4 Conclusions

Mixed iron-nickel oxides have been grown by oxygen-assisted MBE on Ru(0001) at high temperature. The growth parameters have been optimized by following the growth in real time and real space by means of LEEM in order to obtain large micron-wide triangular islands composed of iron-nickel spinels grown on an iron-nickel rocksalt wetting layer of bilayer height. The wetting layer presents a moiré pattern, while the islands have a bi-phase reconstructed surface. Each island is expected to arise from a single nucleus, leading to a low defect density and explaining the observation of large magnetic domains in remanence. XAS and XMCD spectromicroscopy reveal that the spinel islands are not stoichiometric NiFe₂O₄ but iron rich and that the octahedral positions are occupied by Ni²⁺, Fe²⁺ and Fe³⁺ while the tetrahedral ones are occupied by Fe³⁺.

We estimated the magnetic moment per unit formula, which is larger than for NiFe₂O₄ due to the extra iron, but is likely to be affected by the surface reconstruction. Vector magnetization maps have been obtained from XMCD-PEEM images acquired at three different azimuthal angles. An out-of-plane component, unexpected given the bulk magnetocrystalline anisotropy of an iron-rich nickel ferrite, was detected. Together with the observation of sharp domain walls, this points to a sizeable contribution from so far unidentified magnetic interactions, arising from the reduced thickness, influence of the substrate, and/or kinetic growth factors.

Additionally we have found a sizeable dichroic contrast at the O K-edge. The XMCD images acquired at the same region on the sample at Fe, Ni and O revealed the

same domain configuration. On the basis of DFT calculations we have determined that there is a small magnetic moment induced at the O due to hybridization with neighbouring cations (Ni and Fe). The magnetic moment of oxygen aligns parallel with the Ni and Fe spin moments, what results in the same domain configuration observed at the dichroic images of each element.

4.5 References

- [1] V. A. M. Brabers. Progress in spinel ferrite research. In *Handbook of magnetic materials*, 1995. doi:[10.1016/S1567-2719\(05\)80032-0](https://doi.org/10.1016/S1567-2719(05)80032-0).
- [2] V. G. Harris. Modern Microwave Ferrites. *IEEE Trans. Magn.*, 2012. doi:[10.1109/TMAG.2011.2180732](https://doi.org/10.1109/TMAG.2011.2180732).
- [3] U. Özgür et al. Microwave ferrites, part 1: fundamental properties. *J. Mater. Sci.: Mater. Electron.*, 2009. doi:[10.1007/s10854-009-9923-2](https://doi.org/10.1007/s10854-009-9923-2).
- [4] P. Bougiatioti et al. Electrical transport and optical band gap of NiFe₂O_x thin films. *J. Appl. Phys.*, 2017. doi:[10.1063/1.4999428](https://doi.org/10.1063/1.4999428).
- [5] U. Lüders et al. Enhanced magnetic moment and conductive behavior in NiFe₂O₄ spinel ultrathin films. *Phys. Rev. B*, 2005. doi:[10.1103/PhysRevB.71.134419](https://doi.org/10.1103/PhysRevB.71.134419).
- [6] M. Hoppe et al. Enhanced ferrimagnetism in auxetic NiFe₂O₄ in the crossover to the ultrathin-film limit. *Phys. Rev. B*, 2015. doi:[10.1103/PhysRevB.91.054418](https://doi.org/10.1103/PhysRevB.91.054418).
- [7] U. Lüders et al. NiFe₂O₄: A versatile spinel material brings new opportunities for spintronics. *Adv. Mater.*, 2006. doi:[10.1002/adma.200500972](https://doi.org/10.1002/adma.200500972).
- [8] V. G. Ivanov et al. Short-range B-site ordering in the inverse spinel ferrite NiFe₂O₄. *Phys. Rev. B*, 2010. doi:[10.1103/PhysRevB.82.024104](https://doi.org/10.1103/PhysRevB.82.024104).
- [9] M. N. Iliev et al. Monitoring B-site ordering and strain relaxation in NiFe₂O₄ epitaxial films by polarized Raman spectroscopy. *Phys. Rev. B*, 2011. doi:[10.1103/PhysRevB.83.014108](https://doi.org/10.1103/PhysRevB.83.014108).
- [10] R. Datta et al. Formation of antiphase domains in NiFe₂O₄ thin films deposited on different substrates. *Appl. Phys. Lett.*, 2010. doi:[10.1063/1.3481365](https://doi.org/10.1063/1.3481365).
- [11] R. Datta et al. Structural features of epitaxial NiFe₂O₄ thin films grown on different substrates by direct liquid injection chemical vapor deposition. *J. Cryst. Growth*, 2012. doi:[10.1016/j.jcrysgro.2012.02.007](https://doi.org/10.1016/j.jcrysgro.2012.02.007).

-
- [12] J. Stöhr and H. C. Siegmann. *Magnetism: From Fundamentals to Nanoscale Dynamics*. 2006. doi:10.1007/978-3-540-30283-4.
- [13] M. Ouaiassa et al. Effects of Crystal Fields and Exchange Interactions on Magnetic Properties of Nickel Spinel Ferrite. *J. Supercond. Nov. Magn.*, 2015. doi:10.1007/s10948-014-2861-0.
- [14] R. M. Bozorth et al. Anisotropy and magnetostriction of some ferrites. *Phys. Rev.*, 1955. doi:10.1103/PhysRev.99.1788.
- [15] J. M. D. Coey. *Magnetism and Magnetic Materials*. 2010. doi:10.1017/CB09780511845000.
- [16] H. Jin and T. Miyazaki. Magnetic Domain. In *The Physics of Ferromagnetism*, Springer Series in Materials Science, pages 261–286. Springer, 2012. doi:10.1007/978-3-642-25583-0_7.
- [17] S. Blundell. *Magnetism in Condensed Matter*. 2001.
- [18] W. A. Yager et al. Ferromagnetic resonance in nickel ferrite. *Phys. Rev.*, 1950. doi:10.1103/PhysRev.80.744.
- [19] D. W. Healy. Ferromagnetic resonance in nickel ferrite as a function of temperature. *Phys. Rev.*, 1952. doi:10.1103/PhysRev.86.1009.
- [20] A. B. Smith and R. V. Jones. Magnetostriction in Nickel Ferrite and Cobalt—Nickel Ferrite. *Journal of Applied Physics*, 2004. doi:10.1063/1.1708305.
- [21] R. M. Bozorth and J. G. Walker. Magnetostriction of single crystals of cobalt and nickel ferrites. *Phys. Rev.*, 1952. doi:10.1103/PhysRev.88.1209.
- [22] M. T. Johnson et al. Growth of nickel ferrite thin films using pulsed-laser deposition. *J. Cryst. Growth*, 1999. doi:10.1016/S0022-0248(99)00342-5.
- [23] S. Seifkar et al. Structural and magnetic properties of sol-gel derived NiFe₂O₄ thin films on silicon substrates. *J. Magn. Magn. Mater.*, 2014. doi:10.1016/j.jmmm.2014.03.004.
- [24] C. Klewe et al. Physical characteristics and cation distribution of NiFe₂O₄ thin films with high resistivity prepared by reactive co-sputtering. *J. Appl. Phys.*, 2014. doi:10.1063/1.4869400.
- [25] A. V. Singh et al. Bulk single crystal-like structural and magnetic characteristics of epitaxial spinel ferrite thin films with elimination of antiphase boundaries. *Adv. Mater.*, 2017. doi:10.1002/adma.201701222.

- [26] J. Shan et al. Nonlocal magnon spin transport in NiFe₂O₄ thin films. *Appl. Phys. Lett.*, 2017. doi:10.1063/1.4979408.
- [27] S. Matzen et al. Structure, magnetic ordering, and spin filtering efficiency of NiFe₂O₄(111) ultrathin films. *Appl. Phys. Lett.*, 2014. doi:10.1063/1.4871733.
- [28] H. J. Elmers et al. Submonolayer magnetism of Fe(110) on W(110): Finite width scaling of stripes and percolation between islands. *Phys. Rev. Lett.*, 1994. doi:10.1103/PhysRevLett.73.898.
- [29] J. Kołaczkiwicz and E. Bauer. The adsorption of Ni on W (110) and (211) surfaces. *Surf. Sci.*, 1984. doi:0.1016/0039-6028(84)90114-6.
- [30] P. Piercy et al. Phase diagram and critical behavior of the adsorption system O/Ru(001): Comparison with lattice-gas models. *Phys. Rev. B*, 1992. doi:10.1103/PhysRevB.82.024104.
- [31] J. de la Figuera et al. Electron reflectivity measurements of Ag adatom concentrations on W(110). *Surf Sci*, 2006. doi:10.1016/j.susc.2006.02.069.
- [32] B. Santos et al. Structure and magnetism in ultrathin iron oxides characterized by low energy electron microscopy. *J. Phys. Cond. Matt.*, 2009. doi:10.1088/0953-8984/21/31/314011.
- [33] L. Martín-García et al. Atomically flat ultrathin cobalt ferrite islands. *Adv. Mat.*, 2015. doi:10.1002/adma.201502799.
- [34] L. Martín-García et al. Initial stages of the growth of mixed iron-cobalt oxides on Ru(0001). *Phys. Procedia*, 2016. doi:10.1016/j.phpro.2016.11.075.
- [35] I. Palacio et al. Initial stages of FeO growth on Ru(0001). *J. Phys. Condens. Matter*, 2013. doi:10.1088/0953-8984/25/48/484001.
- [36] R. Luoma. A thermodynamic analysis of the system Fe-Ni-O. *CALPHAD*, 1995. doi:10.1016/0364-5916(95)00026-B.
- [37] J. I. Flege and E. E. Krasovskii. Intensity-voltage low-energy electron microscopy for functional materials characterization. *Phys. Status Solidi RRL*, 2014. doi:10.1002/pssr.201409102.
- [38] M. Monti et al. Magnetism in nanometer-thick magnetite. *Phys. Rev. B*, 2012. doi:10.1103/PhysRevB.85.020404.
- [39] W. Weiss and W. Ranke. Surface chemistry and catalysis on well-defined epi-

- taxial iron-oxide layers. *Prog. Surf. Sci.*, 2002. doi:10.1016/S0079-6816(01)00056-9.
- [40] G. S. Parkinson. Iron oxide surfaces. *Surf. Sci. Rep.*, 2016. doi:10.1016/j.surfrep.2016.02.001.
- [41] N. Spiridis et al. Superstructures on epitaxial Fe₃O₄(111) films: Biphasic formation versus the degree of reduction. 2019. doi:10.1021/acs.jpcc.8b11400.
- [42] A. D. Dalvi and W. W. Smeltzer. Thermodynamics of the Iron-Nickel-Oxygen System at 1000°C. *J. Electrochem. Soc.*, 1970. doi:10.1149/1.2407337.
- [43] G. Ketteler et al. Bulk and surface phases of iron oxides in an oxygen and water atmosphere at low pressure. *Phys. Chem. Chem. Phys.*, 2001. doi:10.1039/b009288f.
- [44] M. Rhamdhani et al. Subsolidus Phase Equilibria of the Fe-Ni-O System. *Metall. Mater. Trans. B*, 2008. doi:10.1007/s11663-008-9174-2.
- [45] C. M. Schneider and G. Schönhense. Investigating surface magnetism by means of photoexcitation electron emission microscopy. *Rep. Prog. Phys.*, 2002. doi:10.1088/0034-4885/65/12/202.
- [46] S. Da Col et al. Observation of Bloch-point domain walls in cylindrical magnetic nanowires. *Phys. Rev. B*, 2014. doi:10.1103/PhysRevB.89.180405.
- [47] D. Alders et al. Temperature and thickness dependence of magnetic moments in NiO epitaxial films. *Phys. Rev. B*, 1998. doi:10.1103/PhysRevB.57.11623.
- [48] M. Monti. *Ultrathin iron oxide films on Ru(0001)*. PhD thesis, 2014.
- [49] L. Martín-García. *Characterization of oxide surfaces and films: real-time growth, interface effects and magnetism*. PhD thesis, 2017.
- [50] E. Pellegrin et al. Characterization of nanocrystalline γ -Fe₂O₃ with synchrotron radiation techniques. *Phys. Stat. Sol. (b)*, 1999. doi:10.1002/(SICI)1521-3951(199909)215:1<797::AID-PSSB797>3.0.CO;2-D.
- [51] R. A. D. Pattrick et al. Cation site occupancy in spinel ferrites studied by x-ray magnetic circular dichroism developing a method for mineralogists. *Eur. J. Mineral.*, 2002. doi:10.1127/0935-1221/2002/0014-1095.
- [52] H. Ikeno. First-principles analysis of x-ray magnetic circular dichroism for transition metal complex oxides. *J. Appl. Phys.*, 2016. doi:10.1063/1.4961713.

- [53] K. Wandelt and G. Ertl. Electron spectroscopic studies of the oxidation of Fe/Ni alloys. *Surf. Sci.*, 1976. doi:[10.1016/0039-6028\(76\)90248-X](https://doi.org/10.1016/0039-6028(76)90248-X).
- [54] S. E. Greco et al. Oxidation of the (100) surface of a NiFe alloy. *Surf. Sci.*, 1982. doi:[10.1016/0039-6028\(82\)90282-5](https://doi.org/10.1016/0039-6028(82)90282-5).
- [55] S. Ruiz-Gómez et al. Geometrically defined spin structures in ultrathin Fe₃O₄ with bulk like magnetic properties. *Nanoscale*, 2018. doi:[10.1039/C7NR07143D](https://doi.org/10.1039/C7NR07143D).
- [56] A. Vansteenkiste et al. The design and verification of MuMax3. *AIP Advances*, 2014. doi:[10.1063/1.4899186](https://doi.org/10.1063/1.4899186).
- [57] G. Rasic and J. Schwartz. On the origin of coercivity reduction in surface patterned magnetic thin films. *Phys. Stat. Sol. (a)*, 2015. doi:[10.1002/pssa.201431434](https://doi.org/10.1002/pssa.201431434).
- [58] A. R. O. Rodrigues et al. Magnetic liposomes based on nickel ferrite nanoparticles for biomedical applications. *Phys. Chem. Chem. Phys.*, 2015. doi:[10.1039/C5CP01894C](https://doi.org/10.1039/C5CP01894C).
- [59] M. Hoppe. *Magnetic, structural, and electronic properties of NiFe₂O₄ ultrathin films*. 2016.
- [60] A. Bhosale and B. Chougule. X-ray, infrared and magnetic studies of al-substituted ni ferrites. *Mater. Chem. Phys.*, 2006. doi:<https://doi.org/10.1016/j.matchemphys.2005.08.022>.
- [61] H. Perron et al. Structural investigation and electronic properties of the nickel ferrite NiFe₂O₄: a periodic density functional theory approach. *J. Phys.: Condens. Matter*, 2007. doi:[10.1088/0953-8984/19/34/346219](https://doi.org/10.1088/0953-8984/19/34/346219).
- [62] Z. Szotek et al. Electronic structures of normal and inverse spinel ferrites from first principles. *Phys. Rev. B*, 2006. doi:[10.1103/PhysRevB.74.174431](https://doi.org/10.1103/PhysRevB.74.174431).
- [63] C. T. Chen et al. Experimental confirmation of the x-ray magnetic circular dichroism sum rules for iron and cobalt. *Phys. Rev. Lett.*, 1995. doi:[10.1103/PhysRevLett.75.152](https://doi.org/10.1103/PhysRevLett.75.152).
- [64] D. J. Huang et al. Spin and orbital magnetic moments of Fe₃O₄. *Phys. Rev. Lett.*, 2004. doi:[10.1103/PhysRevLett.93.077204](https://doi.org/10.1103/PhysRevLett.93.077204).
- [65] T. Saitoh et al. Systematic variation of the electronic structure of 3d transition-metal compounds. *Phys. Rev. B*, 1995. doi:[10.1103/PhysRevB.52.7934](https://doi.org/10.1103/PhysRevB.52.7934).

- [66] E. Goering et al. Vanishing Fe 3d orbital moments in single-crystalline magnetite. *Europhys. Lett.*, 2006. doi:10.1209/epl/i2005-10359-8.
- [67] G. F. M. Gomes et al. Magnetic moment of Fe₃O₄ films with thicknesses near the unit-cell size. *Phys. Rev. B*, 2014. doi:10.1103/PhysRevB.90.134422.
- [68] L. Martín-García et al. Spin and orbital magnetic moment of reconstructed $\sqrt{2} \times \sqrt{2}$ R45° magnetite(001). *Phys. Rev. B*, 2015. doi:10.1103/PhysRevB.91.020408.
- [69] N. Spiridis. 2018.
- [70] S. Gallego. 2019.
- [71] D. J. Huang et al. Orbital magnetic moments of oxygen and chromium in CrO₂. *Phys. Rev. B*, 2002. doi:10.1103/PhysRevB.66.174440.

5 Mixed nickel-cobalt oxide - $\text{Ni}_x\text{Co}_{1-x}\text{O}$

The results presented in this chapter are published in:

- A. Mandziak, G. D. Soria, J. E. Prieto, P. Prieto, C. Granados-Mirallas A. Quesada, M. Foerster, L. Aballe, J. de la Figuera *Tuning the Néel temperature in an antiferromagnet: the case of $\text{Ni}_x\text{Co}_{1-x}\text{O}$ microstructures*, Scientific Reports (2019) 9:13584

5.1 Introduction

Binary metal-oxide systems (Me_xO_y) are attractive because of their potential applications in different areas ranging from catalysis to spintronics. From the magnetic point of view much effort has been focused on oxide thin films, containing 3d transition metals like Fe, Co or Ni, considering their importance in magnetic devices technology. Their antiferromagnetic properties have a great potential in the next generation of spintronic devices[1]. Already in current devices such as magnetic tunnel junctions and high-density memories, antiferromagnetic materials (AF), sometimes of nanometer thickness[2], are used to modify the switching behavior of adjacent ferromagnets (FM) through the exchange bias effect[3], or are used to tailor their interactions in dense nonvolatile information storage [4]. Antiferromagnets possess a number of interesting properties in this area such as robustness against perturbations due to magnetic fields, absence of parasitic stray fields, ultrafast dynamics (up to THz ranges)[5] and large magnetotransport effects[6]. It is thus desirable to tune and understand the spin structure and properties of nanometric antiferromagnetic films not only for applications but also to get insight into fundamental magnetic phenomena [7–10].

Here we focus on nickel and cobalt oxides, especially on their mixed form. Nickel oxide or cobalt oxide films have previously been grown by oxygen-assisted molecular beam epitaxy on different oxide substrates such as MgO[11–17]. Less common is the growth on metallic substrates where Ir(100)[18] or PtFe[19] have been used, in addition to Ru(0001)[20; 21]. Both oxides have also been grown in order to study the proximity effect at their common interface[17; 22]. However, the growth of thin films of mixed Ni-Co oxides, to the best of our knowledge, has been only attempted trying to obtain nickel cobaltite[23–25].

5.2 Magnetic structure

Nickel and cobalt oxide are both antiferromagnetic insulators¹. In the paramagnetic phase, CoO and NiO crystallize in the rocksalt structure with similar lattice spacing. Below respective Néel temperature (Table 5.1) they exhibit an antiferromagnetic ordering, originating from the Anderson-type superexchange interaction (type II). The II type of antiferromagnetic ordering is one where the cation magnetic moments are arranged ferromagnetically within the (111) planes and alternating planes are antiferromagnetically coupled along the $\langle 111 \rangle$ directions [26]. In the case of NiO the spins lie in the (111) planes and within each one their direction can point along one of the three equivalent $\langle 211 \rangle$ directions, giving rise to a total of 12 different domains.

¹They are considered as an intermediate insulators between Mott-Hubbard and charge transfer one.

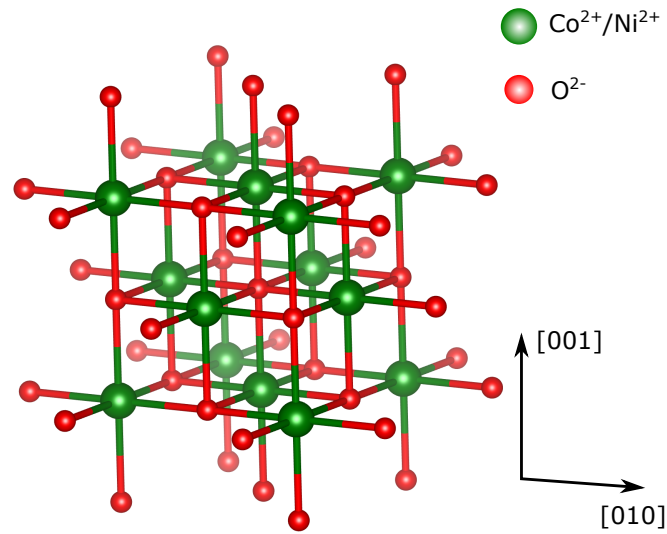


Figure 5.1: Schematic illustration of nickel oxide/cobalt oxide crystal structure.

CoO stands out for presenting a large 1.2% tetragonal contraction[26] below the Néel temperature, which is due to an orbital-ordering inducing Jahn-Teller effect. It leads to a reduction of the crystal symmetry to a monoclinic structure. In the case of NiO the magnetic phase transition also goes along with the an structural one, lowering the symmetry of the crystal from rocksalt to rhomboherdal one. However, the distortion in NiO is much smaller than the one observed for CoO. Thus, the antiferromagnetic domain distribution in CoO is more complex and still under debate [27]. Both NiO and CoO have sizeable magnetic orbital moments of $0.17 \mu_B$ and $0.25 \mu_B$ per formula unit, respectively[28–30].

Oxide	Electronic configuration		Insulating gap (eV)	Néel temperature (K)	Lattice constant (nm)
	O ²⁻	TM ²⁺			
CoO	[He]2s ² 2p ⁶	[Ar]3d ⁷	2.5-6	293	0.426
NiO	[He]2s ² 2p ⁶	[Ar]3d ⁸	3.1-4.3	525	0.417

Table 5.1: Electronic configuration, measured insulating gap, Néel temperature and lattice constant in CoO and NiO.

According to the Co-Ni-O phase diagram, there is a large miscibility region where a mixed Co-Ni rocksalt phase should be stable[31]. In fact, Carey and Berkowitz[32] used Co_xNi_{1-x}O films to modify the exchange coupling with ferromagnetic layers, suggesting that the Néel temperature could be modified in this way.

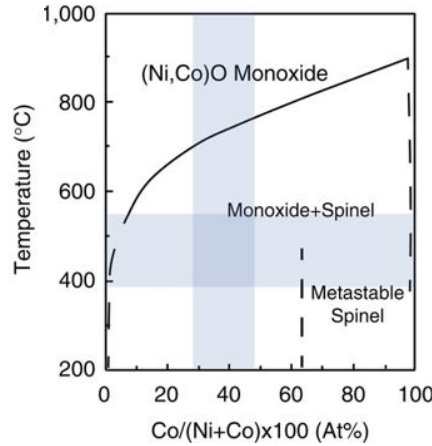


Figure 5.2: The phase diagram of $\text{CoO}_x\text{-NiO}_x$ system at one atmosphere pressure adapted from ref. 40

Antiferromagnetic anisotropy

The magnetic anisotropy is well known in ferromagnetic materials and has been studied for a long time. However in antiferromagnetic systems it has been unveiled quite recently. For example, thin NiO films, epitaxially grown on a MgO substrate, revealed an out-of-plane uniaxial anisotropy which changed with the film thickness[11]. The same behaviour was observed for CoO thin films grown on MnO and Ag(001), respectively[13]. In the latter the mismatch between the substrate and thin layer induced a strain and it was found that, if there is a tetragonal compression the spin axis is in the surface plane, while for tensile strain the out-of-plane alignment is favoured[33].

In the following we will take a close up look at possible sources of AF magnetic anisotropy.

1. Magnetocrystalline anisotropy - it couples the spin to the crystallographic axes through the spin-orbit interaction. A sizeable anisotropy can emerge once the symmetry of the lattice is reduced and the degeneracy of the ground state is lifted. This is normally caused by a small perturbation as e.g. strain or structural distortion. It has been found theoretically that the dependence of the total energy $E(S)$ on the spin direction is described by the following formula:

$$E(\theta, \phi) = E(0, 0) + \Delta E(\theta, \phi) \quad (5.1)$$

where $E(0, 0)$ is the direction-independent contribution, while $\Delta E(\theta, \phi)$ is the angular-dependent variation, whose minimum with respect to the polar angles θ and ϕ corresponds to the easy axis S_0 of the total magnetization.

For example, this anisotropy term is negligible for NiO (according to DFT calculations it amounts to about $15 \mu\text{eV}$) where the spin-orbit coupling is very small (the d ground state has completely filled t_{2g} state and partially filled e_g). In this compound, the most important contribution to the total anisotropy is provided by dipole-dipole interaction[34].

The situation is quite different for CoO. In cobalt oxide the domains orientation is strongly determined by the coupling between the spins and crystal field resulting from the spin orbit coupling and a large orbital magnetic moment. It has been shown that the variation $\Delta E(\theta, \phi)$ is two orders of magnitude higher than in the nickel oxide. The anisotropy energy for systems with monoclinic or rhombohedral symmetry can be described by:

$$\Delta E(\theta, \phi) = \sin^2(\theta - \theta_0)K + K' \cos[2(\phi - \phi_0)] \quad (5.2)$$

where the K and K' represent two anisotropy constants and polar angles θ_0 and ϕ_0 define the easy axis. The anisotropy constants have been determined for both CoO and NiO. The calculated values of K and K' are 1.243 meV per atom and -0.818 meV for cobalt oxide and -0.013 meV and 0.002 meV for nickel oxide, respectively[35]. The values obtained for NiO are very small due to weak variation of $\Delta E(\theta, \phi)$, hence confirming that the magnetocrystalline anisotropy does not strongly influence the total energy of the system.

2. Dipolar anisotropy - long range magnetic dipole-dipole interaction plays an important role in determining the antiferromagnetic structure in such oxides as for example NiO[33]. As it was already mentioned before, nickel oxide has a rocksalt structure and in its AF phase presents small rhombohedral distortion along the [111] direction. In such systems, the magnetic anisotropy contribution to the total dipole effect is given by the following formula:

$$\Delta E = K_d \sin^2 \theta \quad (5.3)$$

where K_d is the anisotropy constant and θ the angle between spin axis and [111] direction. A positive K_d leads to an easy axis along the [111] direction, while the negative one to the easy plane perpendicular to [111] as shown in Figure 5.3.

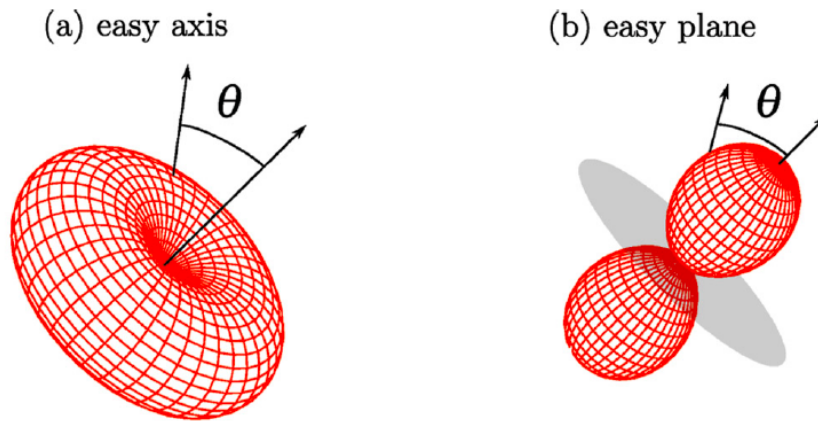


Figure 5.3: Isosurface of the magnetic anisotropy energy for (a) $K_d < 0$ and (b) $K_d > 0$. Reprinted from [35].

The material dependence of the anisotropy constant K_d is given by the factor $(\frac{\mu^2}{a_0^3})$. Thus, it has been determined for NiO that the anisotropy constant K_d related to dipole-dipole interaction, is slightly higher (-0.05 meV) than the constants K, K' due to spin orbit-coupling. For CoO the anisotropy constant was found (to 0.126 meV). The absolute value of K_d for cobalt oxide reveals the insignificance of the anisotropy effects coming from dipole interaction in comparison to the SO contribution[34].

The aforementioned theory of magnetic anisotropy allows to determine the easy axis of an antiferromagnet. In the following we will show how to obtain the AF domains in the dichroic XPEEM, the only technique which gives a direct access to AF domains (excluding neutron diffraction). However, the data treatment is more complicated than XMCD for ferro (ferri-)magnetic materials.

5.3 Growth mode and particle shape

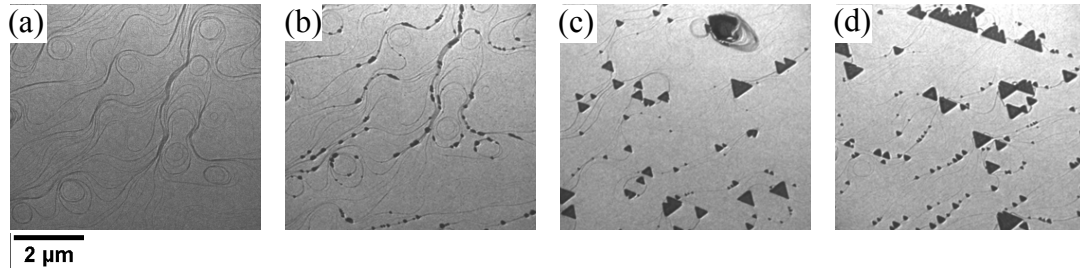


Figure 5.4: Selected frames from a sequence of LEEM images acquired during the growth of $\text{Ni}_x\text{Co}_{1-x}\text{O}$ (ratio Ni:Co 1:2) at 1150 K at a background pressure of 1×10^{-6} mbar of molecular oxygen. The frames correspond to (a) 0 sec, (b) 3 min, (c) 20 min and (d) 45 min after opening the doser shutters. The electron energy is 5 eV.

The growth process of $\text{Ni}_{1-x}\text{Co}_x\text{O}$ was observed in real space and real time in a LEEM microscope. We deposit nickel and cobalt on Ru(0001) at elevated temperature (1150 K) while exposing it to molecular oxygen. As a first step the bare Ru substrate is exposed to molecular oxygen. Oxygen adsorbs on the Ru crystal at high temperature increasing the work function and forming a 2-dimensional atomic oxygen gas, as reported in the previous Chapter 4. The increase of the work function is due to the electron transfer from the substrate towards the O adatoms, according with the high electronegativity of oxygen.

A sequence of images of the growth process is shown in Figure 5.4. The LEEM image of the substrate just after opening the Co and Ni evaporators is presented in Figure 5.4b. Many small nuclei decorate the step edges of the substrate. The dosing rate was adjusted to obtain samples with different compositions (at rates of the order of 10^{-3} $\text{ML}_{\text{Ru}}/\text{s}$). Three samples with Ni:Co ratios of 1:2, 1:6 and 0:1 (i.e., pure cobalt oxide) will be analyzed in the following. It was previously reported that the growth of CoO on Ru(0001) takes place in the Volmer-Weber mode, where 3-dimensional islands nucleate from the beginning[20]. The same growth mode is observed for the mixed NCO samples. We have not detected any influence of the Ni:Co ratio on the growth mode. As in the case of pure CoO islands, mixed oxide islands mostly present a triangular shape with two opposite orientations[20]. Similar triangular islands are also observed when growing spinels ferrites containing Fe^{3+} cations on Ru (0001) by the same method[36]. Additionally, some rectangular shaped islands are found.

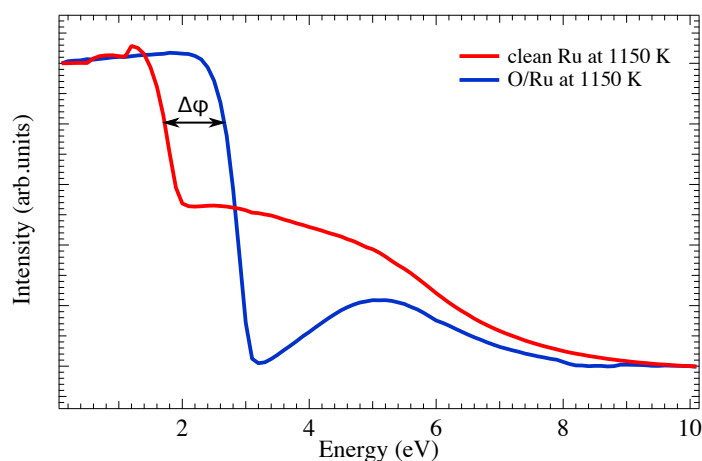


Figure 5.5: LEEM IV spectra acquired at high temperature (1150 K) on bare Ru substrate and cover with oxygen (1×10^{-6} mbar).

We first study the surface structure of each island type by LEED. The diffraction patterns are presented in Figure 5.6b–d. The brightest spots correspond to the 1st order Ru diffracted beams. Adsorbed surface oxygen gives rise to a 2×2 LEED pattern at room temperature (marked with a magenta diamond). In addition to the patterns arising from the bare ruthenium and the oxygen superstructure, we can distinguish a hexagonal pattern (marked with a green hexagon), rotated clockwise by 5° with respect to the Ru one and a square one (marked with a blue square).

We attribute the hexagonal pattern to the triangular islands, and the square pattern to the rectangular ones. Performing micro-spot LEED by using an aperture to select the area from which the pattern is obtained (areas for μ -LEED are shown as insets in Figure 5.6a), we confirm this assignment, as shown in Figure 5.6c–d. The two kind of islands thus correspond to different crystallographic orientations. On the basis of LEED patterns we can estimate the lattice spacing for each island type. The lattice spacing for the triangular islands is (0.29 ± 0.05) nm, slightly larger than the Ru(0001) value, 0.27 nm (see Figure 5.6c). The in-plane lattice spacing for the (111)-oriented rock-salt phases should be 0.29 nm for NiO and 0.30 nm for CoO, in good agreement with the observed value. Thus, we identify the triangular islands as islands oriented along the (111) plane. The square pattern corresponds to a lattice spacing of (0.31 ± 0.05) nm, to be compared with the expected value for CoO(001) of 0.32 nm. This suggests that the square-shaped islands have the (001)-orientation. It has to be noted that not all the possible domains are observed in the LEED patterns of Figure 5.6b, because of the reduced number of islands in the field of view.

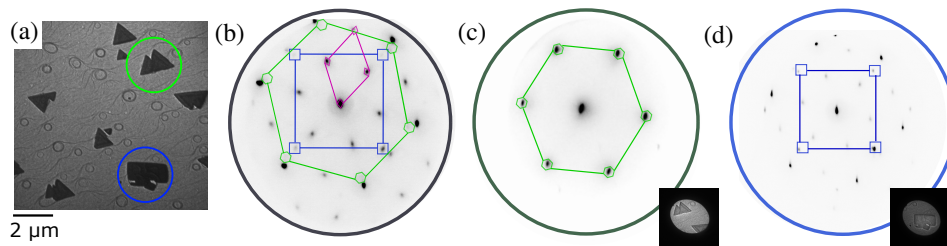


Figure 5.6: LEEM image (a) and corresponding LEED patterns at 45 eV electron energy from different regions on the sample (ratio Ni:Co 1:2) (b) substrate plus islands, (c) triangular islands, (d) rectangular island. The corresponding selected areas for the LEED are shown as insets.

Besides for CoO and $\text{Ni}_{1-x}\text{Co}_x\text{O}$, also for cerium oxide on Ru(0001) it was reported[37] that islands with two orientations, (001) and (111), can be grown depending on the oxygen background pressure. In an oxygen-rich environment the ceria islands tend to be grown in the CeO_2 (001) orientation, while an oxygen lean-environment favors the (111) one [38].

The thickness of the islands can be estimated from the shadows observed in the XPEEM images (see Figure 5.7a). As x-rays are hitting the sample at a polar angle of 16° (with respect to the surface plane), thick enough islands will cast a measurable shadow on the substrate as schematically shown in Figure ??b. Typical heights for the observed islands are tens of nanometers or less (e.g. the island shown in Figure 5.7a is 70 nm high).

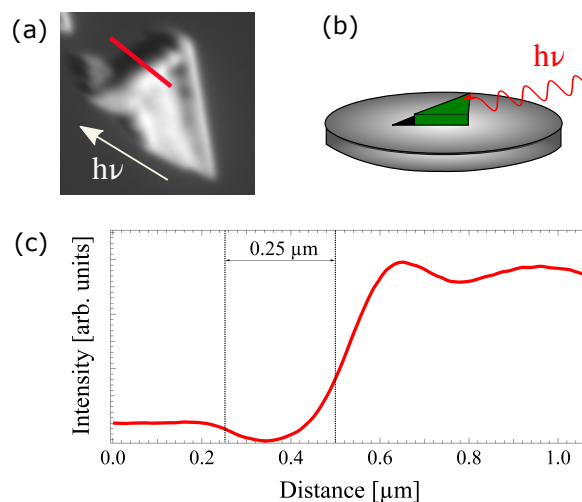


Figure 5.7: a) XAS image acquired at photon energy close to the maximum of Co L_3 absorption edge. (b) Experimental setup. (c) Cross section through the island edge in the XAS image shown in Fig. 5.7a.

5.4 Chemical and magnetic properties

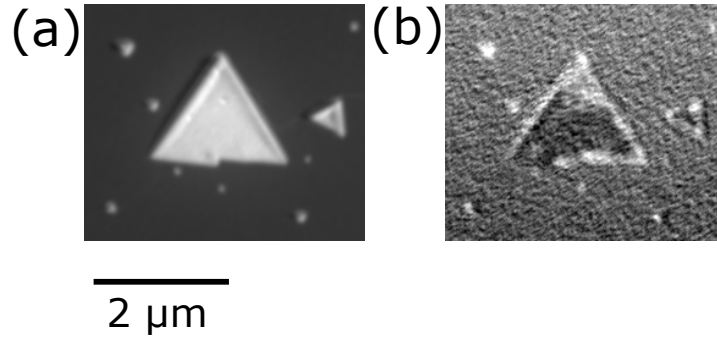


Figure 5.8: (a) Co XAS-PEEM images acquired at the respective L_3 edges. (b) Co XMLD-PEEM images acquired in the same location of a $\text{Ni}_x\text{Co}_{1-x}\text{O}$ (ratio Ni:Co 1:2) island on Ru(0001).

From stacks of PEEM images collected at different photon energies, spanning the Co and Ni $L_{3,2}$ -edges the XAS spectra can be extracted from selected areas on the surface. This was done for example for the island shown in Fig. 5.8a. Figure 5.9, 5.10, 5.11 shows XAS spectra at the Co $L_{3,2}$ (5.9), Ni $L_{3,2}$ (6.8) and O K (5.11) edges XAS for linear horizontal ($\theta = 0^\circ$) and linear vertical polarizations ($\theta = 74^\circ$) extracted from single domain regions. It should be pointed out that while for $\theta = 0^\circ$ the polarization is fully in the surface plane, for vertical polarization of the synchrotron radiation, the electric field is not strictly perpendicular to the surface, as the photons incidence angle is 16° with respect to the surface. The difference between both spectra gives a clear dichroic signal. As explained in chapter 3.3.4.1, linear dichroism measures the charge anisotropy associated with both the local crystal field and the local exchange field through spin-orbit coupling[39]. The latter contribution is known as X-ray Magnetic Linear Dichroism (XMLD). The XAS spectra can be used as well to obtain information on the cation oxidation state. The triangular and rectangular (not shown) islands present the same spectra, typical for Ni^{2+} and Co^{2+} . Co^{2+} in CoO has a characteristic four peak structure at the L_3 edge [19] and Ni^{2+} in NiO has a characteristic double peak structure at both edges[16]. Additionally, spectra at the oxygen K edge were acquired for both polarizations from a single domain area. The spectra together with their difference (i.e., the X-ray Linear Dichroism (XLD) signal) are shown in Figure 5.11. The oxygen spectrum is similar to that of nickel oxide reported by Arenholz[15] with a peak at a photon energy of 540.2 eV. Thus the chemical identity of the islands is confirmed to correspond to $\text{Ni}_{1-x}\text{Co}_x\text{O}$.

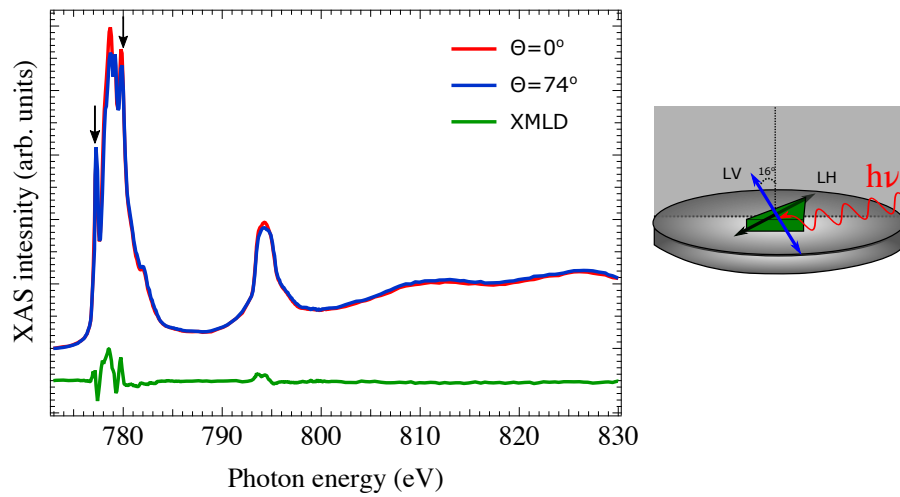


Figure 5.9: Experimental polarization dependent Co L-edge XAS and XMLD spectra acquired in the dark region of the triangular island presented in Fig. 5.8. θ is the angle between the light polarization vector and the surface. In the right panel a relative orientation of polarization and sample for vertical and horizontal polarization.

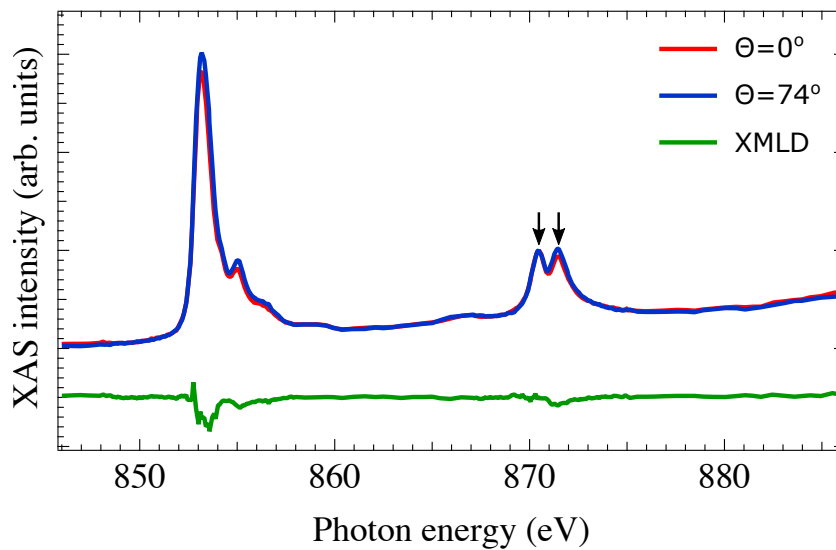


Figure 5.10: Experimental polarization dependent Ni L-edge XAS and XMLD spectra acquired in the dark region of the triangular island presented in Fig. 5.8.

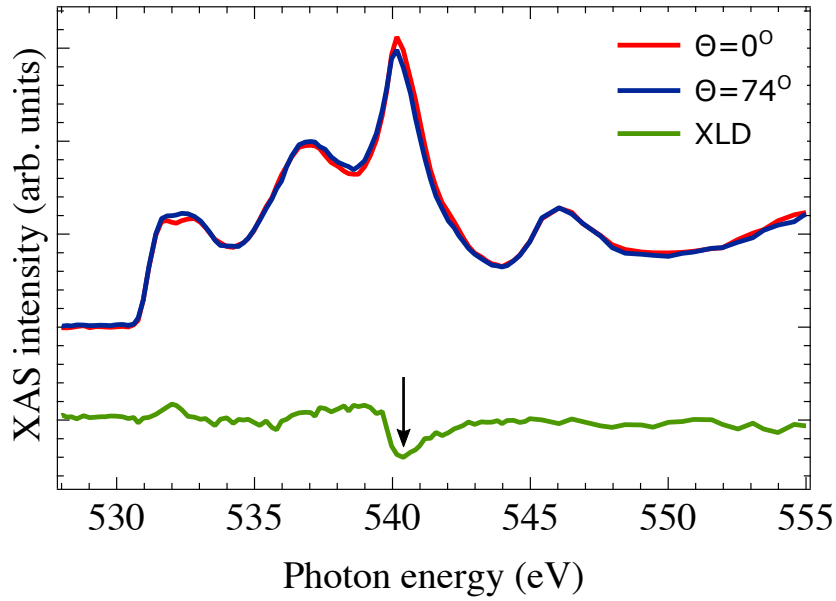


Figure 5.11: Experimental polarization dependent O K-edge XAS and XLD spectra acquired in the dark region of the triangular island presented in Fig. 5.8.

The composition can be roughly estimated by measuring the edge jump of the XAS spectra which is proportional to the number of absorbing atoms in the sample and the linear absorption coefficient (Table 4.1[40]). Estimated values are in good agreement with the deposited ratio for all samples (shown in Tab. 5.2). It should be noted that the probing depth is limited to the near surface region due to the short escape depth of photoelectrons (much shorter than the x-rays penetration depth)[41; 42]. Thus the composition is actually measured for the top few nm only.

	Evaporator flux	XAS edge jump (corrected by taking into account linear absorption coefficient) (arb. units)
$\text{Ni}_{0.33}\text{Co}_{0.67}\text{O}$		
Ni	$8.3 \times 10^{-4} \text{ML/sec}$	1.15
Co	$1.6 \times 10^{-3} \text{ML/sec}$	2.34
$\text{Ni}_{0.14}\text{Co}_{0.86}\text{O}$		
Ni	$5.5 \times 10^{-4} \text{ML/sec}$	0.71
Co	$3.3 \times 10^{-3} \text{ML/sec}$	4.25
CoO		
Co	$1.6 \times 10^{-3} \text{ML/sec}$	2.78

Table 5.2: The Ni/Co flux ratio used during growth and the estimated values obtained by analysis of the XAS data for the different samples.

X-ray Magnetic Linear Dichroism

In order to check whether the dichroic signal in our mixed nickel-cobalt oxide samples comes from an antiferromagnetic ordering, we have studied in detail the Ni and Co L_3 peak positions. It is known that if the symmetry of the material under investigation is exactly cubic, no crystal field dichroism will occur[12] and thus any observed contrast must arise from magnetic ordering. However, if the structure deviates from cubic symmetry (e.g. because of epitaxial strain in a thin film), the crystal field dichroism has to be taken into account[12; 13]. In order to rule out the latter contribution we have examined the energy shift ΔE in the main peak of the Ni and Co L_3 edges between $\theta = 0^\circ$ and $\theta = 90^\circ$. A close-up of this region is given in Figure 5.12. There is no measurable shift between the two spectra acquired at horizontal and vertical polarization in the case of the Co L_3 peak, and for the Ni one. Thus the crystal field effect is not observable in our systems. This is already a strong hint that the observed contrast is dominated by magnetic dichroism, directly related to the presence of long-range antiferromagnetic spin order in $\text{Ni}_{1-x}\text{Co}_x\text{O}$. This is further confirmed by the different domain configuration found at the oxygen edge and by the temperature dependent measurements below.

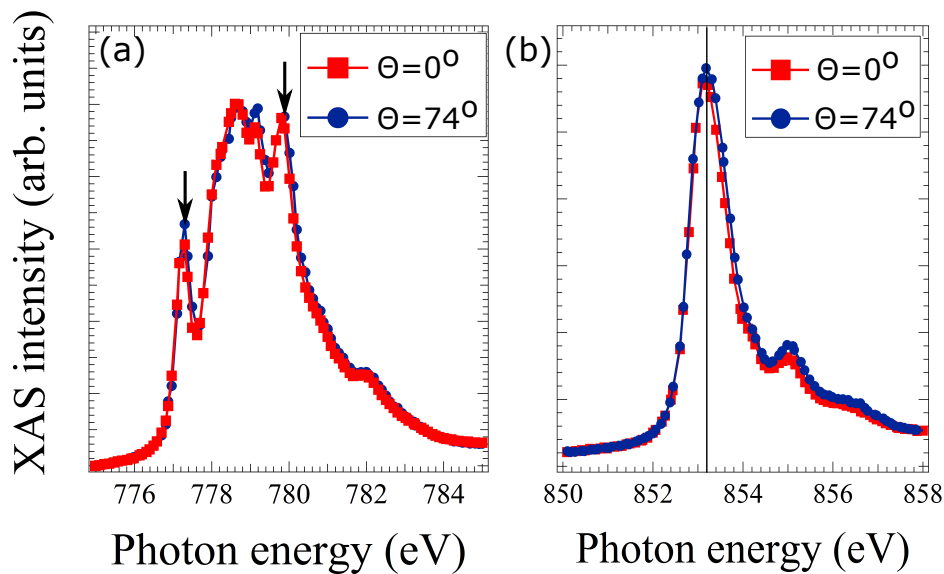


Figure 5.12: Experimental polarization dependent Co and Ni L_3 XAS spectra acquired in the dark central domain of the triangular island presented in Fig. 5.8b.

The situation is quite different for oxygen. In NiO, each O atom is surrounded by six Ni atoms whose moments are antiferromagnetically aligned. Thus the O XLD signal shown in Figure 5.11 cannot be due to a magnetic effect. Kinoshita et al.[43] showed that XLD is then due to crystal distortion and can be therefore employed to map the structural domains in the near surface region.

Antiferromagnetic domains

The domain patterns shown in Figure 5.13 were obtained with linearly polarized light parallel. The images were generated by dividing an image acquired at 777.5 eV, by one recorded at 780 eV corresponding to the first and the last peak of XAS signal at the Co L_3 edge, while the one at Ni at 870.3 eV, by one recorded at 871.5 eV, two peak of XAS signal at the Ni L_2 edge, respectively (indicated by arrows in Figures 5.9 5.10. The domain pattern at the O image were obtained at the maximum of dichroic signal at the O K edge. The strongest magnetic contrast was achieved by calculating the asymmetry of two images at energies as proposed by [44–46]. This contrast arises from the charge anisotropy associated with both the local crystal field and the local exchange field through spin-orbit coupling i.e., the AF part[19]. The distribution of the domains observed at Co and Ni edges correlate exactly with each other. Additional to the large triangular islands, small single-domain islands are also observed. However, the domains visible at the oxygen edge are different. This is a strong indication that dichroic contrast at Co and Ni edges is indeed of magnetic origin, since the cation edge dichroic images are sensitive to domains with different spin directions in addition to different ordering directions, while the anion edge is only sensitive to the latter[15; 47]. The determination of the spin and ordering axis of each domain by means of XMLD is much more complicated and will be analyzed for an other system in the next Chapter. Here we emphasize how the high crystalline quality of our films results in domains of up to micrometer size, much larger than typically found in NiO and CoO thin films[47].

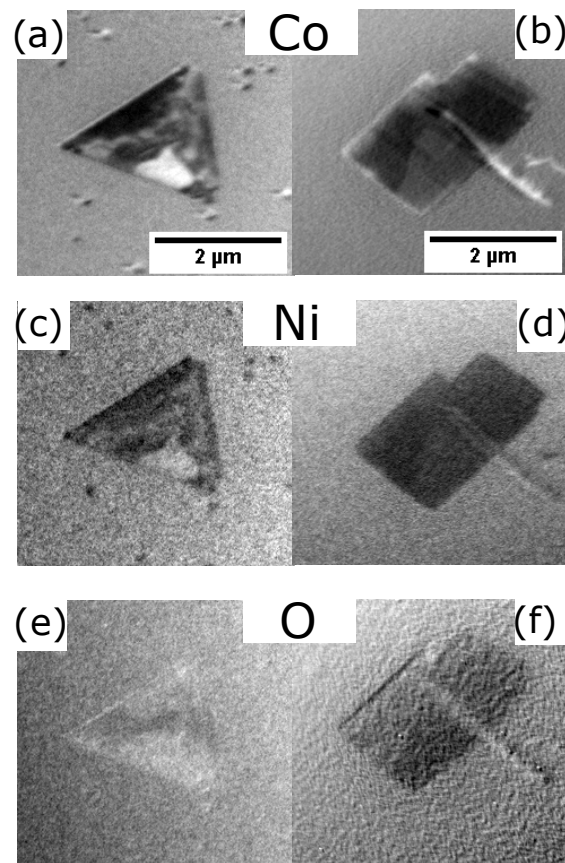


Figure 5.13: XMLD PEEM images for NCO/Ru(0001) measured at (a)-(b) Co L_3 , (c)-(d) Ni L_2 and (e)-(f) O K edges for both types of islands found on the surface.

5.5 Néel temperature dependence on composition

The definitive proof of the magnetic origin of the observed linear dichroism is to heat the film above the ordering temperature of the material, i.e. the Néel temperature. In the case that the observed contrast disappears above a certain temperature, one can conclude that the contrast must be related to the magnetic ordering. In the case of mixed nickel-cobalt oxides, the precise Néel temperature is not known but it is expected to be between the values for the pure oxides (293–525 K). As we already see a contrast at RT, we can expect that by adjusting the Ni:Co ratio we should be able to increase the Néel temperature above the CoO one.

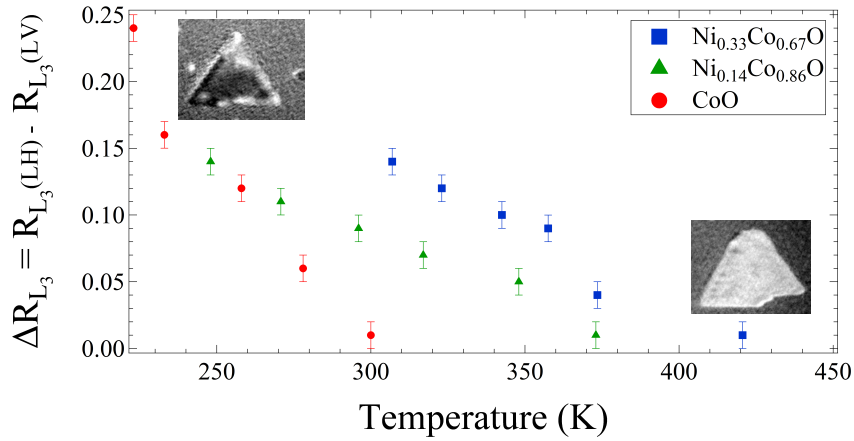


Figure 5.14: Temperature dependence of the asymmetry measured as a Co L_3 ratio difference ΔRL_3 for samples with different composition. In the inset XMLD PEEM images at the Co L_3 edge of $\text{Ni}_{0.33}\text{Co}_{0.67}\text{O}$ at RT (upper left) and above the Néel temperature (bottom right).

We now determine the Néel temperature for each sample. Following Wu et al.[48] and [17], we employ the intensity ratio RL_3 , which is a measure of long range magnetic order, between the first and the last peak at the Co L_3 edge (A and B, marked by arrows in the Figure 5.12) in order to follow the temperature dependence. It is proportional to the overall anisotropy, which tracks the magnetic order. Thus we plot $\Delta RL_3 = RL_3(0^\circ) - RL_3(90^\circ)$ vs temperature (Figure 5.18). Using these plots, we determine the Néel temperature for each sample (Figure 5.18). For a Ni:Co ratio of 1:2 the transition temperature is 425 K, for Ni:Co 1:6 $T_N = 375$ K and for CoO it is 295 K, very close to that of bulk CoO. We thus have shown that the Néel temperature can be modified at will by selecting the proper Co:Ni ratio.

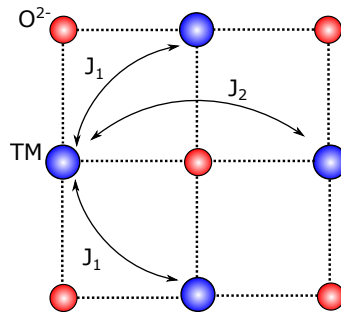


Figure 5.15: Schematic representation of the magnetic interactions in a (100) plane of rocksalt structure of TMOs.

A similar behavior was observed for epitaxial NiO/CoO films grown on MgO substrates [17]. Therein the enhancement of the Néel temperature was induced by a

proximity effect. The T_N of CoO in a bilayer was higher than without the NiO layer and reached a maximum at the interface owing to the interfacial nature of the exchange coupling. In our system there is a mixture of Co and Ni cations within the rocksalt structure. So now the superexchange interaction will depend on the particular cation distribution around a given one. One can expect that the exchange constant $J_{i,j}$ for nearest neighbours will be between the -0.69 meV value of NiO and -0.71 meV of CoO, and between -8.66 meV and -6.30 meV for next-nearest neighbors, respectively (see Figure 5.15). Based on the calculated magnetic exchange interaction constants one can conclude that by mixing two ions with different $J_{i,j}$ we can tune the interaction between them and thus modify the T_N in a controlled way[49; 50].

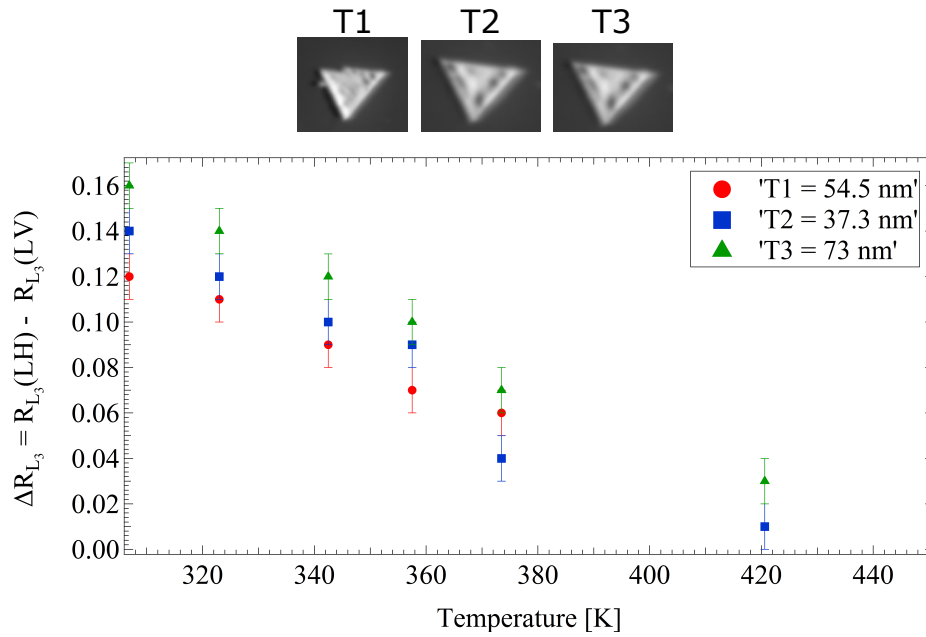


Figure 5.16: Temperature dependence of the asymmetry measured as a Co L_3 ratio difference ΔR_{L_3} for $\text{Ni}_{0.33}\text{Co}_{0.67}\text{O}$ islands with different thickness.

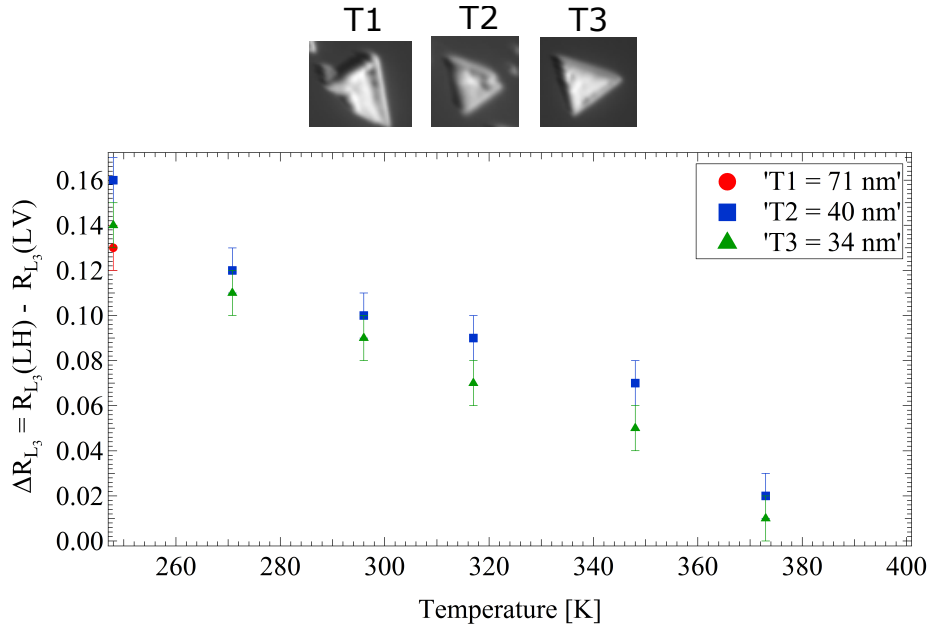


Figure 5.17: Temperature dependence of the asymmetry measured as a Co L₃ ratio difference ΔR_{L_3} for $\text{Ni}_{0.014}\text{Co}_{0.86}\text{O}$ islands with different thickness.

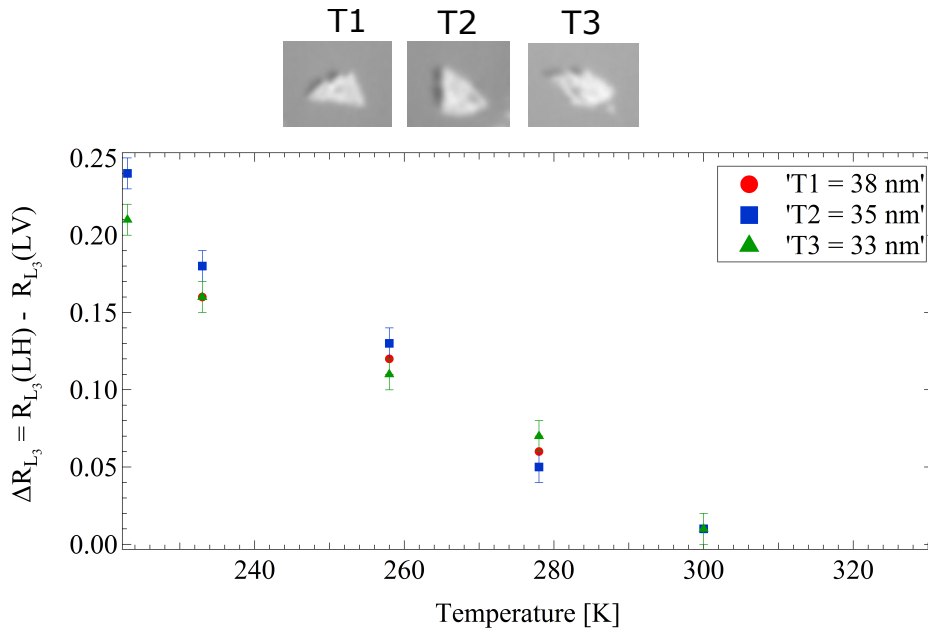


Figure 5.18: Temperature dependence of the asymmetry measured as a Co L₃ ratio difference ΔR_{L_3} for CoO islands with different thickness.

In order to investigate if T_N depends on the film thickness, we have used the same method for islands with different thickness (between 20 and 80 nm). Our results do not show any thickness dependence, confirming previous experiments [51–53] which claimed that finite size effects appear only in films thinner than 10 nm. Note that the height of our mixed oxide islands is tens of nanometers, i.e., above such limit.

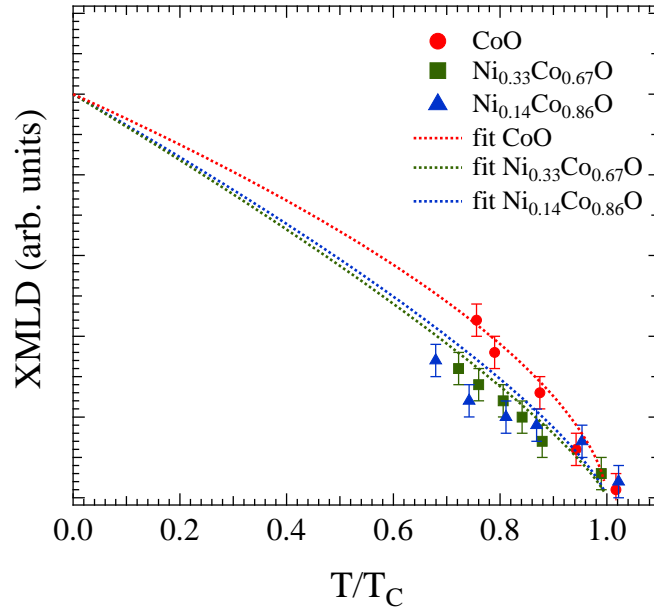


Figure 5.19: Temperature dependence of the asymmetry measured as a Co L_3 ratio difference ΔRL_3 for CoO islands with different thickness.

Additionally, in order to quantify the ordering parameter β , the experimental XMLD contrast values from the samples of different composition have been fitted to the universal relationship $\langle \mu^2 \rangle$ minus the isotropic value $1/3J(J+1)$, $J=1$ (Figure 5.19). The latter provides the major contribution to the XMLD contrast[54]. The expectation value of the magnetic moment $\langle \mu \rangle$ which determines the magnitude of XMCD contrast scales like $\langle \mu \rangle \propto (T_{crit} - T)^\beta$. Since XMLD is proportional to $\langle \mu^2 \rangle$, the contrast will scale like $(T_{crit} - T)^{2\beta}$.

As can be clearly seen in Figure 5.19 the dichroic contrast follows non-linear relation for the temperature higher than $0.7T_N$. By fitting the function $(T_{crit} - T)^{2\beta}$ to the experimental points we obtain $\beta = 0.32 \pm 0.03$ for samples with different composition. Thus, that the data are in a good accordance with 3D Ising model. However, the 3D Heisenberg picture with $\beta = 0.38$ cannot definitely be excluded. If we take into account other models for critical behaviour the 3D mean-field picture with $\beta = 0.5$ (as found for other antiferromagnets [55]) can be ruled out, since the XMLD does not scale linearly near the T_{crit} . A 2D Ising or mean-field model can be completely excluded as the first one with $\beta = 1/8$ would yield a much steeper descent and the second with $\beta = 1$ fits the contrast with a parabola.

As a result the data suggest that the critical exponent lies somewhere close to 0.3 that hints a 3D Ising behaviour.

5.6 Conclusions

To summarize, the growth by high-temperature oxygen assisted molecular beam epitaxy of mixed cobalt-nickel oxide structures on Ru(0001) surface gives rise to the formation of mostly (111) oriented islands. The structures are easily recognized by their triangular shape and they coexist with a few NCO (001) minority orientation rectangular islands. The atomic structure has been characterized with LEEM and μ -LEED confirming the existence of these two orientations. Chemical states of the surface cations (Co^{2+} and Ni^{2+}) have been identified by x-ray absorption spectromicroscopy. We have shown that the growth at high temperature leads to the formation of the mixed nickel-cobalt monoxide phase as expected from the phase diagram. The element-specific XMLD measurements reveal sizeable antiferromagnetic domains at room temperature. Our results demonstrate the possibility to increase the Néel temperature of the $\text{Ni}_x\text{Co}_{1-x}\text{O}$ antiferromagnetic nanostructures well above room-temperature and tune it by adjusting the composition, without involving any additional magnetic layer. No thickness dependence of T_N was found in the range 20 to 80 nm.

5.7 References

- [1] P. Wadley et al. Electrical switching of an antiferromagnet. *Science*, 2016. doi:[10.1126/science.aab1031](https://doi.org/10.1126/science.aab1031).
- [2] M. B. Jungfleisch et al. Perspectives of antiferromagnetic spintronics. *Phys. Lett. A*, 2018. doi:[10.1016/j.physleta.2018.01.008](https://doi.org/10.1016/j.physleta.2018.01.008).
- [3] J. Nogués and I. K. Schuller. Exchange bias. *J. Magn. Magn. Mater.*, 1999. doi:[10.1016/S0304-8853\(98\)00266-2](https://doi.org/10.1016/S0304-8853(98)00266-2).
- [4] S. Baumann et al. Bistability in Atomic-Scale Antiferromagnets. *Science*, 2012. doi:[10.1126/science.1214131](https://doi.org/10.1126/science.1214131).
- [5] T. Kampfrath et al. Coherent terahertz control of antiferromagnetic spin waves. *Nat. Photonics*, 2011. doi:[10.1038/nphoton.2010.259](https://doi.org/10.1038/nphoton.2010.259).
- [6] X. Marti et al. Room-temperature antiferromagnetic memory resistor. *Nat. Mater.*, 2014. doi:<https://doi.org/10.1038/nmat3861>.
- [7] W. Kuch et al. Tuning the magnetic coupling across ultrathin antiferromagnetic films by controlling atomic-scale roughness. *Nat. Mater.*, 2006. doi:[10.1038/nmat1548](https://doi.org/10.1038/nmat1548).
- [8] M. Bode et al. Atomic spin structure of antiferromagnetic domain walls. *Nat. Mater.*, 2006. doi:[10.1038/nmat1646](https://doi.org/10.1038/nmat1646).

-
- [9] I. Sugiyama et al. Ferromagnetic dislocations in antiferromagnetic NiO. *Nat. Nanotechnol.*, 2013. doi:10.1038/nnano.2013.45.
- [10] K. Wang and A. R. Smith. Three-Dimensional Spin Mapping of Antiferromagnetic Nanopyramids Having Spatially Alternating Surface Anisotropy at Room Temperature. *Nano Lett.*, 2012. doi:10.1021/nl204192n.
- [11] D. Alders et al. Temperature and thickness dependence of magnetic moments in NiO epitaxial films. *Phys. Rev. B*, 1998. doi:10.1103/PhysRevB.57.11623.
- [12] M. W. Haverkort et al. Magnetic versus crystal-field linear dichroism in NiO thin films. *Phys. Rev. B*, 2004. doi:10.1103/PhysRevB.69.020408.
- [13] S. I. Csiszar et al. Controlling Orbital Momt and Spin Oritation in CoO Layers by Strain. *Phys. Rev. Lett.*, 2005. doi:10.1103/PhysRevLett.95.187205.
- [14] I. P. Krug et al. Magnetic coupling in highly ordered NiO/Fe₃O₄ (110): Ultrasharp magnetic interfaces vs. long-range magnetoelastic interactions. *EPL*, 2008. doi:10.1209/0295-5075/81/17005.
- [15] H. Ohldag et al. Correlation of crystallographic and magnetic domains at Co/NiO(001) interfaces. *Phys. Rev. B*, 2009. doi:10.1103/PhysRevB.79.052403.
- [16] G. van der Laan et al. Anisotropic x-ray magnetic linear dichroism and spectromicroscopy of interfacial Co/NiO(001). *Phys. Rev. B*, 2011. doi:10.1103/PhysRevB.83.064409.
- [17] Q. Li et al. Antiferromagnetic proximity effect in epitaxial CoO/NiO/MgO(001) systems. *Sci. Rep.*, 2016. doi:10.1038/srep22355.
- [18] K. Heinz and L. Hammer. Epitaxial cobalt oxide films on Ir(100)—the importance of crystallographic analyses. *J. Phys.: Condens. Matter*, 2013. doi:10.1088/0953-8984/25/17/173001.
- [19] A. D. Lamirand et al. Robust perpdcular exchange coupling in an ultrathin CoO/PtFe double layer: Strain and spin oritation. *Phys. Rev. B*, 2013. doi:10.1103/PhysRevB.88.140401.
- [20] L. Martín-García et al. Initial Stages of the Growth of Mixed Iron-Cobalt Oxides on Ru(0001). *Phys. Procedia*, 2016. doi:10.1016/j.phpro.2016.11.075.
- [21] O. Olanipekun et al. Epitaxial growth of cobalt oxide phases on Ru(0001) for spintronic device applications. *Semicond. Sci. Technol.*, 2017. doi:10.1088/1361-6641/aa7c58.

- [22] J. Zhu et al. Antiferromagnetic spin reorientation transition in epitaxial NiO/CoO/MgO(001) systems. *Phys. Rev. B*, 2014. doi:[10.1103/PhysRevB.90.054403](https://doi.org/10.1103/PhysRevB.90.054403).
- [23] P. N. G. Poillerat. Characterization of Spinel-Type Cobalt and Nickel Oxide Thin Films by X-Ray Near Grazing Diffraction, Transmission and Reflectance Spectroscopies, and Cyclic Voltammetry. *J. Electrochem. Soc.*, 1995. doi:[10.1149/1.2044193](https://doi.org/10.1149/1.2044193).
- [24] C. Zhen. et al. Nanostructural origin of semiconductivity and large magnetoresistance in epitaxial $\text{NiCo}_2\text{O}_4/\text{Al}_2\text{O}_3$ thin films. *J. Phys. D: Appl. Phys.*, 2018. doi:[10.1088/1361-6463/aab2a3](https://doi.org/10.1088/1361-6463/aab2a3).
- [25] R. J. Deokate et al. Simple Synthesis of NiCo_2O_4 thin films using Spray Pyrolysis for electrochemical supercapacitor application: A Novel approach. *Electrochim. Acta*, 2017. doi:<https://doi.org/10.1016/j.electacta.2016.12.034>.
- [26] W. L. Roth. Magnetic Structures of MnO, FeO, CoO, and NiO. *Phys. Rev.*, 1958. doi:[10.1103/PhysRev.110.1333](https://doi.org/10.1103/PhysRev.110.1333).
- [27] K. Tomiyasu et al. Magnetic structure of coo studied by neutron and synchrotron x-ray diffraction. *Phys. Rev. B*, 2004. doi:[10.1103/PhysRevB.70.184411](https://doi.org/10.1103/PhysRevB.70.184411).
- [28] W. L. Roth. Multispin Axis Structures for Antiferromagnets. *Phys. Rev.*, 1958. doi:[10.1103/PhysRev.111.772](https://doi.org/10.1103/PhysRev.111.772).
- [29] W. Jauch et al. Crystallographic symmetry and magnetic structure of CoO. *Phys. Rev. B*, 2001. URL: <https://link.aps.org/doi/10.1103/PhysRevB.64.052102>, doi:[10.1103/PhysRevB.64.052102](https://doi.org/10.1103/PhysRevB.64.052102).
- [30] D. C. Khan and R. A. Erickson. Magnetic Form Factor of Co^{2+} Ion in Cobaltous Oxide. *Phys. Rev. B*, 1970. doi:[10.1103/PhysRevB.1.2243](https://doi.org/10.1103/PhysRevB.1.2243).
- [31] L. Han et al. Interrogation of bimetallic particle oxidation in three dimensions at the nanoscale. *Nat. Commun.*, 2016. doi:[0.1038/ncomms13335](https://doi.org/10.1038/ncomms13335).
- [32] M. J. Carey and A. E. Berkowitz. Exchange anisotropy in coupled films of $\text{Ni}_{18}\text{Fe}_{19}$ with NiO and $\text{Co}_x\text{Ni}_{1-x}\text{O}$. *Appl. Phys. Lett.*, 1992. doi:[10.1063/1.106756](https://doi.org/10.1063/1.106756).
- [33] M. Finazzi et al. *Low-Dimensional Antiferromagnetic Oxides: An Overview*, chapter 1, pages 1–23. 2010. doi:[10.1002/9783527630370.ch1](https://doi.org/10.1002/9783527630370.ch1).

- [34] M. Finazzi and S. Altieri. Magnetic dipolar anisotropy in strained antiferromagnetic films. *Phys. Rev. B*, 2003. doi:10.1103/PhysRevB.68.054420.
- [35] A. Schrön et al. Crystalline and magnetic anisotropy of the 3d-transition metal monoxides mno, feo, coo, and nio. *Phys. Rev. B*, 2012. doi:10.1103/PhysRevB.86.115134.
- [36] L. Martín-García et al. Atomically Flat Ultrathin Cobalt Ferrite Islands. *Adv. Mat.*, 2015. URL: <https://onlinelibrary.wiley.com/doi/abs/10.1002/adma.201502799>, doi:10.1002/adma.201502799.
- [37] J. I. Flege et al. Growth and characterization of epitaxially stabilized ceria(001) nanostructures on Ru(0001). *Nanoscale*, 2016. doi:10.1039/C6NR02393B.
- [38] J. Höcker et al. Controlling Heteroepitaxy by Oxygen Chemical Potential: Exclusive Growth of (100) Oriented Ceria Nanostructures on Cu(111). *J. Phys. Chem. C*, 2016. doi:10.1021/acs.jpcc.5b11066.
- [39] J. Stöhr et al. Principles of X-Ray Magnetic Dichroism Spectromicroscopy. *Surf. Rev. Lett.*, 1998. doi:10.1142/S0218625X98001638.
- [40] J. Stöhr and H. C. Siegmann. *Magnetism: From Fundamentals to Nanoscale Dynamics*. Springer Series in Solid-State Sciences. Springer-Verlag, 2006. doi:10.1007/978-3-540-30283-4.
- [41] E. Goering et al. Spin and orbital magnetic moments of Fe₃O₄. *Phys. Rev. Lett.*, 2006. doi:10.1103/PhysRevLett.96.039701.
- [42] E. Goering et al. Magnetic anisotropy of textured CrO₂ thin films investigated by X-ray magnetic circular dichroism. *Appl. Phys. A*, 2002. doi:10.1007/s003390201302.
- [43] T. Kinoshita et al. Antiferromagnetic Domain Structure Imaging of Cleaved NiO(100) Surface Using Nonmagnetic Linear Dichroism at O K Edge: Essential Effect of Antiferromagnetic Crystal Distortion. *J. Phys. Soc. Jpn.*, 2004. doi:10.1143/JPSJ.73.2932.
- [44] J. Stöhr et al. Images of the antiferromagnetic structure of a nio(100) surface by means of x-ray magnetic linear dichroism spectromicroscopy. *Phys. Rev. Lett.*, 1999. doi:10.1103/PhysRevLett.83.1862.
- [45] G. van der Laan. Magnetic linear x-ray dichroism as a probe of the magnetocrystalline anisotropy. *Phys. Rev. Lett.*, 1999. doi:10.1103/PhysRevLett.82.640.
- [46] C. Baldasseroni et al. Temperature-driven growth of antiferromagnetic domains

- in thin-film FeRh. *J. Phys.: Condens. Matter*, 2015. doi:[10.1088/0953-8984/27/25/256001](https://doi.org/10.1088/0953-8984/27/25/256001).
- [47] K. S. R. Mon et al. Surface antiferromagnetic domain imaging using low-ergy unpolarized electrons. *Phys. Rev. B*, 2011. doi:[10.1103/PhysRevB.84.132402](https://doi.org/10.1103/PhysRevB.84.132402).
- [48] J. Wu et al. Direct Measurement of Rotatable and Frozen CoO Spins in Exchange Bias System of CoO/Fe/Ag(001). *Phys. Rev. Lett.*, 2010. doi:[10.1103/PhysRevLett.104.217204](https://doi.org/10.1103/PhysRevLett.104.217204).
- [49] G. Fischer et al. Exchange coupling in transition metal monoxides: Electronic structure calculations. *Phys. Rev. B*, 2009. doi:[10.1103/PhysRevB.80.014408](https://doi.org/10.1103/PhysRevB.80.014408).
- [50] A. E. Berkowitz and K. Takano. Exchange anisotropy — a review. *J. Magn. Magn. Mater.*, 1999. doi:[https://doi.org/10.1016/S0304-8853\(99\)00453-9](https://doi.org/10.1016/S0304-8853(99)00453-9).
- [51] P. J. van der Zaag et al. Difference between Blocking and Néel Temperatures in the Exchange Biased $\text{Fe}_3\text{O}_4/\text{CoO}$ System. *Phys. Rev. Lett.*, 2000. doi:[10.1103/PhysRevLett.84.6102](https://doi.org/10.1103/PhysRevLett.84.6102).
- [52] T. Ambrose and C. L. Chien. Finite-Size Effects and Uncompensated Magnetization in Thin Antiferromagnetic CoO Layers. *Phys. Rev. Lett.*, 1996. doi:[10.1103/PhysRevLett.76.1743](https://doi.org/10.1103/PhysRevLett.76.1743).
- [53] M. Molina-Ruiz et al. Evidence of finite-size effect on the Néel temperature in ultrathin layers of CoO nanograins. *Phys. Rev. B*, 2011. doi:[10.1103/PhysRevB.83.140407](https://doi.org/10.1103/PhysRevB.83.140407).
- [54] B. T. Thole et al. Strong magnetic dichroism predicted in the $M_{4,5}$ x-ray absorption spectra of magnetic rare-earth materials. *Phys. Rev. Lett.*, 1985. doi:[10.1103/PhysRevLett.55.2086](https://doi.org/10.1103/PhysRevLett.55.2086).
- [55] D. L. Mills. Surface effects in magnetic crystals near the ordering temperature. *Phys. Rev. B*, 1971. doi:[10.1103/PhysRevB.3.3887](https://doi.org/10.1103/PhysRevB.3.3887).

6 Fe-doped nickel oxide Fe-NiO

In this Chapter we demonstrate the route for the preparation of high-quality Fe-doped nickel oxide thin films supported on a metallic substrate. The nucleation and the growth process are followed in-situ by LEEM. A comprehensive structural and chemical characterization is performed combining LEEM/LEED with synchrotron based Photoemission Electron Microscopy.

6.1 Introduction

As it was already mentioned, in recent years the significance of antiferromagnetism for practical applications has been continuously increasing[1–5]. The absence of net magnetization makes antiferromagnetic (AF) materials important candidates for extremely rapid spin manipulation and switching since there is no change in angular momentum associated to it. One of the most promising antiferromagnetic compounds for device applications is NiO. Recently it has been shown that a thin layer of nickel oxide can be used in spintronic devices to transport a spin current between two layers or to generate radiation with THz frequency in spin-torque nano-oscillators[6–9].

Nickel oxide is a prototypical room temperature antiferromagnetic insulator. It belongs to the group of $3d$ binary transition metal oxides whose properties are being studied extensively. Above its Néel temperature ($T_N = 523$ K), nickel oxide possess a simple crystallographic structure (cubic structure of rocksalt)[10; 11]. Below T_N the magnetic order is accompanied by a small rhombohedral distortion (a fraction of 1%) in the $[111]$ direction[12]. In various macroscopic regions of the crystal, any one of the four possible directions of type $\langle 111 \rangle$ can become the axis of the rhombohedral distortion. These structural domains, each of which contains its own $\{111\}$ -type plane, perpendicular to the corresponding rhombohedral distortion, bear the name of twin domains (T)[13].

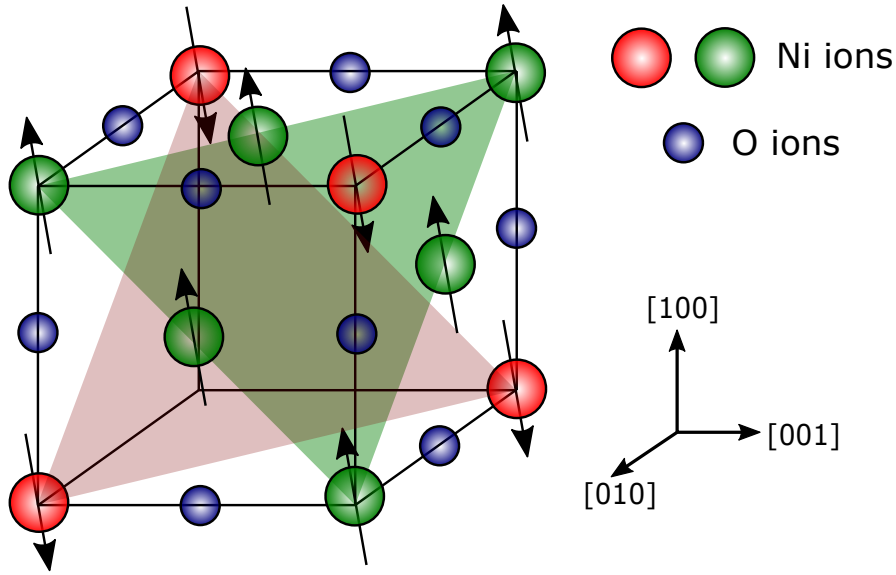


Figure 6.1: Schematic illustration of AF spin ordering in nickel oxide. The green and red circles and planes indicate Ni^{2+} ions with spin up and down, respectively. The spin directions lies along $[11\bar{2}]$ and are coupled ferromagnetically within the same $\{111\}$ plane.

The spins of Ni^{2+} cations are ordered ferromagnetically along $[11\bar{2}]$ direction inside a single plane and alternating $\{111\}$ planes are antiferromagnetically ordered. Each of the three $[11\bar{2}]$ spin directions per T domain defines a "spin domain" (S). This results in a total of 12 orientational domains. This type of antiferromagnetic ordering is usually denoted as type-II AF order[14].

S	T			
	$T_1 [111]$	$T_2 [11\bar{1}]$	$T_3 [1\bar{1}1]$	$T_4 [\bar{1}11]$
S_1	$[11\bar{2}]$	$[112]$	$[121]$	$[211]$
S_2	$[\bar{2}11]$	$[121]$	$[\bar{2}11]$	$[\bar{1}1\bar{2}]$
S_3	$[1\bar{2}1]$	$[211]$	$[112]$	$[121]$

Table 6.1: Crystallographic directions of the Spin and Twin domains of NiO[15].

In the previous chapter, it was already explained that the anisotropy in NiO is provided by dipole-dipole interaction, and it favours a collinear alignment between the sublattices. However, in a thin film form, the anisotropy depends on the particular combination of strain ($\epsilon = \frac{c}{a} - 1$, c and a are the out-of-plane and in-plane lattice parameters, respectively) and thickness, that can substantially change the spin direction of spin domains. For example, for tetragonally strained NiO films

on Ag(001) ($\epsilon < 0$ - compression), the strain result in a preferred S-domain with main spin component perpendicular to the strain axis, while for NiO/MgO(001) ($\epsilon > 0$ - expansion) the spin arrangement is parallel to the strain axis. In uniformly strained AF films the in-plane anisotropy, which stabilizes the S-domains in the surface plane, arises from the strain and reduced film thickness that sum up to the total dipolar anisotropy[16]. At variance with the well known shape anisotropy in ferromagnetic thin films, which scales with the film volume, the AF "shape" anisotropy is proportional to τ^{-1} (where τ is a finite film thickness)[17].

The unique properties of NiO are especially evident in systems of reduced dimensionality, as pointed out in many studies. However, the growth of NiO films is not straightforward. It requires the control at the atomic scale (chemical and structural) of the growth process. As a consequence, a lot of effort has been directed to the fabrication and study of nickel oxide films on different substrates. One monolayer thick nickel oxide films prepared by standard O₂-based reactive deposition on various metallic (Ag, Au, Pd, Pt and vicinal Rh) and insulating (MgO) surfaces are the most studied systems[10; 18–24].

Nevertheless, for a simple rocksalt monoxide as NiO is, controlling and understanding the growth details often remains a challenge. In many cases the most important properties such as magnetic order, ordering temperature or magnetic moments were found to depend on the stoichiometry, defect content or morphology of the films, in turn mostly determined by the preparation method. Films deposited on metal substrates by oxygen reactive deposition typically display a very puzzling growth behaviour characterized by complex atomic reconstructions, nonuniform thickness and/or multiple oxidation states that drastically change with the growth parameters (oxygen partial pressure, substrate temperature or deposition rate).

6.2 Growth of nickel oxide thin films

6.2.1 Growth at different substrate temperature

For this thesis we have been trying to growth nickel oxide films on Ru(0001) by using high-temperature oxygen-assisted molecular beam epitaxy (under an O₂ atmosphere of 10⁻⁶ mbar) varying the substrate temperature (in the range 950 K to RT). The results are similar to those already obtained for other metals[18–21], as summarized in the LEEM images and corresponding LEED patterns of Figure 6.2.

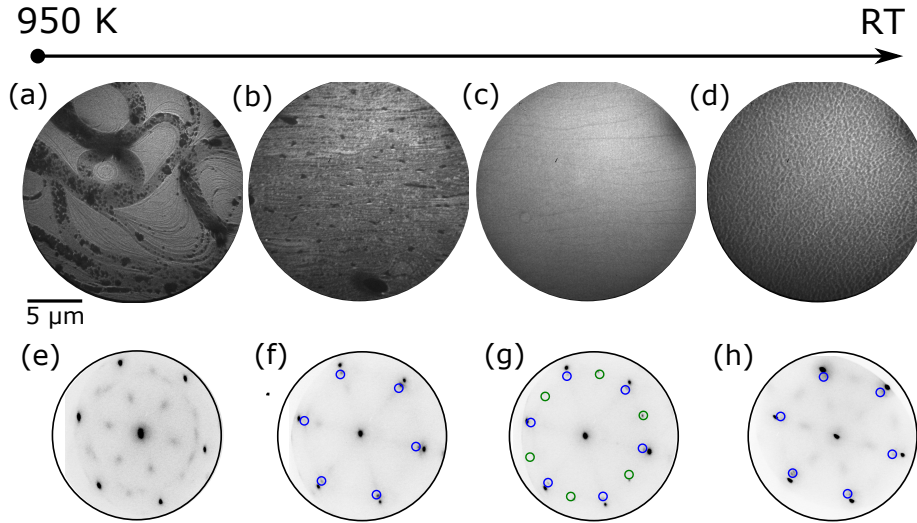


Figure 6.2: LEEM images and corresponding LEED patterns of NiO structures grown on Ru(0001) at different substrate temperatures (a) and (e) $T_{Ru} = 950$ K, (b) and (f) $T_{Ru} = 680$ K, (c) and (g) $T_{Ru} = 500$ K, (d) and (h) $T_{Ru} = 300$ K.

We have found that the substrate temperature does not influence drastically the growth process. In all cases, (Figure 6.2) the growth results in small islands formation, randomly distributed on the sample. Additionally low energy electron diffraction (LEED) patterns were acquired to provide information about the surface structure of each film. Typical LEED patterns shown in Figure 6.2e–h reveal several sets of hexagonal patterns. The brightest spots correspond to Ru 1st order diffracted beams. While the structures grown on Ru give rise to less intense hexagonal pattern (marked by blue circles in Figure 6.2. By comparing the spacing of the first order diffracted spots of hexagonal pattern with those of Ru substrate, they are found to correspond to a distance of 0.305 nm which is comparable with the in-plane lattice spacing of perfectly stoichiometric NiO (0.3 nm). In some cases additional rotated hexagonal patterns are formed, as well as a 2x2 reconstruction, possibly stemming from the O-covered Ru surface.

In order to obtain the surface morphology *ex-situ* Atomic Force Microscopy (AFM) measurements have been done by C. Ocal and co-workers. The AFM images for NiO film grown on ruthenium at 500 K are shown in Figure 6.3. It displays small, grainy islands (a few nm wide) distributed along the Ru atomic steps. This kind of structures cannot be observed in LEEM due to the lateral resolution of the microscope (10 nm).

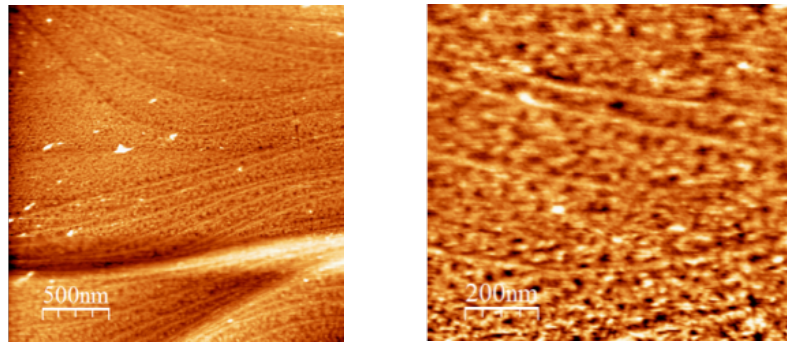


Figure 6.3: AFM images of NiO films grown by MBE at $T=500$ K on Ru(0001) substrate.

In summary, the islands of NiO grown on Ru even at high substrate temperatures, are very small. We now describe a way around this limitation, based on the addition of small amounts of iron in order to modify the growth mode.

6.2.2 Effect of Fe doping on the growth of NiO films on Ru(0001)

It was already reported in the literature that the structure of non-stoichiometric nickel oxide can act as an inert matrix for iron[25–27]. Due to this fact, iron doped nickel oxide create is a stable phase with a cubic rocksalt structure, in good agreement with the phase diagram of Ni-Fe-O (presented in Chapter 4, Figure 4.10), where the (Ni/Fe)O phase should be stable.

Thus we have tested the following strategy in order to grow large NiO islands: the co-deposition of Fe and Ni (the dosing rate was adjusted to obtain small content of Fe of a few %) on a Ru crystal at elevated temperature (1150 K) and oxygen atmosphere (10^{-6} mbar). Figure 6.4 presents selected frames acquired during the growth process.

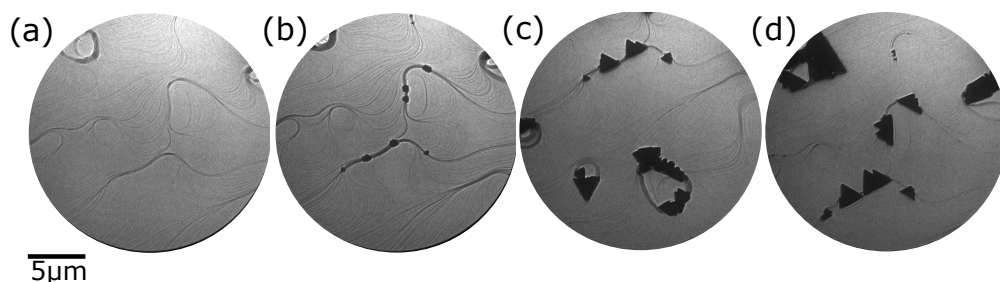


Figure 6.4: Selected frames from a sequence of LEEM images acquired during the growth of Fe-doped NiO (ratio Ni:Fe 15:1) at 1150 K and at a background pressure of 1×10^{-6} mbar of molecular oxygen. The frames correspond to (a) 0 sec, (b) 8 min, (c) 35 min and (d) 60 min after opening the doser shutters. The electron energy is 5 eV. Notice that the imaged region is not identical in all images since thermal drift is unavoidable at the used temperatures.

A substantial modification of the film growth mode requires an appreciable change in the balance of surface and interface free energies. Thus, in the following we opted for introducing an additional element in order to adjust the growth mode. Figure 6.4 presents selected frames acquired during the growth process of Fe-doped NiO. We deposit nickel and iron on Ru(0001) at elevated temperature (1150 K) while exposing to molecular oxygen. As a first step the bare substrate is exposed to molecular oxygen which adsorbs on the Ru crystal forming a 2D atomic oxygen gas and increasing the work function of Ru around 0.8 eV. A LEEM image of the substrate just after opening the shutters is shown in Figure 6.4b. Many nuclei decorate the step bunches around large atomic terraces and further grow forming μm -sized triangular 3-dimensional but flat islands (Figure 6.4c–d). It was already shown previously that the growth of mixed nickel-cobalt oxides on Ru(0001) follows the same growth mode - Volmer-Weber, where starting from single nuclei 3-dimensional islands grow. As in the case of NiFe_2O_4 or $\text{Ni}_x\text{Co}_{1-x}\text{O}$, iron doped nickel oxide islands present a triangular shape with two opposite orientations. Additionally, some triangular islands rotated 30° were found.

By comparing the data shown in Figure 6.2 with 6.4 we can see the drastic change in the growth when adding a small amount of Fe to act as a surfactant. Instead of small, grainy islands we observed that iron content promote three dimensional growth[28].

A small amount of Fe added during the growth process, thus flattens the films and leads to the formation of several μm wide islands, with much bigger structural and magnetic domains, as will be shown later. Thus, we can conclude that iron atoms behave in some way as a surfactant that changes the balance of surface and interface free energy of the overlayer[28].

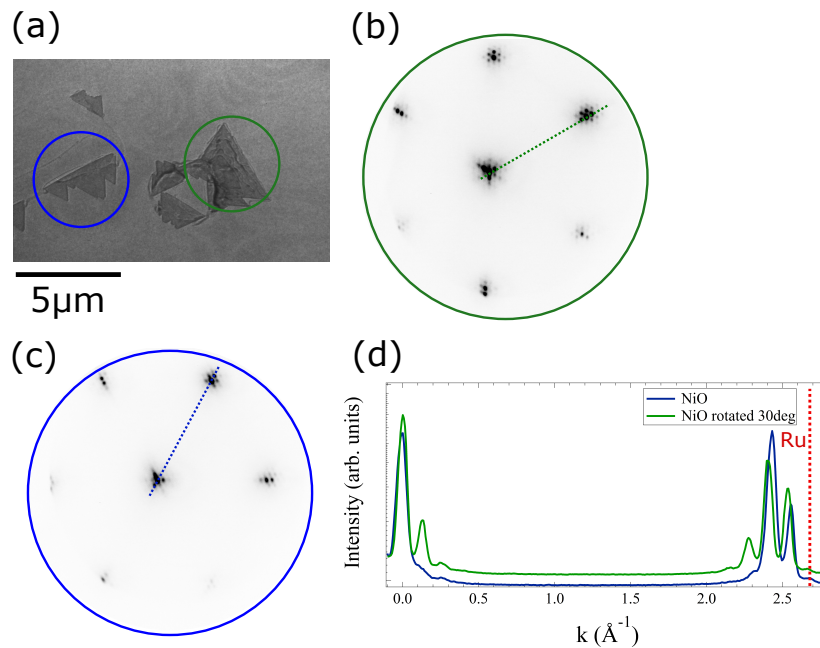


Figure 6.5: LEEM image (a) and corresponding LEED patterns at 45 eV electron energy from two different islands on the sample (b) non-rotated, (c) rotated 30°. (d) Cross sectional cuts along the cuts indicated by dash lines in (b) and (c). The red dash line indicates the Ru first order spots distance, for reference.

The surface structure was studied by microspot low-energy electron diffraction. An area selected for LEED measurement is shown in Figure ??a. We have found two types of triangular islands rotated 30° relative to each other. The diffraction patterns of each island type are presented in Figure ??b-c. The two islands marked in Figure ??a present hexagonal patterns aligned (blue) with the Ru(0001) lattice and rotated (green) by 30°, respectively. The additional closely spaced satellite spots are similar to those observed for nickel ferrite[29] or magnetite[?], arising from the so-called bi-phase reconstruction. Based on the LEED pattern we can estimate the lattice spacing for each island type. The lattice spacing for the island aligned with the Ru (0001) is 0.295 ± 0.1 nm, slightly larger than the ruthenium one (0.27 nm) while the reconstruction corresponds to a periodicity of 5.2 ± 0.1 nm. The rotated hexagonal pattern and related reconstruction show slightly larger atomic distances 0.31 ± 0.1 nm and 5.5 ± 0.1 nm, respectively. Cross sectional cuts along the satellite spots at the (b) non-rotated (blue) and (c) rotated island (green), compared to the ruthenium spot distance (red dashed line) are shown in Figure ??d. The difference in the lattice spacing between both islands can be estimated from the cross-sectional profiles. The in-plane lattice spacing for the (111)-oriented rock-salt phase should be 0.29 nm for bulk NiO, in good agreement with the observed values. Thus, we identify the triangular islands as NiO in (111) orientation.

In the case of the rotated island, the Ni atoms are aligned along the direction that joins two in-plane, second nearest neighbours of Ru ($\overline{1\bar{2}1}$). The bulk value for this second nearest neighbours is 0.467 nm. Thus the mismatch is much larger in this case. Nevertheless, it is accommodated by a similar atomic arrangement resulting in superstructure with a similar periodicity, although the growth along the Ru axes is strongly favoured, (we have found that rotated islands make up only 5% of the total amount).

The thickness of islands can be estimated measuring the shadows observed in the XPEEM images. Such images are acquired by collecting secondary electrons emitted by the sample upon photon irradiation. The photons are impinging on the sample at a polar angle 16° . Thus if the islands are thick enough they will create a shadow when photons are tuned to an absorption edge. In the case of the island shown in Figure ??a, the average height is around 25 nm.

6.3 Chemical and magnetic properties

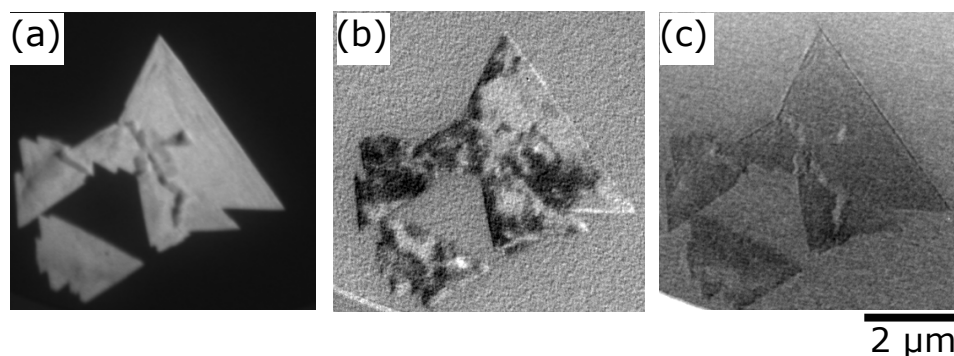


Figure 6.6: (a) XAS-PEEM image of Fe-doped NiO islands on Ru(0001) acquired at the Ni L_2 edge. (b) XMLD-PEEM at the same edge and (c) XLD-PEEM image at the O K edge.

To determine the chemical and magnetic properties of the Fe-doped nickel oxide films we have acquired polarization dependent XAS-PEEM image stacks. XAS images at the Ni, Fe - L_3 , L_2 and O K edges are extracted from selected areas on the surface presented in Figure 7.4b, d, f. The spectra are acquired for both linear horizontal ($\theta = 0^\circ$) and vertical ($\theta = 74^\circ$) polarizations (where θ is the angle between the surface and the electric field vector of the incoming photons). The difference, named XLD (X-ray Linear Dichroism) measures the charge anisotropy related to both local crystal field and local exchange field (via spin-orbit coupling). In the latter case it is termed X-ray Magnetic Linear Dichroism (XMLD).

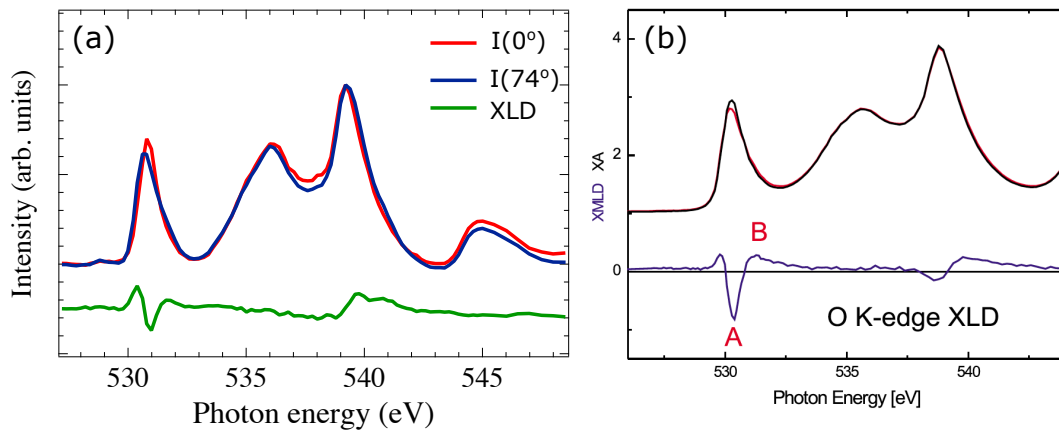


Figure 6.7: (a) O K-edge XAS spectra together with the difference signal (XLD) acquired at the dark region of island shown in Figure 6.6b. (b) For comparison O K-edge spectra from a clean NiO(001) surface. Reprinted from [30].

The local O K-edge XAS spectra for both polarizations together with the difference signals are shown in Figure 6.7a. The oxygen XAS spectrum is the same as the one obtained from a clean NiO(001) surface[30]. It has a characteristic three peak structure, and the dichroic spectrum shows a substantial signal at a photon energy around 531 eV[30]. In the NiO crystal, each O atom is surrounded by six Ni atoms. The direction of the magnetic moments of three of the Ni atoms is opposite to that of the other three, so that the oxygen atoms in NiO crystal should not have any net magnetic moment. Thus, the signal observed at the O dichroic spectra is not due to any magnetic effect but rather it is caused by the crystal distortion and allows to study the structural domains distribution (T-domains)[31]. In Fe-doped NiO films the observed XLD contrast at the O edge is very weak (Figure 6.7b) which can be explained by taking into account that the rhombohedral distortion in the NiO crystal is along the $\langle 111 \rangle$ AF ordering direction, i.e., perpendicular to our films.

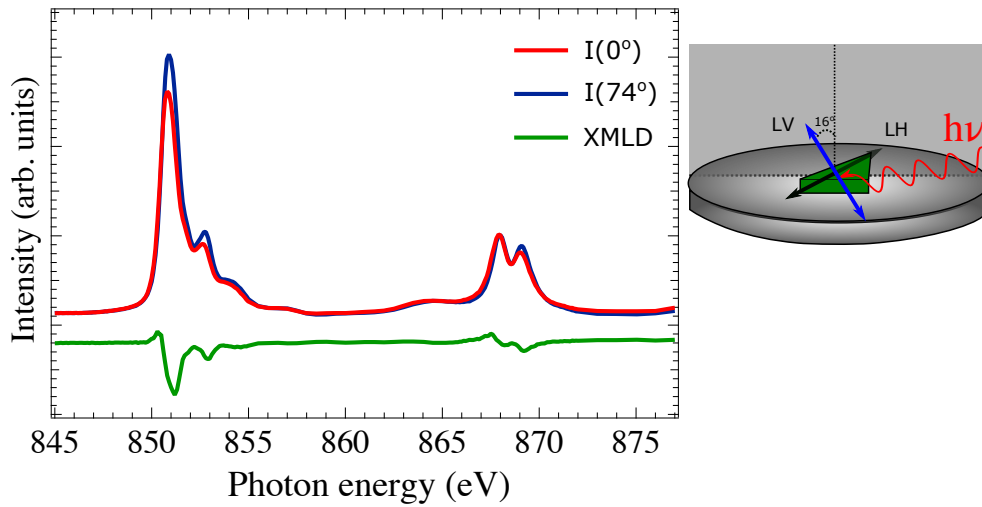


Figure 6.8: Ni L-edge XAS spectra together with the difference signal (XMLD) acquired at the island shown in Figure 6.6. In the right panel a relative orientation of polarization and sample for vertical and horizontal polarization.

The Ni $L_{3,2}$ spectra are presented in Figure 6.8. They present a typical double-peak structure at both L_3 and L_2 edges, characteristic for Ni^{2+} in an octahedral crystal field[10; 32]. The XMLD spectrum measured as the difference between two local absorption spectra from a single domain area with linear horizontal and vertical x-ray polarization presents a significant dichroic signal at both edges. The general line shape of the spectra is similar to that of pure NiO films and of bulk NiO[32].

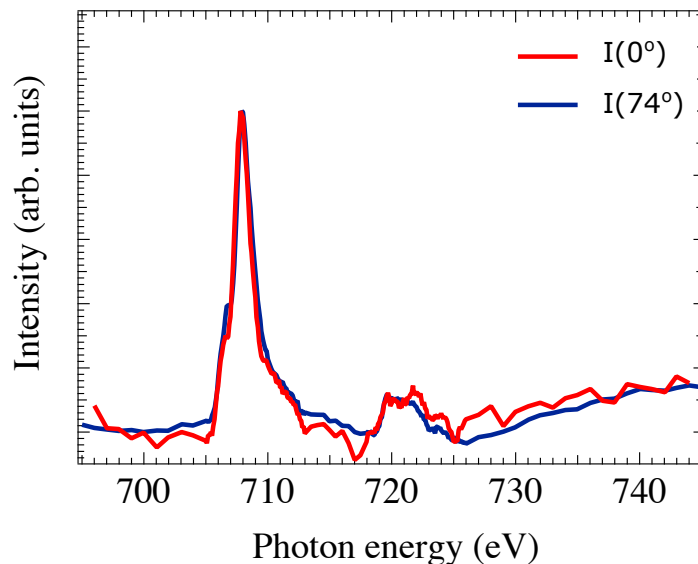


Figure 6.9: (a) Fe L-edge XAS spectra together acquired at the island shown in Figure 6.6.

The XAS spectra at the Fe L-edge (Figure 6.9) are similar to the ones observed for FeO with a small shoulder at the L_3 edge. However, the small Fe amount results in spectra too noisy for the unambiguous detection of a dichroic signal from a single domain[33].

According to the XAS spectra, the chemical identity of the islands is confirmed to be $\text{Fe}_x\text{Ni}_{1-x}\text{O}$. In order to estimate the ratio between Ni and Fe we have measured the edge jump of the XAS spectra, which is proportional to the number of absorbing atoms and linear absorption coefficient. The absorption coefficient for both elements (at the L_3 peak) is similar. By direct comparison of the edge jump intensities at the Ni and Fe XAS spectra, a Ni:Fe ratio close to 15:1 is found. Thus, the islands contain about 5% iron. The error in this estimation is around 10%.

6.4 Magnetism in Fe-doped nickel oxide films

6.4.1 Ruling out the crystal field dichroism

It was already discussed in section 3.3.3 that if the symmetry of the material is exactly cubic no crystal field dichroism will occur, and thus any dichroic contrast observed is due to the magnetic order of the material. However, an epitaxial film grown on a substrate with some lattice mismatch will usually present some distortion (strain). Once the crystal symmetry is lowered, the formerly degenerated orbitals of e_g level split into two states a_1 (d_{z^2} orbital) and b_1 ($d_{x^2-y^2}$ orbital), while the t_{2g} orbitals splits into two degenerate e (d_{xz} , d_{yz}) and b_2 (d_{xy}). This energy splitting will result in an energy shift at the Ni L-edge, between spectra acquired with linear horizontal and vertical polarization[34; 35].

One way to probe whether the observed dichroic signal (Figure 6.6) is due to anti-ferromagnetic ordering or crystal-field effect, is to compare the energy of the main L_3 component for both linear horizontal and vertical photon polarizations[34]. It was already proven both experimentally and theoretically that 1 monolayer thick NiO film on MgO presents strong dichroism at room temperature[34]. However, detailed analysis revealed that the dichroism is not due to the presence of some form of magnetic order, but entirely to crystal field effect[36]. In order to rule out the latter contribution we have checked the Ni L_3 white lines position between $\theta = 0^\circ$ and $\theta = 74^\circ$ for the two types of islands found on the sample. Close ups of this region for both types of island are shown in Figure 5.12. Within the experimental resolution (0.08 eV) no shift is observed, which is an indication that rather than a crystal field effect, the contrast observed in the XMLD PEEM images is antiferromagnetic.

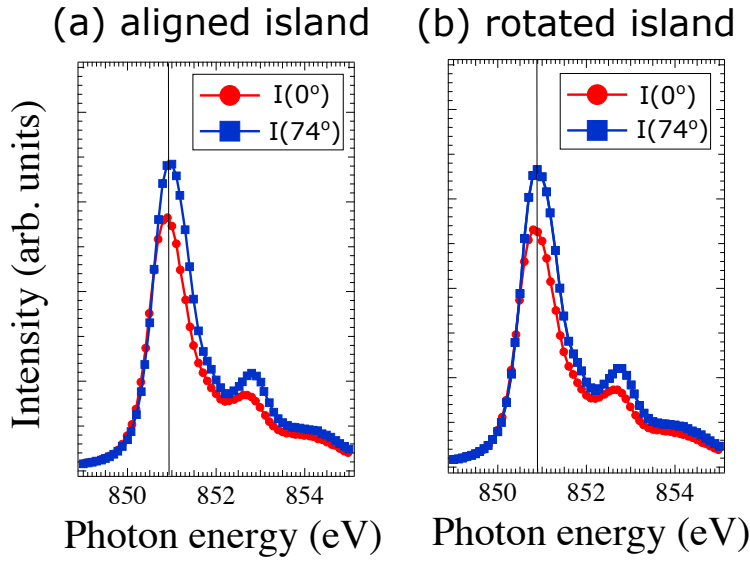


Figure 6.10: Experimental polarization dependent L_3 XAS spectra from a single domain area acquired at both types of triangular islands.

6.4.2 Determination of the spin direction

It has been recently shown that the linear dichroism in the general case does not only depend on the direction of the x-ray polarization with respect to the spin direction but also on the direction of the spin with respect to the crystal axes[32; 35]. This is very important for magnetic domain studies by means of the XMLD-PEEM technique. Hence, in this section we will summarize how to extract the spin direction in an antiferromagnet, following Haverkort *et al.*[37].

To extract the information about the spin-axis orientation in the Fe-doped NiO films, we exploited the XMLD at the Ni L_2 edge, calculating the L_2 peak ratio, as the intensity of the low-energy peak (A) divided by the intensity of the high-energy (B) peak $R = I(A)/I(B)$, after subtraction of a linear background[36]. The spectra of the NiO L_2 peak were acquired at both linear horizontal and vertical polarizations at different azimuthal angle ($\phi = 0 - 180^\circ$, where $\phi = 0^\circ$ defines the direction when the incoming photon beam is parallel to the triangular island edge and hence parallel to the $[1\bar{1}0]$ direction), for a given domain set of the non-rotated islands. The schematic illustration of the experimental geometry is shown in Figure 6.11.

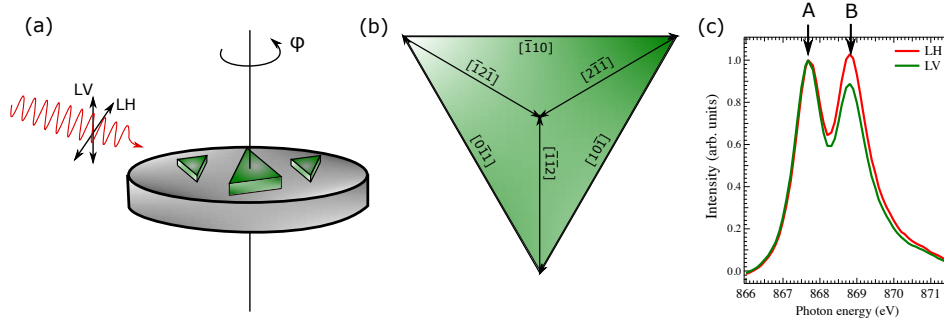


Figure 6.11: (a) Schematic illustration of the experimental geometry. (b) (111) plane with the crystallographic directions marked. (c) NiO L_2 microspectra acquired with linear horizontal and vertical polarization.

Since the XMLD is anisotropic, the contrast obtained from the L_2 double peak ratio cannot be described by the simple relationship:

$$I_{XMLD} = A + B\{3\cos^2(\angle E, S) - 1\} \quad (6.1)$$

where A represents the isotropic part and B the angular part of the spectrum. This formula is only applicable if and only if the crystal symmetry is spherical, or the sum over all magnetic domains yields rotational symmetry with respect to a high symmetry C_4 or C_3 axis, or if the spin axis points along an axis of C_3 symmetry. In the general case, a complicated dependence of the XAS shape on the orientation of S and E with respect to the crystal lattice will result. For Fe-NiO, we have to deal with O_h symmetry since the islands are crystalline, cubic with uniform orientation.

In order to understand the domains distribution in our in-situ grown Fe-NiO films we will compare our experimental contrast with the theoretical one, derived from the model described in detail in section 3.3.4. According to that model an x-ray absorption spectrum for arbitrary polarization E and spin direction S can be calculated using the equation 3.9. The XMLD in NiO is anisotropic, so the dielectric tensor takes the form of Eq. 3.19 with (x, y, z) being the unity spin vector. What we additionally need are the two fundamental spectra ϵ_{\parallel} and ϵ_{\perp} . The spectra ϵ_{\parallel} and ϵ_{\perp} are the XAS spectra measured for the high symmetry cases: ϵ_{\parallel} is the XAS spectrum for $S \parallel E \parallel C_4^z$ and ϵ_{\perp} is the XAS spectrum measured for $C_4^x \parallel S \perp E \parallel C_4^z$ ¹. In order to find two fundamental spectra for a given geometry we have performed ligand field multiplet calculations by using the software Crispy[38]. In Figure 6.12 the fundamental spectra calculated for room temperature are shown. The spectra enter the dielectric tensor, which thus becomes dependent on the photon energy[39]. Thus, by calculating the x-ray absorption at energies A and B of the NiO L_2 edge, the L_2 ratio for all possible orientations of the spin for a given photon polarization, can be derived.

¹The C_4 direction is one of the fourfold high-symmetry directions given by the point group and they are assumed to be x, y, z directions.

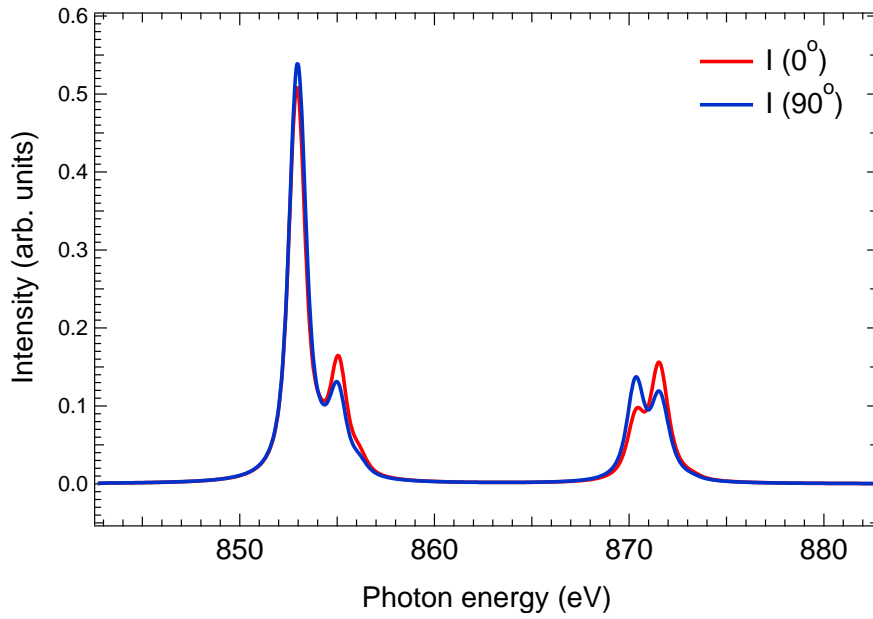


Figure 6.12: Fundamental spectra calculated for 300 K for the high symmetry two cases $S||E||C_4^z$ ($I(0^\circ)$) and $C_4^x||S\perp E||C_4^z$ ($I(90^\circ)$). From these two spectra, it is possible to compute XAS spectra for arbitrary orientations of S and E.

Having discussed the necessary prerequisites for a detailed interpretation of the magnetic contrast, we will turn to the experimental results. We will divide our consideration for two parts, as each type of islands found on the substrate require a special attention.

Aligned islands

In Figure 6.13a–b, the experimental XMLD-PEEM images of the islands aligned with the Ru axes are shown. The images were calculated by the standard method as the ratio of A/B peak intensities of the Ni L_2 edge with linearly polarized light both horizontal (LH) and vertical (LV). It can be noticed from the XMLD images that there is a strong contrast at the images acquired with horizontal polarization, while in the vertical case the contrast is limited. This is nicely reflected on the microspectra (Figure 6.13c–d) acquired from the single domain areas marked in panels (a) and (b). For example in the PEEM image for LH, the D1 domain showing a high L_2 ratio of 1.24 is considerably stronger than at the images acquired with vertical polarization where the ratio is close to 1. Thus, a strong dichroic contrast is observed in the surface plane.

In order to find the spin-axis within each island, we have compared the experimental XMLD contrast for both photon polarizations to the theoretical spectra. The L_2 ratio for example for LH geometry is calculated for a given spin direction (e.g. NiO bulk spin-axis) by rotating the E-vector around an arbitrary direction. In our case we rotate the E-vector around the $[111]$ direction as we have (111) -oriented islands.

In Figure 6.13g–h the theoretical L_2 ratio for LH and LV polarized geometry is plotted. It is immediately clear that the simple $\cos(\mathbf{E}, \mathbf{S})$ -dependence is not valid in the general case.

It can be seen that the L_2 ratio calculated for one of the bulk NiO spin axis $[\bar{1}2\bar{1}]$ is in good agreement with the data obtained experimentally: both the overall shape of the L_2 ratio vs azimuthal angle and the ratio values are in close agreement. For the LV contrast, the outcome analysis is similar. The L_2 ratio found experimentally is close to 1 which indicates reduced dichroism. The same values were found theoretically. Hence, it can be finally concluded that the spin axes of the Fe-doped NiO islands is preferentially oriented in the (111) plane, along the $[\bar{1}2\bar{1}]$ directions of bulk NiO.

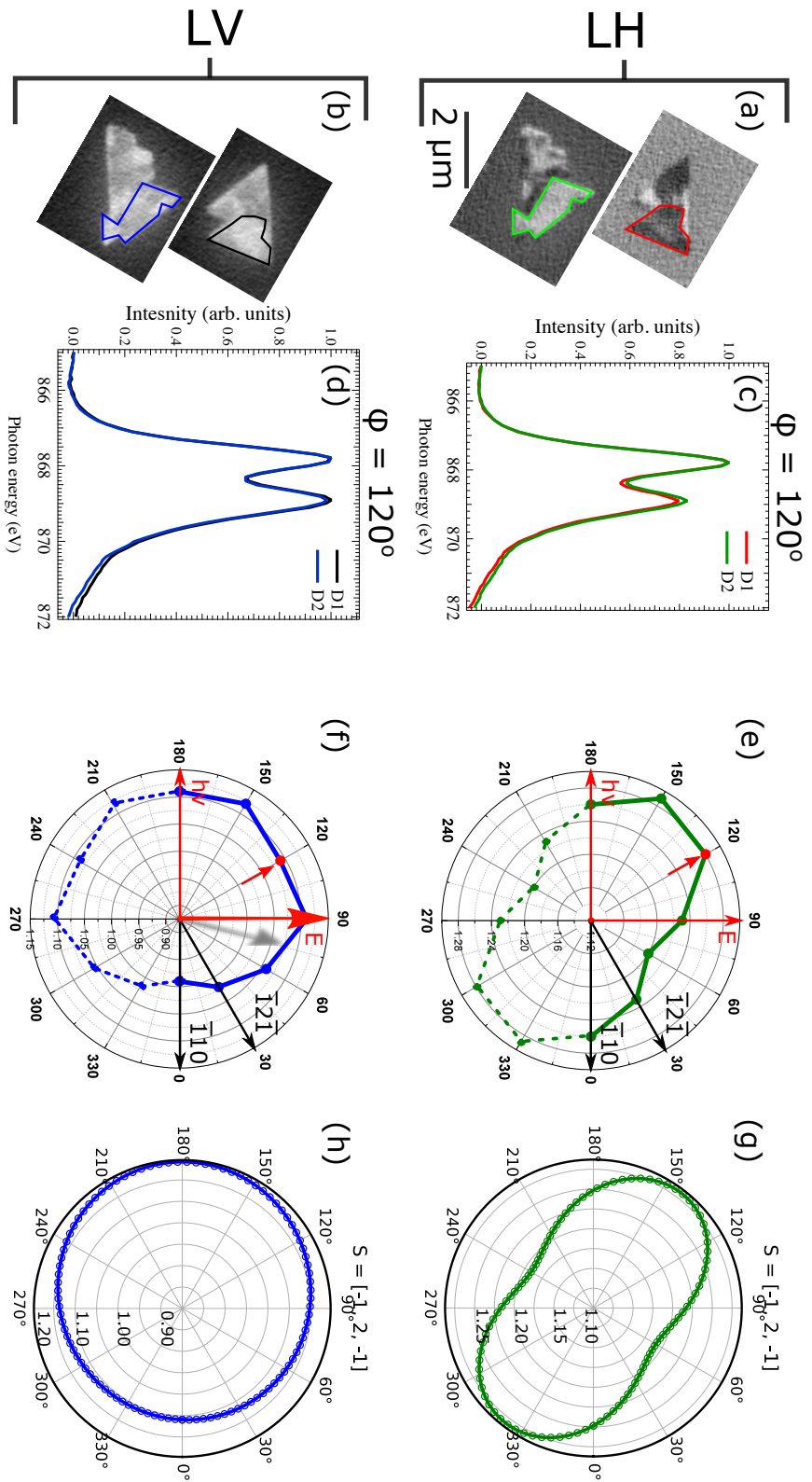


Figure 6.13: Experimental XMCD PEEM images obtained with linear (a) horizontal and (b) vertical photon polarization. Panels (c) and (d) show the respective microspectra within the different domain set marked in colors in panel (a) and (b). Polar plots with the experimental L_2 ratio for all the possible directions within (111) plane acquired with linear (e) horizontal and (f) vertical polarization. (g) and (h) show the calculated L_2 ratio for the given spin vector in the (111) plane and out-of-plane.

Rotated islands

The same analysis has been performed for the islands rotated 30° with respect to the Ru crystal close-packed directions. The XMLD images acquired at horizontal and vertical linear polarizations are shown in panel (a) in Figures 6.14, and 6.15, respectively.

We will first consider the LH geometry. We have chosen two regions on the sample (marked in colors), where the XMLD contrast is different. The region marked in green (D3) presents strong dichroic contrast, while the one in red (D4) has negligible dichroism. From each region we have acquired the L_2 edge spectra at different azimuthal angles ϕ (Figure 6.14c-d). Note that the XMLD contrast variation for D3 with respect to the D4 suggests that the spin-axis of both domains point in different directions. We calculated the theoretical value of L_2 , for extremal spin-axis orientations with respect to the rotation plane (111), i.e. parallel or perpendicular and found that the best agreement with our experimental data is achieved when the spin-axis of D3 lies in-plane, in the $[\bar{1}\bar{1}2]$ direction, whereas for D4 it is pointed along the $[\bar{1}11]$ direction, which is tilted about 70° with respect to the (111) plane.

In the XMLD images acquired with vertical photon polarization (Figure 6.15a), it can be noticed that the D3 and D4 domains have reversed contrast with respect to the images with horizontal polarization. Domain D3 marked in blue presents a gray contrast with the value of L_2 ratio close to 1, while domain D4 with high L_2 ratio (1.14) is considerably brighter. This strong contrast observed with vertical photon polarization gives another hint that the spin-axis actually points along one of the out-of-plane directions. To check the validity of this observation we have calculated the value of L_2 ratio for vertical geometry for the spin-axis previously used. Our findings are in a good agreement with the experimental results and hence confirm that the rotated island hosts two sets of domains: in-plane pointing along $[\bar{1}\bar{1}2]$ and out-of-plane along $[\bar{1}11]$ directions.

On the one hand the existence of long-range antiferromagnetic ordering in the surface plane with $\{\bar{1}\bar{1}2\}$ spin direction shows that in our in-situ grown Fe-doped NiO films the spin-axis is the same as for bulk NiO. But on the other hand for rotated islands we also find domains with a different spin direction, including an out-of-plane component. The exact origin of the additional out-of-plane contrast is not totally clear. We could relate the observed $[\bar{1}11]$ direction to one of the twin domains in NiO. But then we should observe the same contrast at the oxygen K edge, which is not the case. In addition, strain could play a role in the rotated islands, which present an in-plane lattice constant larger than that of bulk NiO by almost 7%. Further work is necessary in order to fully understand the origin of the spin axis in the rotated islands[40].

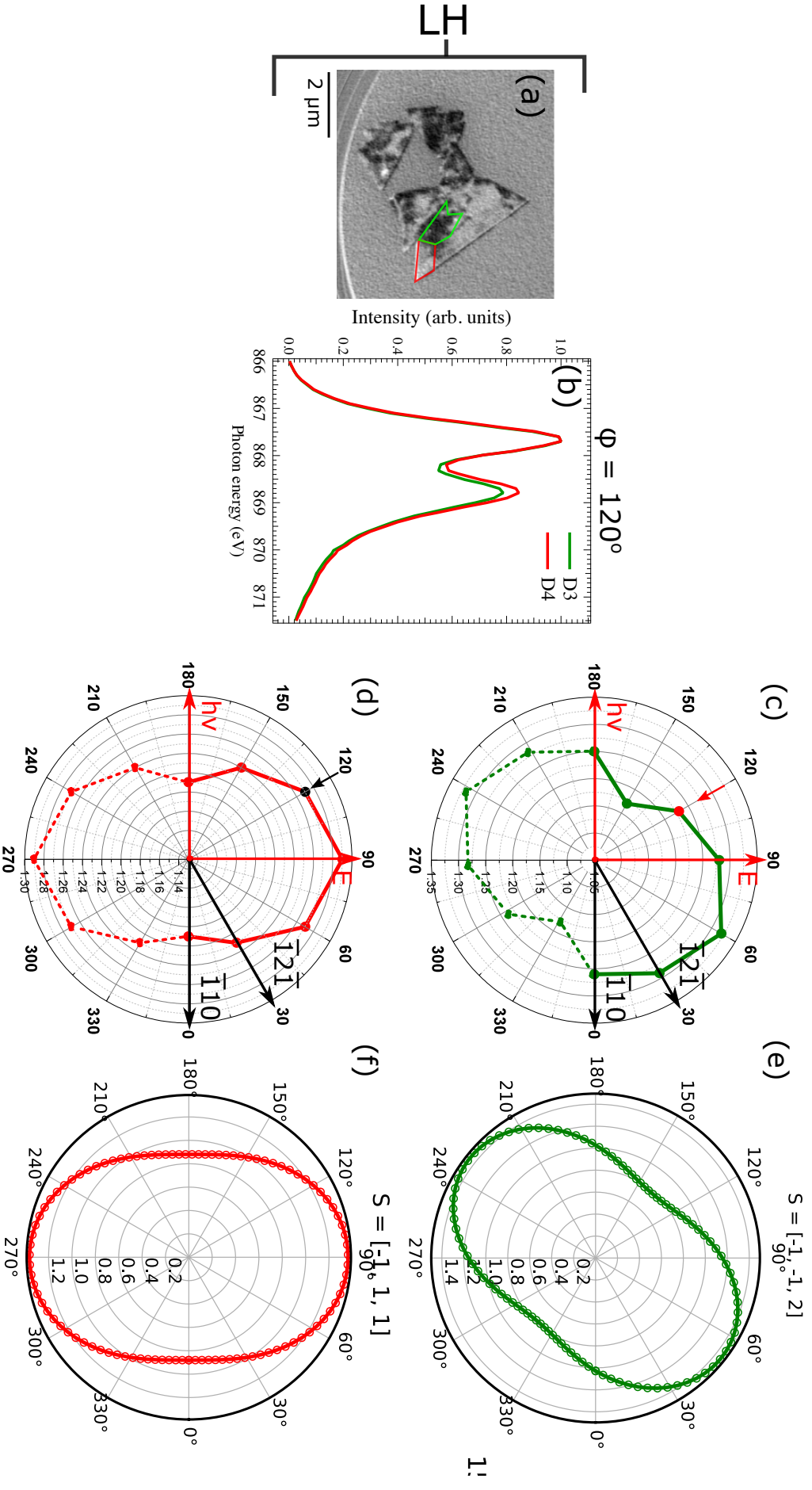


Figure 6.14: (a) Experimental XMCD PPEEM image obtained with linear horizontal photon polarization. Panel (b) shows the respective microspectra within the different domain set marked in colors in panel (a). (c) - (d) Polar plots with the experimental L_2 ratio extracted from single domain area marked in panel (a) for all the possible direction within (111) plane acquired with linear horizontal polarization. (e) - (f) the calculated L_2 ratio for a spin vectors in and out of the (111) plane, respectively.

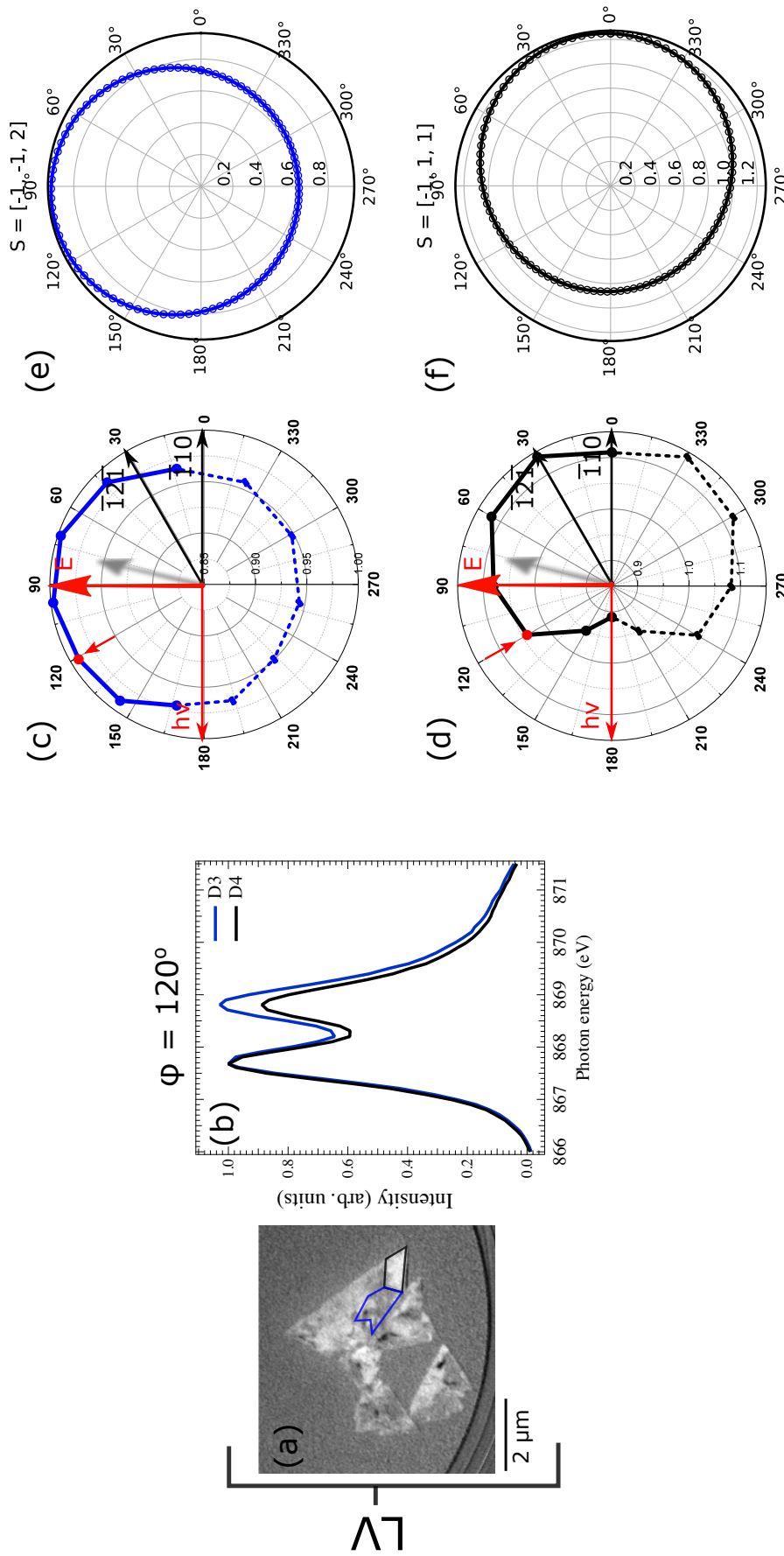


Figure 6.15: (a) Experimental XMLD PEEM image obtained with linear vertical photon polarization. Panel (b) shows the respective microspectra within the different domain set marked in colors in panel (a). (c) - (d) Polar plots with the experimental L₂ ratio extracted from single domain area marked in panel (a) for all the possible direction within (111) plane acquired with linear vertical polarization. (e) - (f) the calculated L₂ ratio for a spin vectors within and out of (111) plane, respectively.

6.5 Conclusions

In summary, Fe-doped NiO films have been grown on Ru(0001) by high-temperature oxygen-assisted molecular beam epitaxy. We have found that a small amount of Fe changes drastically the growth mode. Instead of the small, grainy islands observed for pure nickel oxide, the formation of micrometric islands is prompted. The structures are easily recognized by their triangular shape and they coexist with a few minority islands rotated 30° with respect to the Ru axes. The structural characterization performed with LEEM and μ -LEED confirms two types of triangular islands with (111) orientation. Chemical states of surface cations Fe^{2+} and Ni^{2+} were identified by x-ray absorption spectromicroscopy. Thus, the growth at high temperature leads to the formation of a Fe-doped nickel oxide phase as expected from the phase diagram. The element specific XMLD measurements reveal large antiferromagnetic domains at room temperature. The spin axis orientation has been extracted applying vectorial magnetometry. We found that the spin-axis orientation, in the islands aligned with the Ru axes, is along $\{\bar{1}\bar{1}2\}$ directions, whereas the rotated islands additionally present domains with out-of-plane contrast, which according to the vectorial magnetometry stems from the spin-axis pointing along $[\bar{1}11]$. Thus, the small Fe content acts as a surfactant but does not strongly influence the properties of in-situ grown NiO films on Ru for the majority of the micron-islands and could thus be used in devices requiring high structural quality and flat NiO structures. The origin of the unexpected out-of-plane contrast in some rotated islands domains could be strain, although more experiments have to be performed to fully understand it. The growth and analysis method employed here provide an excellent starting point for study of novel spin phenomena in NiO thin films. We found that the spin axis orientation is mostly in plane, along the $\{\bar{1}\bar{1}2\}$ directions, but it depends on the relative orientation of the NiO lattice with respect to the Ru substrate.

6.6 References

- [1] P. Němec et al. Antiferromagnetic opto-spintronics. *Nat. Phys.*, 2018. doi:10.1038/s41567-018-0051-x.
- [2] X. Marti et al. Room-temperature antiferromagnetic memory resistor. *Nat. Mater.*, 2014. doi:10.1038/nmat3861.
- [3] V. Baltz et al. Antiferromagnetic spintronics. *Rev. Mod. Phys.*, 2018. doi:10.1103/RevModPhys.90.015005.
- [4] J. Železný et al. Spin transport and spin torque in antiferromagnetic devices. *Nat. Phys.*, 2018. doi:10.1038/s41567-018-0062-7.
- [5] R. A. Duine et al. Synthetic antiferromagnetic spintronics. *Nat. Phys.*, 2018. doi:10.1038/s41567-018-0050-y.

-
- [6] C. Hahn et al. Conduction of spin currents through insulating antiferromagnetic oxides. *EPL*, 2014. doi:10.1209/0295-5075/108/57005.
- [7] H. Wang et al. Spin transport in antiferromagnetic insulators mediated by magnetic correlations. *Phys. Rev. B*, 2015. doi:10.1103/PhysRevB.91.220410.
- [8] W. Lin et al. Enhancement of thermally injected spin current through an antiferromagnetic insulator. *Phys. Rev. Lett.*, 2016. doi:10.1103/PhysRevLett.116.186601.
- [9] H. Wang et al. Antiferromagnonic spin transport from $\text{y}_3\text{fe}_5\text{o}_{12}$ into nio. *Phys. Rev. Lett.*, 2014. doi:10.1103/PhysRevLett.113.097202.
- [10] D. Alders et al. Temperature and thickness dependence of magnetic moments in NiO epitaxial films. *Phys. Rev. B*, 1998. doi:10.1103/PhysRevB.57.11623.
- [11] W. L. Roth. Magnetic Structures of MnO, FeO, CoO, and NiO. *Phys. Rev.*, 1958. doi:10.1103/PhysRev.110.1333.
- [12] M. Finazzi and S. Altieri. Magnetic dipolar anisotropy in strained antiferromagnetic films. *Phys. Rev. B*, 2003. doi:10.1103/PhysRevB.68.054420.
- [13] V. S. Mandel. Twin domains in nickel-oxide type crystals. *J. Cryst. Growth*, 1997. doi:10.1016/S0022-0248(96)01146-3.
- [14] J. Baruchel et al. Antiferromagnetic s-domains in nio. *Philosophical Magazine B*, 1981. doi:10.1080/01418638108222351.
- [15] I. Sanger et al. Distribution of antiferromagnetic spin and twin domains in NiO. *Phys. Rev. B*, 2006. doi:10.1103/PhysRevB.74.144401.
- [16] M. Finazzi et al. Interface Coupling Transition in a Thin Epitaxial Antiferromagnetic Film Interacting with a Ferromagnetic Substrate. *Phys. Rev. Lett.*, 2006. doi:10.1103/PhysRevLett.97.097202.
- [17] F. L. A. Machado et al. Spin-flop transition in the easy-plane antiferromagnet nickel oxide. *Phys. Rev. B*, 2017. doi:10.1103/PhysRevB.95.104418.
- [18] S. D. Peacor and T. Hibma. Reflection high-energy electron diffraction study of the growth of NiO and CoO thin films by molecular beam epitaxy. *Surf. Sci.*, 1994. doi:10.1016/0039-6028(94)91283-1.
- [19] A. Rota et al. Growth of oxide-metal interfaces by atomic oxygen: Monolayer of NiO(001) on Ag(001). *Phys. Rev. B*, 2009. doi:10.1103/PhysRevB.79.161401.

- [20] J. Wollschläger et al. Growth of NiO and MgO Films on Ag(100). *Thin Solid Films*, 2001. doi:10.1016/S0040-6090(01)01482-1.
- [21] C. Giovanardi et al. Oxygen-dosage effect on the structure and composition of ultrathin NiO layers reactively grown on Ag(001). *Phys. Rev. B*, 2004. doi:10.1103/PhysRevB.69.075418.
- [22] C. Hagedorf et al. Pressure-dependent Ni–O phase transitions and Ni oxide formation on Pt(111): An in situ STM study at elevated temperatures. *Phys. Chem. Chem. Phys.*, 2006. doi:10.1039/B516070G.
- [23] G. Parteder et al. Growth and Oxidation of Ni Nanostructures on Stepped Rh Surfaces. *J. Phys. Chem. C*, 2008. doi:10.1021/jp807259n.
- [24] S. Agnoli et al. Experimental and Theoretical Study of a Surface Stabilized Monolayer Phase of Nickel Oxide on Pd(100). *J. Phys. Chem. B*, 2005. doi:10.1021/jp052394s.
- [25] K. Fominykh et al. Iron-Doped Nickel Oxide Nanocrystals as Highly Efficient Electrocatalysts for Alkaline Water Splitting. *ACS Nano*, 2015. doi:10.1021/acsnano.5b00520.
- [26] F. Haaß et al. Quantitative elaboration of the defect structure of iron doped nickel oxide $(\text{Ni}_{0.955}\text{Fe}_{0.045})_{1-\delta}\text{O}$ by in situ X-ray absorption spectroscopy. *Phys. Chem. Chem. Phys.*, 2001. doi:10.1039/B103884M.
- [27] F. Haaß et al. High-temperature in situ X-ray absorption studies on the iron valence in iron-doped nickel oxide $(\text{Ni}_{1-x}\text{Fe}_x)_{1-\delta}\text{O}$. *Solid State Ion.*, 2001. doi:10.1016/S0167-2738(01)00763-9.
- [28] M. Copel et al. Surfactants in epitaxial growth. *Phys. Rev. Lett.*, 1989. doi:10.1103/PhysRevLett.63.632.
- [29] A. Mandziak et al. Structure and magnetism of ultrathin nickel-iron oxides grown on Ru(0001) by high-temperature oxygen-assisted molecular beam epitaxy. *Sci. Rep.*, 2018. URL: <https://doi.org/10.1038/s41598-018-36356-6>, doi:10.1038/s41598-018-36356-6.
- [30] H. Ohldag et al. Correlation of crystallographic and magnetic domains at Co/NiO(001) interfaces. *Phys. Rev. B*, 2009. doi:10.1103/PhysRevB.79.052403.
- [31] T. Kinoshita et al. Antiferromagnetic Domain Structure Imaging of Cleaved NiO(100) Surface Using Nonmagnetic Linear Dichroism at O *K* Edge: Essential Effect of Antiferromagnetic Crystal Distortion. *J. Phys. Soc. Jpn.*, 2004. doi:10.1143/JPSJ.73.2932.

-
- [32] G. van der Laan et al. Anisotropic x-ray magnetic linear dichroism and spectromicroscopy of interfacial Co/NiO(001). *Phys. Rev. B*, 2011. doi:[10.1103/PhysRevB.83.064409](https://doi.org/10.1103/PhysRevB.83.064409).
- [33] P. S. Miedema and F. M. de Groot. The iron L edges: Fe 2p X-ray absorption and electron energy loss spectroscopy. *J. Electron Spectrosc. Relat. Phenom.*, 2013. doi:[10.1016/j.elspec.2013.03.005](https://doi.org/10.1016/j.elspec.2013.03.005).
- [34] M. W. Haverkort et al. Magnetic versus crystal-field linear dichroism in NiO thin films. *Phys. Rev. B*, 2004. doi:[10.1103/PhysRevB.69.020408](https://doi.org/10.1103/PhysRevB.69.020408).
- [35] T. Hibma and M. W. Haverkort. Antiferromagnetic Oxide Films on Nonmagnetic Substrates. In *Magnetic Properties of Antiferromagnetic Oxide Materials*, pages 99–142. 2010. doi:[10.1002/9783527630370.ch4](https://doi.org/10.1002/9783527630370.ch4).
- [36] I. P. Krug et al. Impact of interface orientation on magnetic coupling in highly ordered systems: A case study of the low-indexed Fe₃O₄/NiO interfaces. *Phys. Rev. B*, 2008. doi:[10.1103/PhysRevB.78.064427](https://doi.org/10.1103/PhysRevB.78.064427).
- [37] M. W. Haverkort et al. Symmetry analysis of magneto-optical effects: The case of x-ray diffraction and x-ray absorption at the transition metal $\{L\}_{2,3}$ edge. *Phys. Rev. B*, 2010. doi:[10.1103/PhysRevB.82.094403](https://doi.org/10.1103/PhysRevB.82.094403).
- [38] M. Retegan. 2019. URL: <https://dx.doi.org/10.5281/zenodo.1008184>, doi:[10.5281/zenodo.1008184](https://doi.org/10.5281/zenodo.1008184).
- [39] I. P. Krug et al. Magnetic coupling in highly ordered NiO/Fe₃O₄(110): Ultrasharp magnetic interfaces vs. long-range magnetoelastic interactions. *EPL*, 2007. doi:[10.1209/0295-5075/81/17005](https://doi.org/10.1209/0295-5075/81/17005).
- [40] I. P. Krug. private communication.

7 Magnetite - Fe_3O_4 Manipulation of magnetic domains in thin magnetite films

In this Chapter we present the first experiments with the new sample holder system comprised of two different sample holder bodies: one with a filament for high temperature measurements (up to more than 1500 K) and the second one with the integrated electromagnets for the in-situ application of small magnetic fields either in-plane or out-of-plane (Appendix A). In order to illustrate its capabilities microstructures of ferrimagnetic Fe_3O_4 were grown in-situ on a Ru(0001) substrate by oxygen-assisted high temperature MBE. The switching characteristics of individual magnetite microstructures under an applied magnetic field were subsequently imaged by means of XMCD-PEEM at resolution of a tens of nm.

7.1 Introduction

The study of static and dynamic properties of magnetic domains in ferromagnetic nanostructures has recently received a lot of attention not only because of the fundamental interest, but also due to the emergence of technological applications based for example on domain walls (DWs) and their dynamics in memory [1–5] and logic devices[6–9].

Consequently their behaviour under applied magnetic field[10–13] or spin-polarized electric currents[14; 15] as a driving force has been studied extensively over the past years. For most spintronic applications, thin films or smaller dimensionality structures are required. Thus there is a strong motivation to understand and control the growth of ferromagnetic films and nanostructures and to study their magnetic properties and their modification by applied magnetic fields.

One of the most attractive candidate for spintronic applications is magnetite Fe_3O_4 , due to its ubiquity and inexpensive production. In its bulk form, it is a soft magnet with a magnetic moment of $4.07 \mu_B$ per formula unit, and a high Curie temperature ($T_C \simeq 850$ K). It crystallizes in the cubic inverse spinel structure where tetrahedral sites are occupied by Fe^{3+} , while the octahedral ones are populated by both Fe^{2+} and Fe^{3+} cations. The two sublattices are coupled antiferromagnetically, so the

spin contribution of Fe^{3+} cancel out between both lattices. Thus, the net magnetic moment arises mainly from Fe^{2+} cations. The orbital moment is negligible leading to a small magnetocrystalline anisotropy that favours the $\langle 111 \rangle$ easy axes at room temperature.

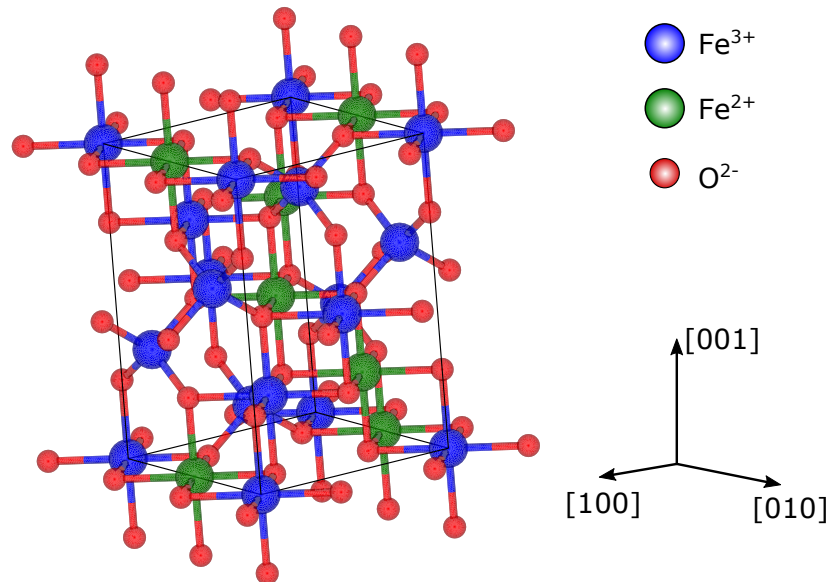


Figure 7.1: Schematic illustration of magnetite crystal structure

The growth of magnetite films and nanostructures has been the subject of many studies. A common observation of thin magnetite films is that often its magnetic properties are disappointing[16; 17]. In most cases, the modification of magnetic properties is not attributed to the reduction of dimensionality as they also appear in a structures a hundred of nanometers thick. The unexpected properties including high coercivities[18; 19] or new-easy axis[20; 21] are attributed to the presence of growth defects named antiphase boundaries (APBs), to which we have also referred in the case of nickel ferrite (Chapter 4).

7.2 Growth and crystal structure

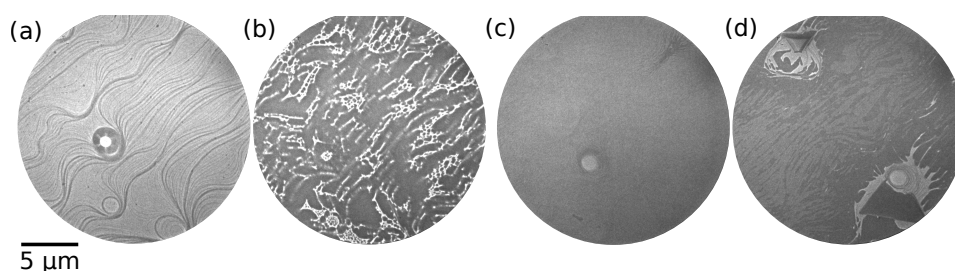


Figure 7.2: Frames selected from a sequence of images acquired during the growth of Fe_3O_4 at 1150 K at a background pressure 1×10^{-6} mbar of molecular oxygen. The frames correspond to (a) 20 sec, (b) 11 min, (c) 24 min and (d) 50 min (2 ML of FeO on Ru – 20 min).

Magnetite was grown by oxygen-assisted high temperature MBE, as described in Chapter 2.1 and illustrated in Figure 7.2. As already reported, initially small islands start to nucleate and grow on Ru(0001) (Figure 7.2a–b). When they coalesce the entire surface is covered by a so-called wetting layer with FeO composition (Figure 7.2c), on top of which the growth proceeds in the form of 3-dimensional islands of magnetite (Fe_3O_4) (Figure 7.2d). The sequence reproduces previous experiments by our group. The growth process in total took one hour. Figure 7.3a is a LEEM image of a couple of magnetite islands grown by this method at 1150 K on Ru(0001). Already the very different electron reflectivity of islands and wetting layer in the LEEM image reveal their different nature. The crystallographic structure of wetting layer and island were confirmed by μ -spot LEED measurements, as shown in Figure 7.3b–c. The wetting layer presents a 1×1 pattern with characteristic satellite spots arising from the in-plane mismatch between the Ru substrate and the wetting layer. The resulting in-plane lattice spacing is 0.32 nm in agreement with the value reported for FeO on Ru(0001)[22]. In contrast, the large triangular island presents additional spots in a 2×2 position related to the bigger unit cell of a spinel structure along the [111] direction suggesting the Fe_3O_4 (111) oxide surface. The island's oxygen lattice spacing obtained by LEED is similar to the wetting layer 0.31 nm. The additional closely-spaced spots from the islands are assigned to a surface reconstruction of magnetite, the bi-phase reconstruction for which a recent model has been proposed[23].

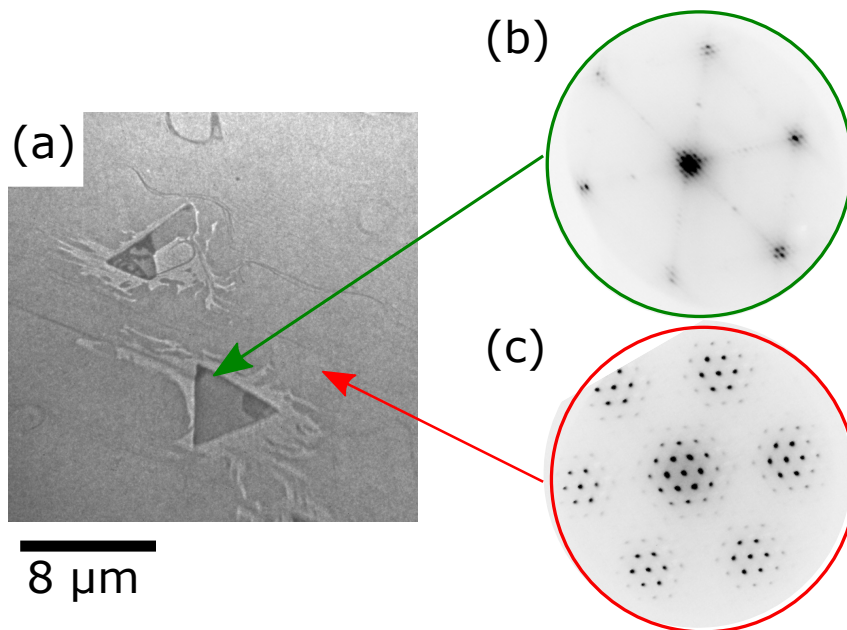


Figure 7.3: (a) LEEM image of magnetite crystals grown on Ru(0001) substrate at the electron energy 5 eV and μ -spot low energy electron diffraction patterns (acquired at 45eV) (b) of magnetite crystal and (c) the surrounding wetting layer.

7.3 Evolution of magnetic domains in magnetite microstructures

As a next step, the $\text{Fe}_3\text{O}_4/\text{Ru}$ sample was transferred to the electromagnet holder without leaving the ultra high vacuum system.

To get insight into the chemical nature of the island the X-ray absorption spectra (XAS) were measured at both $L_{3,2}$ Fe edges. Figure 7.4 shows the Fe XAS and X-ray Magnetic Circular Dichroism (XMCD) spectra from the island in Figure 7.4a. The Fe L_3 -edge XMCD spectrum has a typical three peak structure arises from the different iron cations (Fe^{2+} and Fe^{3+}) located in octahedral and tetrahedral sites within spinel structures, and is typical of magnetite[24]. Next, the sample was magnetically mapped by means of (XMCD) PEEM images at the Fe L_3 absorption edge (first peak at the XMCD spectrum). Figure 7.4a shows the magnetic domain distribution of the magnetite island after a demagnetization cycle performed by the built-in elec-

tromagnet. A clear magnetic contrast is observed in the magnetite island while the wetting layer does not present any magnetic contrast at room temperature.

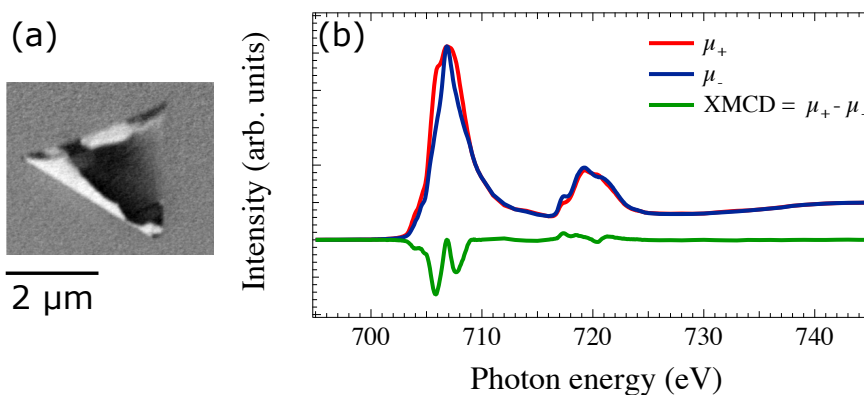


Figure 7.4: (a) XMCD PEEM image of magnetite island, (b) XAS (top) and XMCD spectra (bottom) at the Fe L-edges from the central dark domain.

Next the magnetic state of the single magnetite island was changed by applying short magnetic field pulses. The evolution of the magnetic domains under applied field is shown in Figure 7.5b,c (red and blue areas indicate different orientations of the magnetization with respect to the X-ray beam incidence direction, i.e., different ferrimagnetic domains). It can be seen that even after a small pulse (10 mT) is applied the distribution of the domains has changed, indicating the low pinning of most of the island. Increasing the value of B up to 50 mT the domains tend to align in the direction of the applied field, although saturation is not reached. In order to check the reversibility of this process the maximum field was applied in an opposite direction (Figure 7.5c). The magnetic contrast inside the island shown in Figure 7.5d is reversed but the domains do have a one to one correspondence with those of Figure 7.5b when the magnetic field was applied in an opposite direction with the same absolute value.

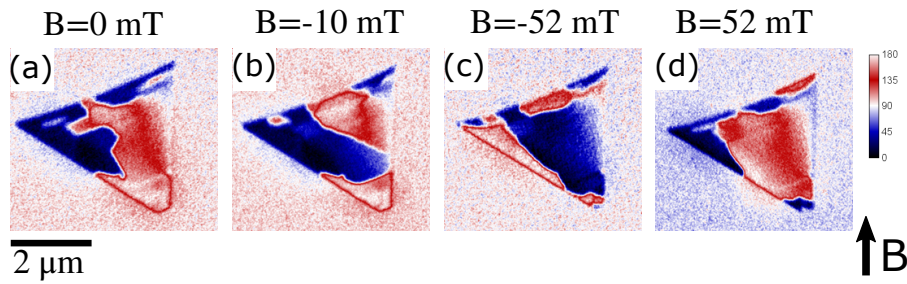


Figure 7.5: Magnetic state of Fe_3O_4 under applied pulses of in-plane magnetic field according to XMCD contrast at the Fe L_3 -absorption edge: (a) after the demagnetization cycle. After short pulses of magnetic field (b) -10 mT, (c) -52 mT and (d) 52 mT. Red and blue correspond to the two different antiparallel in-plane magnetization directions, while white lines indicate the presence of a domain wall.

The possible origin of the irreversibility of some domains around the island periphery could be due to defects in the islands. The motion of domain walls through a magnetic material depends in detail upon the structural properties of the material. Non-magnetic defects in the volume of a ferromagnetic material, such as twin boundaries, steps or dislocations, can cause "pinning" of the domain walls. Such pinning sites cause the domain wall to be trapped in a local energy minimum. Strong pinning arises when these defects have a dimension comparable to the domain wall width δ_w . Especially planar defects are most effective pinning centres because whole wall finds itself with a different total energy when it encompasses the defect (Figure 7.6). The planar defect interacts with DWs, acting either as a trap or a barrier making it more difficult to move. Thus, the domain wall pinning strongly influences the properties of magnetic materials increasing for example the coercivity. This can be observed directly if even applying the external magnetic field higher than the saturation magnetization the magnetic body does not become a single-domain state.

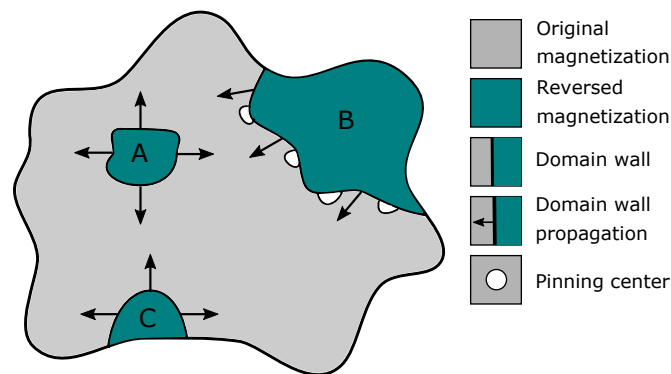


Figure 7.6: Processes involved in magnetization reversal.

7.4 Landau state of a thick magnetite microstructures

In addition to nm thin Fe_3O_4 microstructures, the growth by MBE can lead to the formation of thick (over tens of nm) 3-dimensional islands as shown in Figure 7.7. The island creates a clear shadow on the left in the XAS image (Figure 7.7a). The height of that island, estimated from the shadow is 40 nm. The corresponding XMCD-PEEM image is shown in Figure 7.7b. A clear magnetic contrast is observed with a flux closure domain configuration: three magnetic domains of similar size divide the triangle into three sectors, within which the magnetization is align along the side of the nearest edge. The latter is known as a *Landau state*.

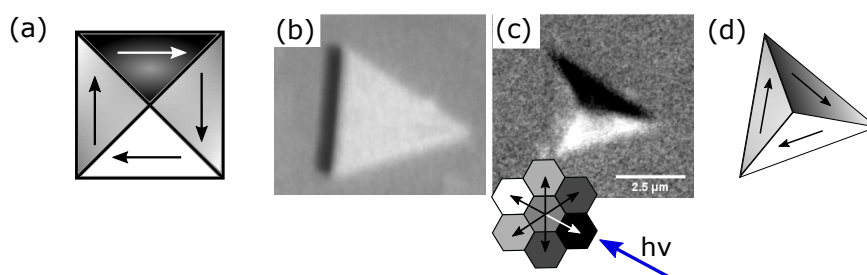


Figure 7.7: (a) Landau flux closure configuration in a square patterns. (b) XAS image of the magnetite island acquired at photon energy close to the maximum of the Fe L_3 absorption edge. (c) XMCD PEEM image at the same area. (d) Schematic illustration of Landau-closure state in triangular shape microstructure.

In the Landau state four (Figure 7.7a) (in our case three) in-plane magnetic domains form a flux-closed structures in which the magnetostatic energy is minimized (Eq. 4.4). At the center of the Landau state, in the intersection of Néel walls a magnetic vortex exists where the magnetization points in the direction perpendicular to the film plane. Since the vortex core costs a large magnetostatic energy it is usually very small, of the order of a few nm.

We can distinguish four triangular vortex structures, as shown in Figure 7.8. The handedness of a vortex is determined by aligning the thumb with the direction of the core out-of-plane magnetization, and then matching the directions of the fingers of the right or left hand with the in-plane curl direction of the Landau state. The magnetic vortex structure is special in the sense that combines the basic symmetry properties of inversion and time reversal: in Figure 7.8 it can be seen that the four structures correspond to two types of handedness, which are transformed into each other by the parity operation, and the two magnetization directions which can be transformed into each other by the time reversal operation (since the magnetization is an axial vector).

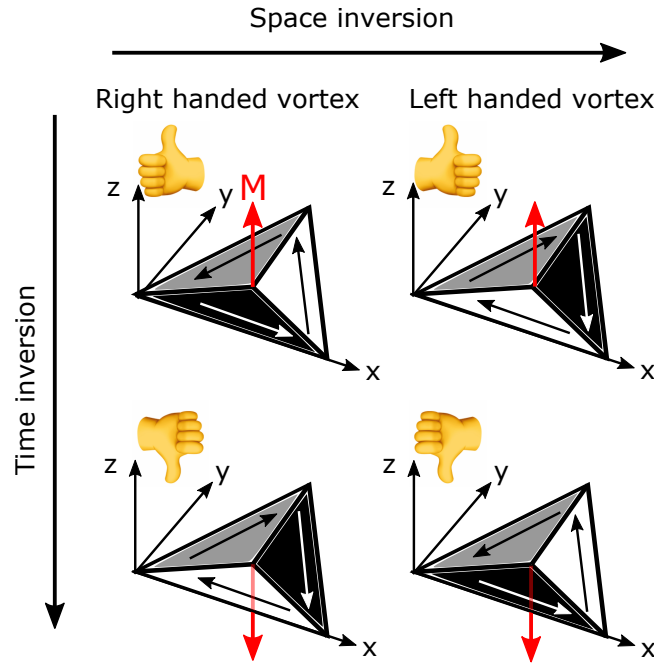


Figure 7.8: The four basic magnetic vortices, classified by their handedness and out-of-plane direction of the core.

However, the Landau state is not only the vortex core. It possesses a composite magnetic character in which we can distinguish three different magnetic substructures: domains, domain walls and vortex core. The spontaneous magnetization M within each of the three domains is constant and points along the in-plane directions. The three substructures differ in their dynamic behaviour but are mutually coupled, and are generally simultaneously excited, resulting in an overall complex dynamic behaviour of Landau states[25].

In order to better understand the observed magnetic domains distribution in the island, micromagnetic simulations have been performed on flat islands with the same shape, size and thickness as the experimental one. The values of the material properties like exchange stiffness, saturation magnetization and magnetocrystalline anisotropy were set to the values typically used for bulk magnetite: $A_{ex} = 2.64 \times 10^{-11}$ J/m, $M_S = 4.8 \times 10^5$ A/m and $K_{C1} = -1.25 \times 10^4$ J/m³ respectively[26]. The size of the micromagnetic simulation cell has been adjusted to the experimental pixel size (8.4 nm wide and 4 nm high). The magnetocrystalline anisotropy axes have been assigned to the $\langle 111 \rangle$ directions of the magnetite bulk axes at room temperature knowing that the island orientation is (111) and its sides are along the in-plane $\langle 110 \rangle$ directions. The magnetic configuration was relaxed to minimize the energy, on the basis of a Bogacki-Shampine approach available in the MuMax3 software. The results are presented in Figure 7.9a.

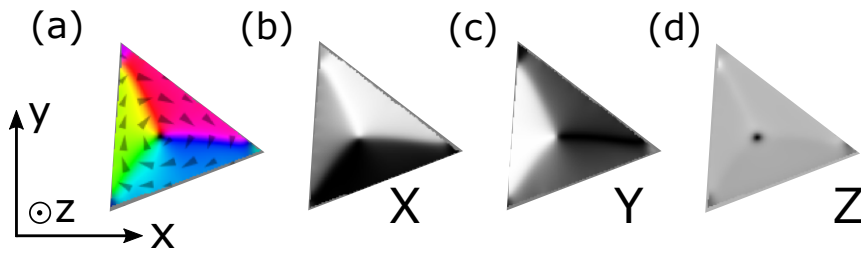


Figure 7.9: (a) Micromagnetism relaxed configuration, by using the experimental configurations and the material properties of bulk magnetite, as an input. (b) X, (c) Y and (d) Z component of the magnetization.

The magnetization distribution is very similar to the one obtained experimentally. A flux closure domain configuration aligned along the island edge (indicated by the arrows in Figure 7.9a). The magnetization of each domain is aligned along the island edge closer to it. This is the result of strong shape anisotropy contribution that overcomes the magnetocrystalline anisotropy which would actually prefer to orient the magnetization along $\langle 112 \rangle$ directions, that are the projection of the bulk $\langle 111 \rangle$ directions on the (111) plane.

Additionally, three components of the magnetization have been plotted. It can be seen in Figure 7.9d, where the z-component is shown that at the center of the triangle the aforementioned vortex core is located, pointed out-of-plane. Our group has recently confirmed by analysing the domain wall width that the magnetite island have similar micromagnetic properties to bulk magnetite[27]. Additionally, the domain walls are the Néel type.

7.5 Vortex displacement in in-plane magnetic field

Devices for spintronic applications rely on the manipulation of magnetization. Thus, study of magnetic domain wall or vortex dynamics in micro- and nanoscopic thin film structures have become of great interest in recent years due to their potential commercial applications. There have been several advances toward the use of magnetic vortex cores as memory components, where the bistability of core polarity allows for binary data storage[28–30].

A large literature already exists describing the response of the magnetization in Landau flux-closure states (e.g. in permalloy squares) under different excitation methods: laser excitation[31; 31–33], magnetoelastic coupling[34–37], or applied magnetic field [38–41]. However, comparatively less is known about the magnetic vortex dynamics, since they are small objects requiring high resolution imaging techniques.

In the present section, we study the dynamics of Landau flux-closure states found in in-situ grown magnetite. The response of the magnetization is followed by XPEEM that allows to determine the vortex displacement under applied external magnetic field.

The magnetization dynamics within small magnetic structures is described by the phenomenological Landau–Lifshitz–Gilbert equation given by:

$$\frac{d\vec{M}}{dt} = -\gamma[\vec{M} \times \vec{H}] - \frac{\alpha\gamma}{M_S}[\vec{M} \times (\vec{M} \times \vec{H})] \quad (7.1)$$

The first term of LLG equation (Eq. 7.1) describes the precession of magnetization \vec{M} at a fixed angle θ about the magnetic field direction, due to the torque $T = \vec{M} \times H$. The second term describes the relaxation back into the equilibrium state using the dimensionless damping parameter α ¹. γ is the gyromagnetic ratio of the electron[42].

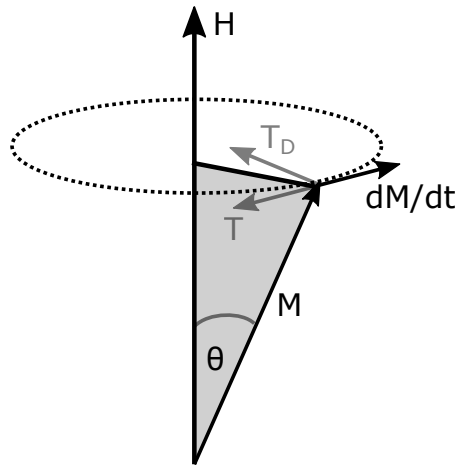


Figure 7.10: The precessional torque T and the damping torque T_D acting on the precessing magnetization M .

In the Landau state the three different substructures - domains, domain walls and vortex - differ in their total energy, leading to the to differences in the local magnetic field H and to three distinct frequencies or time scales. Within the domain the magnetization is constant and is dominated by the magnetostatic energy. The vortex itself is dominated by the exchange energy, and its motion is strongly coupled to

¹A dimensionless empirical constant usually of the order of 10^{-4} - 10^{-2} which describes the transfer of angular momentum to the crystal lattice - called damping constant or the spin lattice relaxation

the one of the domain walls (as we will see below). The walls are an intermediate case between vortex and domains, with the contribution from both exchange and magnetostatic energy.

In this paragraph we will present the excitation of the magnetic vortex structure in in-situ grown magnetite microstructures on Ru, using weak in-plane magnetic field. The spatial distribution of the magnetization \vec{M} under in-situ applied magnetic field is followed by XMCD-PEEM. The images are acquired under in-plane applied magnetic fields in the range 0 - 12 mT. Note, that since we are working with very low energy electrons, even a small magnetic field produce a bending of the electron beam and consequently an image distortion. In order to obtain reasonable resolution, the maximum applied magnetic field while imaging was 12 mT in this experiment.

The evolution of the magnetization in a magnetite triangle showing a Landau flux-closure pattern is shown in Figures 7.11 and 7.12 applying a field B in the plane of the film parallel (7.11a) or antiparallel (7.12a) to the Y axis in the image (perpendicular to the photon incidence direction). The Landau flux-closure equilibrium state is shown in left panel of Figure 7.11a. The domains oriented parallel and antiparallel to the x-ray direction appear white and black, while the one oriented perpendicular to \vec{L} is gray. Domain walls separate the triangular domains and the vortex is at the center of the triangle.

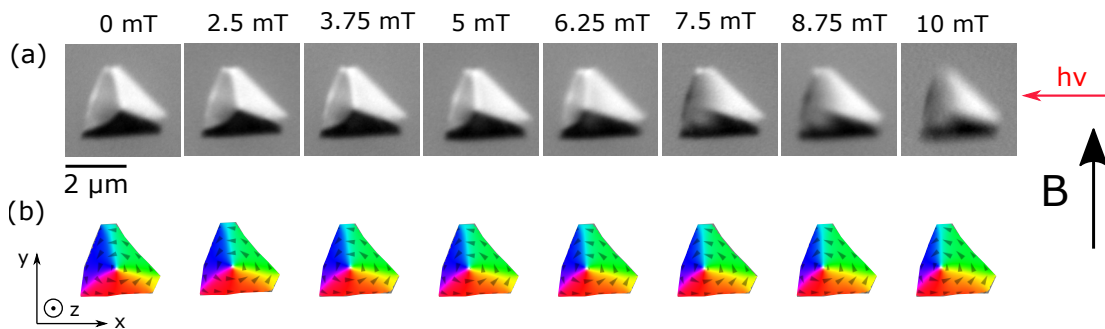


Figure 7.11: a) Selected XMCD images showing the evolution of the magnetic domains in microscopic triangular islands under in-situ applied magnetic field. (b) Micromagnetic simulations, using the experimental triangle shape as the initial input and employing the know bulk material properties of magnetite.

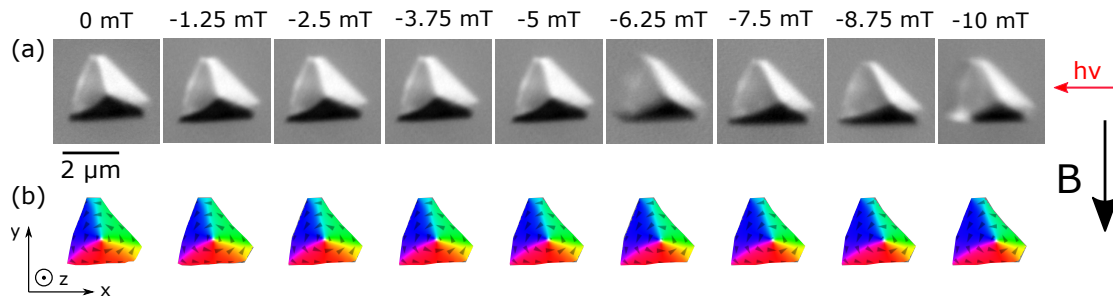


Figure 7.12: (a) Selected XMCD images showing the evolution of the magnetic domains in microscopic triangular islands under in-situ applied magnetic field. (b) Micromagnetic simulations, using the experimental triangle shape as the initial input and employing the known bulk material properties of magnetite.

It is shown that the vortex where the three domain walls meet moves in the direction perpendicular to the applied magnetic field and is enlarged while the field is increased. We can clearly see that at some value of the magnetic field the resolution of the image is getting worse (see Figure 7.11a for $\vec{B} > 7.5$ mT), due to the image distortion produced by external field \vec{B} . By inverting the direction of the magnetic field the motion is reversed. Now the magnetic field is parallel to the magnetization in the gray domain, which thus grows for increasing \vec{B} . Once the field is switched off, the Landau state relaxes back to the initial, field-free configuration.

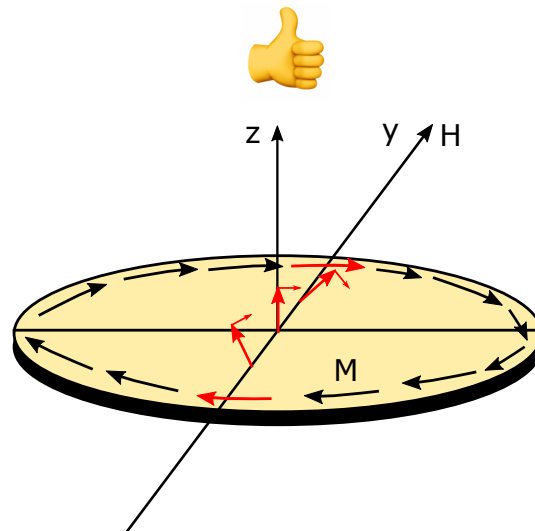


Figure 7.13: Left handed magnetic vortex structure near the center of a Landau state. The Magnetization M rotates out of the $x - y$ plane into the z direction.

In general, the quasistatic magnetization process in small fields is dominated by domain wall displacement as demonstrated in Figures 7.11 and 7.12. The domains

with a magnetization component parallel to the external field have a lower energy than those with an antiparallel component. The motion of the domain walls (domain wall displacement) leads to a minimization of the total energy by growing of the domains with parallel magnetization components at the expense of the domains with antiparallel aligned magnetization components.

The behaviour of the Landau state under an applied external magnetic field can be understood on the basis of the LLG equation (Eq. 7.1). An external magnetic field oriented perpendicular to the initial magnetization in the black domain generates a torque $\vec{T} = -\gamma \vec{M} \times \vec{H}_{eff}$ on the magnetization \vec{M} within the domain wall. For the domains oriented parallel to \vec{B} (gray and white) the torque is zero. This torque forces the magnetization \vec{M} in the black domain to rotate around the axis of the effective field that includes also a demagnetizing field \vec{H}_{demag} perpendicular to the plane of the film (which is the actual cause of the domain wall motion). Hence, the regions with the magnetization parallel to the magnetic field are enlarged and the domain wall perpendicular to applied field moves in the direction perpendicular to \vec{B} . Since the vortex motion is coupled to the motion of the domain walls, its motion is also observed.

To understand the changes in the magnetic configuration we have compared the experimental results with the micromagnetic simulations using the values of the material properties corresponding to the literature bulk magnetite ones, which as mentioned in the [27] are in good agreement with experimental the domain wall width. The simulation size was 200x200x2 cells, each of 8.46 nm x 8.46 nm x 3.9 nm is size. The in-plane cell dimensions are chosen to coincide with the in-plane resolution of the experimental images, while the out-of-plane dimension is chosen to be an integer fraction of the island height, as determined from the shadow in XPEEM. The magnetic field was adjusted to be in the same range as the one we have been using in our experiment. A vortex configuration was used as the initial magnetization, and the magnetization under the applied field was relaxed for each field. The results for two opposite field directions are shown in the lower panel (b) in Figures 7.11 and 7.12. The simulations on the triangular island indicate a good qualitative agreement with the experimental data. The domains with the magnetization direction parallel to the external field direction grow causing the domain wall motion in the direction perpendicular to H . Additionally the core of the Landau state follows the domain wall motion.

In order to check the quantitative agreement between our experimental and theoretical results, we have extracted the absolute vortex displacement as a function of the applied field. The data are plotted in Figures 7.14 and 7.15. It is shown that the displacement for the highest reachable magnetic field is more than 300 nm. The vortex displacement extracted from the simulations is of the same magnitude and follows the experimental trend. Small discrepancies at higher fields can be attributed to the image distortion.

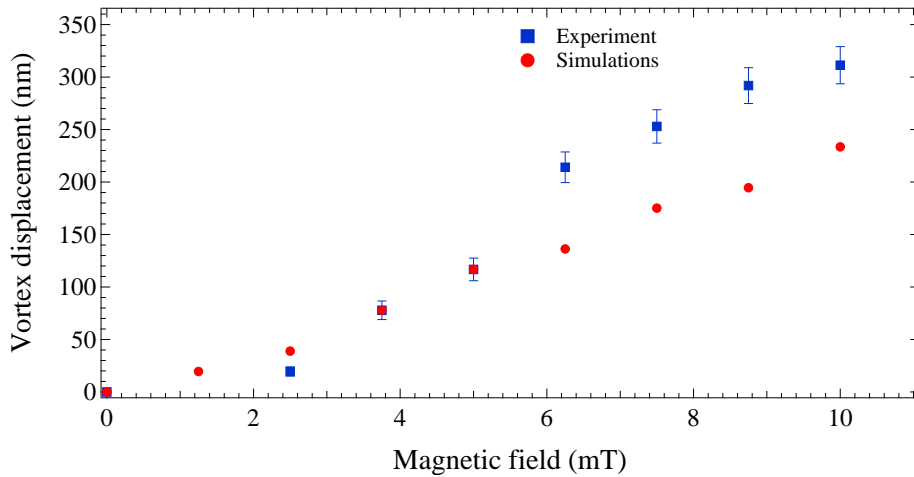


Figure 7.14: Experimental and theoretical absolute vortex displacement versus in-plane applied magnetic field parallel to the Y axis (see Figure 7.11).

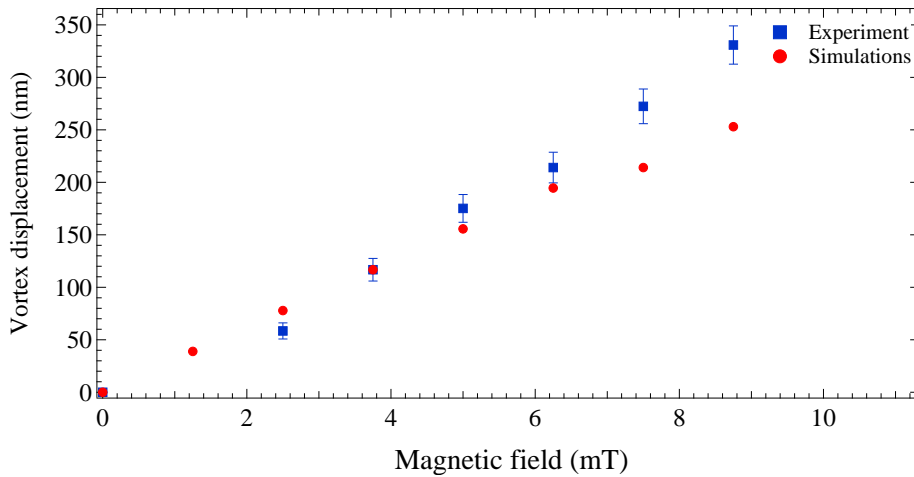


Figure 7.15: Experimental and theoretical absolute vortex displacement versus in-plane applied magnetic field antiparallel to the Y axis (see Figure 7.12).

It can be seen that the micromagnetic simulations with bulk magnetite parameters closely coincide with the XMCD-PEEM observations, accurately explaining the response of Landau state under an in-plane applied magnetic field. In the initial configuration the magnetization in each domain is parallel to the side of the island and presents a flux closure domain configuration. The domains are separated by well defined, narrow domain walls. By applying a magnetic field, a domain wall parallel to the magnetic field direction starts to move perpendicularly to \vec{B} . Together with the domain wall motion, a vortex core moves in the same direction. In general the observation that the island behaves as expected from the know properties of the bulk material implies that the islands are of extremely high crystalline and chemical quality despite the reduced dimensionality. In particular, the absence of aniphase boundaries that would influence the vortex motion is remarkable, especially as com-

pared with the magnetite films grown by other methods. This is in agreement with a direct comparison of the domain wall width.

7.6 Conclusions

In summary, we present first experiments with the new custom-made exchangeable sample-holder system for LEEM/PEEM comprising a sample holder body for high-temperature measurements and another one with an integrated mini-electromagnet for the in-situ application of small magnetic fields. As an example, thin magnetite films on Ru(0001) were grown and characterized in situ. Furthermore, we showed experimental data confirming that by applying an in-plane small magnetic field it is possible to change the magnetic state of ferrimagnetic thin films of Fe_3O_4 .

Further, we have observed that thicker magnetite islands present a flux-closure Landau states. The magnetic field excitation of the Landau state leads to domain wall motion. The movement of the domain wall implies also a vortex displacement that is perpendicular to the exciting field. The experimental vortex motion has been compared with micromagnetic simulations performed for the objects with the same shape and initial magnetization as the experimental one. It has been found that the behaviour of Landau state under applied in-plane magnetic field is well reproduced in the micromagnetic simulations. This confirms that the oxygen-assisted high-temperature growth by MBE on Ru substrate leads to the formation of magnetite microstructures with bulk properties as previously reported on non-dynamic experiments.

7.7 References

- [1] K.-W. Moon et al. Magnetic bubblecade memory based on chiral domain walls. *Sci. Rep.*, 2015. doi:10.1038/srep09166.
- [2] A. Bisig et al. Correlation between spin structure oscillations and domain wall velocities. *Nat. Commun.*, 2013. doi:10.1038/ncomms3328.
- [3] O. Zografos et al. Exchange-driven Magnetic Logic. *Sci. Rep.*, 2017. doi:10.1038/s41598-017-12447-8.
- [4] S. S. P. Parkin et al. Magnetic Domain-Wall Racetrack Memory. *Science*, 2008. doi:10.1126/science.1145799.
- [5] S. E. Barnes et al. Magnetic memory and current amplification devices using moving domain walls. *Appl. Phys. Lett.*, 2006. doi:10.1063/1.2354036.

- [6] Y. Zhang et al. 2018. [arXiv:1803.02552](https://arxiv.org/abs/1803.02552).
- [7] M. Rao et al. Design and simulation of magnetic logic device for next generation data processing. In *2015 19th International Symposium on VLSI Design and Test*, 2015. [doi:10.1109/ISVDAT.2015.7208089](https://doi.org/10.1109/ISVDAT.2015.7208089).
- [8] R. P. Cowburn and M. E. Welland. Room Temperature Magnetic Quantum Cellular Automata. *Science*, 2000. [doi:10.1126/science.287.5457.1466](https://doi.org/10.1126/science.287.5457.1466).
- [9] D. A. Allwood et al. Submicrometer Ferromagnetic NOT Gate and Shift Register. *Science*, 2002. [doi:10.1126/science.1070595](https://doi.org/10.1126/science.1070595).
- [10] M. Hayashi et al. Direct observation of the coherent precession of magnetic domain walls propagating along permalloy nanowires. *Nat. Phys.*, 2007. [doi:10.1038/nphys464](https://doi.org/10.1038/nphys464).
- [11] G. S. D. Beach et al. Dynamics of field-driven domain-wall propagation in ferromagnetic nanowires. *Nat. Mater.*, 2005. [doi:10.1038/nmat1477](https://doi.org/10.1038/nmat1477).
- [12] A. Hrabec. *Domain wall dynamics in magnetic nanostructures: Effect of magnetic field and electric current*. PhD thesis, 2011.
- [13] H. W. Schumacher et al. Control of the magnetic domain wall propagation in Pt/Co/Pt ultra thin films using direct mechanical AFM lithography. *J. Magn. Magn. Mater*, 2002. [doi:10.1016/S0304-8853\(01\)00727-2](https://doi.org/10.1016/S0304-8853(01)00727-2).
- [14] M. Kläui et al. Domain wall motion induced by spin polarized currents in ferromagnetic ring structures. *Appl. Phys. Lett.*, 2003. [doi:10.1063/1.1588736](https://doi.org/10.1063/1.1588736).
- [15] M. Kläui et al. Direct Observation of Domain-Wall Configurations Transformed by Spin Currents. *Phys. Rev. Lett.*, 2005. [doi:10.1103/PhysRevLett.95.026601](https://doi.org/10.1103/PhysRevLett.95.026601).
- [16] S. S. P. Parkin et al. Observation of magnetic dead layers at the surface of iron oxide films. *Appl. Phys. Lett.*, 1986. [doi:10.1063/1.96481](https://doi.org/10.1063/1.96481).
- [17] J.-X. Yin et al. Unconventional magnetization of Fe₃O₄ thin film grown on amorphous SiO₂ substrate. *AIP Advances*, 2016. [doi:10.1063/1.4954035](https://doi.org/10.1063/1.4954035).
- [18] D. T. Margulies et al. Anomalous moment and anisotropy behavior in Fe₃O₄ films. *Phys. Rev. B*, 1996. [doi:10.1103/PhysRevB.53.9175](https://doi.org/10.1103/PhysRevB.53.9175).
- [19] F. C. Voogt et al. Superparamagnetic behavior of structural domains in epitaxial ultrathin magnetite films. *Phys. Rev. B*, 1998. [doi:10.1103/PhysRevB.57.R8107](https://doi.org/10.1103/PhysRevB.57.R8107).

- [20] P. Prieto et al. Fourfold in-plane magnetic anisotropy of magnetite thin films grown on tin buffered Si(001) by ion-assisted sputtering. *J. Mater. Chem. C*, 2016. doi:10.1039/C6TC02152B.
- [21] M. Monti et al. Room temperature in-plane $\langle 100 \rangle$ magnetic easy axis for $\text{Fe}_3\text{O}_4/\text{SrTiO}_3(001):\text{Nb}$ grown by infrared pulsed laser deposition. *Journal of Applied Physics*, 2013. doi:10.1063/1.4837656.
- [22] I. Palacio et al. Initial stages of FeO growth on Ru(0001). *J. Phys.: Condens. Matter*, 2013. doi:10.1088/0953-8984/25/48/484001.
- [23] N. Spiridis et al. Superstructures on epitaxial $\text{Fe}_3\text{O}_4(111)$ films: Biphasic formation versus the degree of reduction. *The Journal of Physical Chemistry C*, 2019. doi:10.1021/acs.jpcc.8b11400.
- [24] E. Goering et al. Vanishing Fe 3d orbital moments in single-crystalline magnetite. *EPL*, 2005. doi:10.1209/epl/i2005-10359-8.
- [25] J. Stöhr and H. C. Siegmann. *Magnetism: From Fundamentals to Nanoscale Dynamics*. Springer Series in Solid-State Sciences. Springer-Verlag, 2006. doi:10.1007/978-3-540-30283-4.
- [26] A. Hubert and R. Schäfer. *Magnetic Domains: The Analysis of Magnetic Microstructures*. Springer-Verlag, 1998. doi:10.1007/978-3-540-85054-0.
- [27] S. Ruiz-Gómez et al. Geometrically defined spin structures in ultrathin Fe_3O_4 with bulk like magnetic properties. *Nanoscale*, 2018. doi:10.1039/C7NR07143D.
- [28] S. Bohlens et al. Current controlled random-access memory based on magnetic vortex handedness. *Appl. Phys. Lett.*, 2008. doi:10.1063/1.2998584.
- [29] B. Pigeau et al. A frequency-controlled magnetic vortex memory. *Appl. Phys. Lett.*, 2010. doi:10.1063/1.3373833.
- [30] K. Nakano et al. All-electrical operation of magnetic vortex core memory cell. *Appl. Phys. Lett.*, 2011. doi:10.1063/1.3673303.
- [31] J. Raabe et al. Quantitative analysis of magnetic excitations in Landau flux-closure structures using synchrotron-radiation microscopy. *Phys. Rev. Lett.*, 2005. doi:10.1103/PhysRevLett.94.217204.
- [32] X. Zhu et al. Broadband spin dynamics of the magnetic vortex state: Effect of the pulsed field direction. *Phys. Rev. B*, 2005. doi:10.1103/PhysRevB.71.180408.

- [33] D. Chumakov et al. Nanosecond time-scale switching of permalloy thin film elements studied by wide-field time-resolved kerr microscopy. *Phys. Rev. B*, 2005. doi:10.1103/PhysRevB.71.014410.
- [34] S. Finizio et al. Magnetic anisotropy engineering in thin film Ni nanostructures by magnetoelastic coupling. *Phys. Rev. Appl.*, 2014. doi:10.1103/PhysRevApplied.1.021001.
- [35] S. Finizio et al. Control of the gyration dynamics of magnetic vortices by the magnetoelastic effect. *Phys. Rev. B*, 2017. doi:10.1103/PhysRevB.96.054438.
- [36] M. Foerster et al. Direct imaging of delayed magneto-dynamic modes induced by surface acoustic waves. *Nat. Commun.*, 2017. doi:10.1038/s41467-017-00456-0.
- [37] M. Filianina et al. Piezo-electrical control of gyration dynamics of magnetic vortices. *Applied Physics Letters*, 2019. doi:10.1063/1.5110169.
- [38] M. Bailleul et al. Microwave spectrum of square permalloy dots: Multidomain state. *Phys. Rev. B*, 2007. doi:10.1103/PhysRevB.76.224401.
- [39] A. Neudert et al. Small-amplitude magnetization dynamics in permalloy elements investigated by time-resolved wide-field kerr microscopy. *Phys. Rev. B*, 2005. doi:10.1103/PhysRevB.71.134405.
- [40] C. M. Schneider et al. Incoherent magnetization rotation observed in sub-nanosecond time-resolving x-ray photoemission electron microscopy. *Applied Physics Letters*, 2004. doi:10.1063/1.1790606.
- [41] Transient spatio-temporal domain patterns in permalloy microstructures induced by fast magnetic field pulses. *Nuclear Instruments and Methods in Physics Research Section B: Beam Interactions with Materials and Atoms*, 2006. Synchrotron Radiation and Materials Science. doi:https://doi.org/10.1016/j.nimb.2005.12.011.
- [42] J. M. D. Coey. *Magnetism and Magnetic Materials*. 2010. doi:10.1017/CB09780511845000.

8 Conclusions

In this thesis several aspects of different transition metal oxides have been studied by a surface science approach. The growth process of ternary oxide films on Ru(0001) and a detailed analysis of electronic, structural and magnetic properties of these films was motivated by their potential applications in a diverse areas such as ceramics, catalysis or magnetic devices. In the following we will present the most important conclusions of this thesis.

1. Nickel ferrite NiFe_3O_4

High-quality single crystal of nickel ferrite were synthesized by high-temperature oxygen-assisted molecular beam epitaxy on Ru(0001) by following the growth in real time and real space by low energy electron microscope (LEEM). The growth process takes place in two stages. At first a continuous layer (called wetting layer) covers the substrate. Next, large micron-wide, 3-dimensional islands grow on top of the wetting layer. The islands were atomically flat. As each one usually arises from a single nucleus they should lack antiphase boundaries. The thickness of the islands estimated from the shadow at XPEEM images was found to be up to 70 nm.

The composition and magnetic properties of the islands were studied by means of XAS and XMCD. The wetting layer was composed of Ni-Fe monoxide. The islands presented the spinel structure with Ni^{2+} cations located in octahedral site and Fe^{3+} cations distributed between octahedral and tetrahedral positions. However there was some Fe^{2+} at the octahedral positions. The XAS measurements revealed that the spinel islands are non-stoichiometric with a composition $\text{Ni}_{0.5}\text{Fe}_{2.5}\text{O}_4$.

The spin and orbital magnetic moment were calculated by applying the sum rules in XMCD. The values obtained for each cation are $m_{spin} = 0.94 \mu_B$ and $m_{orb} = 0.18 \mu_B$ for Fe and $m_{spin} = 1.13 \mu_B$ and $m_{orb} = 0.13 \mu_B$ for Ni, giving a total moment $3.43 \mu_B$. The estimated magnetic moment per formula unit was found to be larger than for stoichiometric NiFe_3O_4 and was likely affected by the surface reconstruction.

The surface magnetization maps have been obtained from XMCD-PEEM images. The high crystalline quality of the islands resulted in large magnetic

domains up to few μm^2 . The magnetic domain structure imaged for both Ni and Fe matched perfectly and presented an out-of-plane component suggested to arise from the bulk magnetocrystalline anisotropy on an iron-rich nickel ferrite.

A sizeable dichroic contrast were also found at the O K edge due to hybridization of neighbouring cations (Ni and Fe). The magnetic moment of oxygen aligned parallel with Ni and Fe resulted in the same magnetic domain configuration observed at XMCD-PEEM images of each element (Ni, Fe and O).

2. Mixed nickel-cobalt oxide $\text{Ni}_x\text{Co}_{1-x}\text{O}$

Mixed Ni-Co oxides were grown on Ru(0001) by HOMBE. The growth in comparison to nickel ferrite proceeded in a one step, starting from single nuclei, 3-dimensional, tens of nm high islands were covering the substrate. The growth at 1150 K gave rise to islands with a triangular shape with two opposite orientations. The triangular islands coexisted with with a few rectangular ones. The selected area LEED of the triangular islands presented an hexagonal pattern indicating a (111) orientation, while the one of rectangular islands had a square diffraction pattern suggesting a (001) orientation.

The chemical state of the surface cation identified by XAS revealed that both Ni and Co are in the 2+ state and thus confirming that the high-temperature growth led to the formation of a mixed nickel-cobalt monoxide phase ($\text{Ni}_x\text{Co}_{1-x}\text{O}$). The element-specific x-ray magnetic linear dichroic images revealed antiferromagnetic domains at room temperature. The magnetic domain structure imaged via XMLD-PEEM for Ni and Co matched perfectly, while the one observed for O is completely different. This indicated that the contrast observed at cobalt and nickel were of the magnetic origin and the one at the anion edge revealed the ordering direction (structural domains).

The Néel temperature of the $\text{Ni}_x\text{Co}_{1-x}\text{O}$ antiferromagnetic nanostructures was studied by polarization dependent x-ray absorption spectroscopy at the Co L_3 edge. The studies confirmed that the Néel temperature of a mixed nickel-cobalt monoxides was well above the room-temperature. Additionally, the temperature could be tuned by adjusting the composition. Within the thickness range of 20 to 80 nm no changes of T_N were found.

3. Fe-doped nickel oxide Fe-NiO

Nickel oxide films were grown on Ru(0001) by oxygen-assisted MBE varying the substrate temperature from 950 K to RT. In all cases, the growth resulted in the formation of small islands, randomly distributed on the sample. This kind of structures could not be observed in LEEM due to limited lateral resolution of the microscope. Thus the surface morphology was confirmed by *ex-situ* AFM measurements. It revealed that NiO grown forming grainy islands along

the Ru atomic steps. It was discovered that a small content of Fe influenced drastically the growth mode.

By adding a small amount of iron, large micron-wide triangular islands could be grown. Two families of islands rotated by 30° between them were found with hexagonal LEED pattern rotated by the same amount.

The chemical state of surface cations have been identified by XAS measurements. This confirmed that the growth of nickel oxide with small amount of Fe led to the formation of Fe^{2+} doped NiO phase, in agreement with the phase diagram. The composition of the islands was extracted from the edge-jump at the XAS spectra and was suggested to be $\text{Fe}_{0.05}\text{Ni}_{0.95}\text{O}$.

The islands studied by XMLD-PEEM presented large antiferromagnetic domains at room temperature. The AFM domain structures were interpreted taking into account an "anisotropic" XMLD, allowing for vectorial magnetometry. It was found that the spin-axis orientation in the islands align with the Ru axes, lie along $\{\bar{1}\bar{1}2\}$ directions, which are the expected directions of a spin-axis in bulk NiO. For comparison, the rotated islands presented an additional out-of-plane component pointing along $[\bar{1}11]$ direction. Its origin could be attributed to strain, although more experiments have to be performed to rule out other effects.

4. Magnetite Fe_3O_4 - Manipulation of magnetic domains in thin magnetite films

The Fe_3O_4 films grown on Ru(0001) were studied by means of new custom-made exchangeable sample holder system comprising two parts: one for high-temperature measurements and another one for the *in-situ* application of small magnetic field. High-quality single crystals of magnetite were synthesized and further characterized *in-situ* by LEEM. The growth proceeded in a similar way to nickel ferrite with wetting layer and large triangular islands on top of it. The composition and magnetic properties of the Fe_3O_4 islands were studied by XAS and XMCD. The islands were confirmed to present a spinel structure with Fe^{2+} and Fe^{3+} cations located in octahedral and Fe^{3+} in tetrahedral sites.

The magnetic state of particular islands was changed by applying an external magnetic field by means of the second part of the sample holder and subsequently imaged via XMCD-PEEM. The switching of individual microstructures could be observed, although in thin islands (up to few nm) the domains did not have a one to one correspondence when the magnetic field was applied in an opposite direction with the same absolute value. This is suggested to be caused by domain wall pinning.

Apart from thin islands, MBE growth led also to formation of thick ones (up to tens of nm thick). Those islands studied by PEEM presented a (Landau) flux

closure domain configuration in which the magnetostatic energy is minimized. The observed magnetic domain structure was compared with the micromagnetic simulations of objects with the same shape and size as the experimental one. Thus, the magnetic configuration can be understood by taking into account the known magnetic properties of bulk defect-free magnetite.

The field excitation of the Landau state were studied by applying a small in-plane magnetic field. It has been observed that even with a small magnetic field (few mT) it is possible to move vortex at the meeting point of three domain walls: the movement of the domain wall implied also a vortex displacement which was perpendicular to the exciting field. The vortex displacement extracted from experimental data has been compared with micromagnetic simulations. The data obtained both experimentally and theoretically are in a good agreement what confirmed that the islands behaved as expected from the known properties of bulk Fe_3O_4 .

A Appendix A

A.1 A custom-made sample holder for high temperature in-situ growth and magnetic field

The exchangeable sample holder system is designed to be compatible with the Elmitec microscopes widely used at synchrotrons. Drawings and pictures of the different parts are shown in Figure A.1. There are two different sample holder bodies: for high temperature (Figure A.1a-b) and for magnetic field application (Figure A.1c-d). The former includes an electrically insulated thoriated tungsten filament for electron bombardment heating up to more than 1500 K and 2 further electric contacts for a W/Re thermocouple. On the top there is an adapter for flag-type sample holder platelets (Figure A.1e), which are inserted in UHV by means of a wobble stick. The sample itself is pressed between the platelet and a top plate with a central hole of variable diameter. The platelet is held in place by W springs which ensure stability for any holder orientation and also after strong temperature variations.

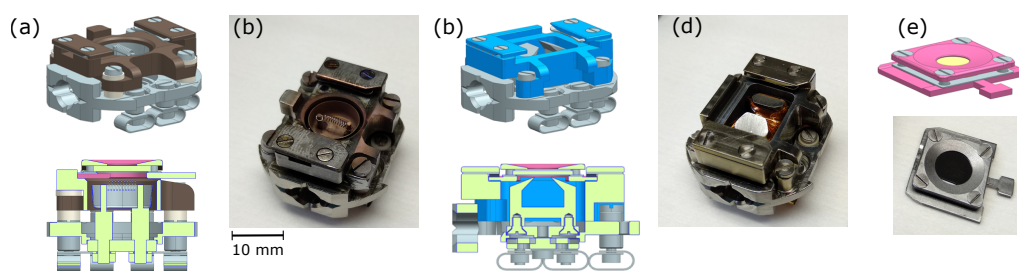


Figure A.1: 3D drawings (a) and picture (b) of the high temperature sample holder base with the electrically insulated filament in the center. 3D drawings (c) and picture (d) of the electromagnet sample holder base with an uniaxial in-plane electromagnet. (e) Platelet transferred between both holder types.

The second sample holder, shown in Figure A.1c-d, features an integrated electromagnet for uniaxial, in-plane magnetic field. It comprises a monolithic Permendur yoke and a coil wound from Kapton-insulated 0.14 mm diameter copper wire. With 2×350 windings and 3 mm gap it is possible to reach 50 mT/A. Although the available power supply provides ± 1 A, the maximum field which can be applied during an experiment is limited by different factors such as the pressure increase due to

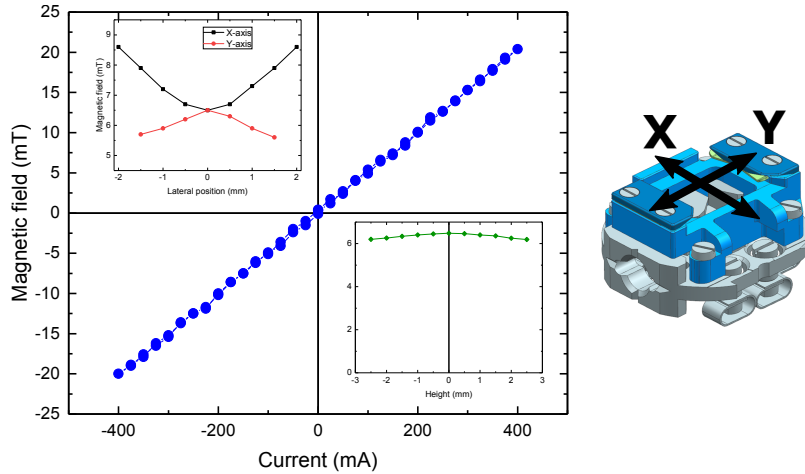


Figure A.2: Measured magnetic field produced by the in-plane sample holder in the sample surface position (0.5 mm above the yoke plane) as a function of current. Left upper inset: field measured for 0.1 A when displacing the Hall probe along different in-plane directions (as indicated in the right panel). Right lower inset: measured field as a function of Hall probe position (for 0.1 A) as a function of height.

wire heating and image distortion due to the electron deflection. In practice we typically apply a maximum of 0.3 A for extended periods (i.e., imaging) and higher currents (up to 1 A) in the form of short pulses for switching or setting a certain magnetic state. The magnetic field produced in this assembly was measured with a Hall probe (Projekt Elektronik) with an active area $2\text{mm} \times 1\text{mm} \times 1\text{mm}$ as is shown in Figure A.2. In the main panel the measured magnetic field at the sample surface position is plotted (0.5 mm above the yoke plane). The field direction can be switched by 180 degrees changing the current sense. In the upper left inset in Figure A.2 the measured field B as a function of the in-plane position along the two principal axes is shown. Along the gap (X direction), the center represents the minimum of the field, while for the lateral (Y direction) maximum field is in the center. In the vertical direction - lower right inset (Z axis) the maximum of the field is at the yoke gap tips (0 mm), while at the sample position it is slightly reduced (typically 0.5 mm above the yoke). We note that this sample holder system has been designed to be highly customizable, e.g., for other electromagnet geometries.

The whole assembly was tested in the ALBA XPEEM, operating at the most demanding conditions in terms of vacuum (sample at - 20 kV). Both sample holder bodies were outgassed in UHV (10^{-9} mbar) prior to the experiments and the XMCD images with applied magnetic field were acquired with up to 0.25 A applied current.

B List of acronyms and abbreviations

MBE	Molecular Beam Epitaxy
PLD	Pulse Laser Deposition
UHV	Ultra High Vacuum
IMFP	Inelastic Mean Free Path
eV	Electronvolt
MEM	Mirror Electron Mikroskopy
DF LEEM	Dark Field Low Energy Electron Microcopy
RHEED	Reflection of High Energy Electron Diffraction
LEED	Low Energy Electron Diffraction
LEEM	Low Energy Electron Microcope
TEM	Transmission Electron Microscope
PEEM	Photoemission Electron Microcope
XPEEM	X-ray Photoemission Electron Microcope
SPELEEM	Spectroscopic Photoemission and Low Energy Electron Microscope
QSE	Quantum Size Effect
QW	Quantum Well
ML	Monolayer
FOV	Field Of View
HV	High Voltage
RT	Room Temperature
ARPES	Angle Resolved Photoemission Spectroscopy
MCH	Main Chamber
XPS	X-ray Photoemission Spectroscopy
XAS	X-ray Absorption Spectroscopy
XNCD	X-ray Natural Circular Dichroism
XMCD	X-ray Magnetic Circular Dichroism
XNLD	X-ray Natural Linear Dichroism
XMLD	X-ray Magnetic Linear Dichroism
CF	Crystal Field
NFO	Nickel ferrite
NCO	Mixed nickel-cobalt oxide
P	Polarization
M	Magnetization
A	Asymmetry
m_{spin}	Spin magnetic moment
m_{orbit}	Orbital magnetic moment

B List of acronyms and abbreviations

μ_B	Bhor magneton
N_h	Number of $3d$ holes per formula unit
n_d	Number of $3d$ electrons per cation
T_z	Dipole operator
ϵ	Conductivity tensor
μ_{abs}	Absorption intensity
Oh	Octahedral
Td	Tetrahedral
γ	Tension
APB	Antiphase Boundary
k_b	Boltzman constant
λ	Saturation magnetostriction
K	Shape anisotropy
H_d	Demagnetizing field
M_S	Saturation magnetization
A_{ex}	Exchange stiffness
AFM	Atomic Force Microscopy
AF	Antiferromagnetic
FM	Ferromagnetic
RS	Rocksalt
a	Lattice parameter
T_C	Curie temperature
T_N	Néel temperature
Å	Angstrom

C

CV

Personal data

- ↳ Name: Anna Mandziak
- ↳ Date of birth: 20.07.1992,
- ↳ Address: Pokrzywnica 9, 27-225 Pawłów,
- ↳ Email: ania_mandziak@o2.pl

Education

- ↳ 2015-2017: MSc in Technical Physics, Thesis: “Ultrathin antimony films on W(110)”, (Advisor: dr hab. R. Zdyb); Maria Curie-Skłodowska University, Lublin, Poland,
- ↳ 2011-2015: ENg in Technical Physics, Thesis: “The project of the system for surface structure investigation by low-energy electron diffraction (LEED)”, (Advisor: dr hab. Z. Korczak); Maria Curie-Skłodowska University, Lublin, Poland

List of publications

1. G.D. Soria, C. Granados-Mirallas, [A. Mandziak](#), M. Saura-Múzquiz, P. Jenus, J. E. Prieto, M. Christensen, M. Foerster, L. Aballe, J. Fernandez, J. de la Figuera and A. Quesada, *Uncorrelated magnetic domains in decoupled SrFe₁₂O₁₉ -Co hard/soft bilayers*, J. Mater. Chem., submitted (2020).
2. G.D. Soria, J. F. Marco, [A. Mandziak](#), S. Sánchez-Cortés, M. Sánchez-Arenillas, J. E. Prieto, J. Dávalos, M. Foerster, L. Aballe, J. López-Sánchez, J. C. Guzmán-Mínguez, C. Granados-Mirallas, J. de la Figuera and A. Quesada, *Influence of the growth conditions on the magnetism of SrFe₁₂O₁₉ thin films and the behavior of Co/SrFe₁₂O₁₉ bilayers*, J. Phys. D, **53**, 344002 (2020).
3. [A. Mandziak](#), J. Prat, J. de la Figuera, J. E. Prieto, M. Foerster, L. Aballe, *Combining high temperature sample preparation and in-situ magnetic fields in XPEEM*, Ultramicroscopy, **214**, 113010 (2020).
4. B. Casals, N. Statuto, M. Foerster, A. Hernandez-Mínguez, R. Cichelero, P. Manshausen, [A. Mandziak](#), L. Aballe, J. Manel Hernandez, F. Macia, *Generation and imaging of magnetoacoustic waves over millimeter distances*, Phys. Rev. Lett., **13**, 124 (2020).
5. S. Ruiz-Gómez, [A. Mandziak](#), J. Prieto, M. Aristu, E. Trapero-Díaz, G. Soria, A. Quesada, M. Foerster, L. Aballe, and J. de la Figuera, *A Real Time XAS PEEM Study of the Growth of Cobalt Iron Oxide on Ru(0001)*, J. Chem. Phys., **7**, 152 (2020).
6. G. Delgado Soria, P. Janus, M. Sanchez Arenillas, J. F. Marco Sanz, J. E. Prieto, P. Prieto, [A. Mandziak](#), M. Foerster, L. Aballe, M. Valvidares, H. Babu Vasili, E. Pereiro, A. Quesada, J. de la Figuera, *Strontium ferrite platelets: from the atomic scale to magnetic domains through x-ray circular dichroism*, Sci. Rep., **1**, 9 (2019).
7. [A. Mandziak](#), G. D. Soria, J. E. Prieto, P. Prieto, C. Granados-Mirallas A. Quesada, M. Foerster, L. Aballe, J. de la Figuera, *Tuning the Néel temperature in an antiferromagnet: the case of Ni_xCo_{1-x}O microstructures*, Sci. Rep., **9**, 13584 (2019).
8. M. Foerster, N. Statuto, B. Casals, A. Hernandez, S. Finizio, [A. Mandziak](#), L. Aballe, J. Manel Hernandez and F. Macia, *Quantification of propagating and standing surface acoustic waves by stroboscopic X-ray Photoemission Electron Microscopy*, J. Synch. Rad., **1**, 26 (2019).

-
9. A. Mandziak, J. de la Figuera, S. Ruiz-Gómez G. D. Soria, L. Pérez, P. Prieto, A. Quesada, M. Foerster, L. Aballe, *Structure and magnetism of ultrathin nickel-iron oxides grown on Ru(0001) by high-temperature oxygen-assisted molecular beam epitaxy*, *Sci. Rep.*, **8**, 17980 (2018).
 10. M. Foerster, I. Fina, B. Casals, S. Finizio, A. Mandziak, F. Fauth, L. Aballe, *Disclosing odd symmetry, strain driven magnetic response of Co on Pt/PMN-PT (011)*, *J. Phys.: Condens. Matter.*, **8**, 31 (2018).
 11. M. Kopciuszynski, A. Mandziak, M. Dachniewicz, R. Zdyb, *Regular distribution of $(\sqrt{3} \times \sqrt{3})$ Bi-reconstructed stripes on Si(553) surface*, *Thin Solid Films*, **631**, 80-84 (2017).